The Rhine River plume

Unravelling its dynamics and sea-level contributions

Keyzer, L.M.

DOI
10.4233/uuid:a27be347-b9e4-45f7-885f-31b8ec466f78

Publication date
2025

Document Version
Final published version

Citation (APA)
Keyzer, L. M. (2025). *The Rhine River plume: Unravelling its dynamics and sea-level contributions*. [Dissertation (TU Delft), Delft University of Technology]. https://doi.org/10.4233/uuid:a27be347-b9e4-45f7-885f-31b8ec466f78

Important note
To cite this publication, please use the final published version (if applicable).
Please check the document version above.

The Rhine River Plume

Unravelling its dynamics and sea-level contributions

L.M.Keyzer

The Rhine River plume

Unravelling its dynamics and sea-level contributions

The Rhine River plume

Unravelling its dynamics and sea-level contributions

DISSERTATION

for the purpose of obtaining the degree of doctor
at Delft University of Technology,
by the authority of Rector Magnificus prof. dr. ir. T.H.J.J. van der Hagen
chair of the Board for Doctorates,
to be defended publicly on 05 June 2025 at 12.30

by

Lennart Martijn KEYZER

Master of Science in Civil Engineering
Delft University of Technology, The Netherlands
born in Woerden, The Netherlands.

This dissertation has been approved by the promotors.

Composition of the doctoral committee:

Rector Magnificus	chairperson
Prof.dr. J.D. Pietrzak	Delft University of Technology, promotor
Prof.dr.ir. M. Snellen	Delft University of Technology, promotor
Prof.dr. C.A. Katsman	Delft University of Technology, promotor

Independent members:

Prof.dr.ir. D.G. Simons	Delft University of Technology
Prof.dr. H. Burchard	Leibniz Institute for Baltic Sea Research
Prof.dr. C.W. Hughes	University of Liverpool
Dr. M. Duran Matute	Eindhoven University of Technology
Prof.dr.ir. A.J.H.M. Reniers	Delft University of Technology, reserve member

This work is part of the research project 'Versatile Hydrodynamics', which is funded by the Netherlands Organization for Scientific Research (NWO).

Keywords: river plume, Rhine ROFI, wind-driven response, sea-level variability, multibeam echosounder, sound speed inversion

Cover by: Shannon Loos

An electronic version of this dissertation is available at http://repository.tudelft.nl.

Contents

PREFACE

When I was young, I could spend hours trying to divert mountain streams or protect my sandcastles at the beach against the sea. Working with water fascinated me long before I realized it could become a career. Yet when the time came to choose a study, my choice for Civil Engineering at Delft University of Technology wasn't part of a grand plan. But looking back, it now seems almost inevitable that I ended up pursuing a BSc in Civil Engineering and an MSc in Hydraulic Engineering. Step by step, the fascination I had as a child found its way into academic and professional life.

Starting a PhD was another step I hadn't foreseen. But when the opportunity arose to study the Rhine River plume, it felt like a natural next step to further dive into the fields of hydraulic engineering, numerical modelling and coastal oceanography.

And now here I am, writing the preface as the final part of my thesis. I am grateful for the opportunities I've had throughout this journey, and I am proud of the dissertation you are reading. However, I could not have done it alone. This thesis wouldn't have been possible without the help of many people who supported me. I would like to sincerely thank all of you.

First, I would like to thank my promotors. Julie, thank you for your enthusiasm and support throughout this project. After supervising my MSc thesis, you planted the idea of pursuing a PhD by asking if I'd consider applying for this position. Your knowledge on river plumes and your endless ideas really inspired me grow as a researcher. During more difficult times, you also cared about my well-being, which I deeply appreciate. Mirjam, thank you for sharing your expertise in underwater acoustics and multibeam echosounders. Your guidance, and the way you were able to clearly explain complex concepts to me, were crucial for this part of the research. Caroline, thank you for your pragmatism and your constructive feedback throughout the project. Your clear advice helped us keep an eye on the bigger picture and ensured the project kept moving forward. I really enjoyed working together with all three of you — thank you!

I would also like to thank Chris Hughes, Hans Burchard, Matias Duran Matute, and Dick Simons. I appreciate that you are willing to take the time to serve as independent committee members for my PhD defense and review my work.

I had the opportunity to carry out this research within the project Versatile Hydrodynamics, and I would like to thank the entire project team and my co-authors — Roland, Cornelis, Martin, Firmijn, Yosra, Henrique, and Frithjof — for the pleasant collaboration. Yosra and Henrique, it was great to share this journey with you as fellow PhD candidates. Cornelis, thank you for your guidance and support as the project leader. Firmijn and Martin, thank you for sharing your expertise in numerical modelling and for your valuable input throughout the project. Frithjof, I appreciated working together on connecting hydrodynamic modelling with satellite remote sensing, your enthusiasm and insights were inspiring. Tannaz, thank you for sharing your knowledge on multibeam echosounders and the processing of its measurements. Without your help I could not have done this, and I really enjoyed working together.

During my time at TU Delft, I had the pleasure of meeting so many amazing col-

leagues, for which I am truly grateful. A special word to my colleagues from the second floor: Floris, Carine, Silke, Sotiria, Marlein, Tess, Gal, Said, Juanma, Jessamy, Dennis, Paul, Lucas, Anne, Steffie and Sabine — thank you for the good company, the (digital) coffee breaks, the walks, the after-work drinks, the discussions, and most importantly the laughs and jokes. I am also grateful to all the other PhD candidates, postdocs and staff members I crossed paths with during these years. Learning about your research and sharing ideas made it an inspiring environment to work in. And Otti and Sandra, thank you for taking care of all the practical and HR matters during my PhD.

While water and oceans are among the most fascinating things there is, my research is not the most important thing in life. I would like to thank all my friends and family, allowing me to escape from my research. Special thanks to Daan and Daniël for being my paranymphs, I am sure you will help making my defense an extra special day. Mom, Dad, Elise, I cannot thank you enough for everything, from my childhood to my student years, and still today. Your belief in me — even without knowing exactly what I was working on — and your unconditional support has been invaluable, during the good times and even more so during the more challenging moments. And finally, Shan, merci dat jij er ben. I'm so grateful for your patience, trust, help, and everything else and I'm also very proud of you.

Thanks to all of you. Enjoy reading this thesis and I hope we will see each other soon!

Lennart Keyzer
Rotterdam, May 2025

SUMMARY

River plumes are formed when freshwater from rivers enters the salty ocean, creating buoyant water masses that strongly influence coastal circulation. Worldwide, hundreds to thousands of river plumes are found with varying geometry and properties. By transporting freshwater, heat, nutrients, sediments and pollutants, they impact the ocean circulation, coastal zones and ecosystems on local (10–100 km) and even (beyond) regional scales (> 1000 km), depending on the size and dynamics of the plume.

The goal of this thesis is to improve our understanding of the Rhine River plume and the subsequent interactions with sea-level variations (Chapter 1). The Rhine River plume is located along the Dutch coast in the Southern North Sea, formed by the outflow of the Rhine River which is deflected towards the right due to Earth's rotation. Influenced by tides, bottom friction and atmospheric forcing, the plume forms a highly dynamic system.

In Chapter 2, the variability of the wind-driven response of the Rhine River plume is examined using a high-resolution, 3D model. Simulations forced by idealized wind conditions show the wind-driven response significantly varies during a spring-neap cycle. During neap tide, when tidal mixing is weaker, the Rhine River plume is stratified, and the wind-driven response is in accordance with Ekman dynamics. Under downwelling winds, the plume thickens and moves onshore, whereas upwelling winds cause the plume to thin and spread offshore. However, during spring tide, the stratification is reduced due to increased tidal mixing, changing the wind-driven response. Under downwelling winds, the plume does not narrow and, instead, enhanced mixing occurs. Under upwelling winds, the plume is mixed before freshwater can spread offshore. The spring-neap variability of the plume is in turn modulated by these wind-driven changes. During downwelling winds, the plume is less sensitive to variations in tidal mixing due to the stronger stratification and reduced interfacial area. In contrast, upwelling winds create a thinner, wider plume that is more sensitive to tidal mixing. Expressing the potential energy anomaly in salinity coordinates proved valuable for tracking freshwater transport and understanding connectivity across different plume regions. These results show how the competition between straining and mixing, both induced by tides and winds, determine the structure and evolution of the Rhine River plume.

In Chapter 3, the impact of the Rhine River plume on sea-level variability along the Dutch coast is investigated by comparing baroclinic and barotropic simulations. While sea-level variability is predominantly driven by tidal and atmospheric forces, the river plume induces steric changes, which contribute to sea-level variability. The Rhine River plume induces a positive anomaly in steric height, elevating the annual mean sea level along the Dutch coast. Near the river mouth at Hoek van Holland, the steric signal shows strong tidal modulation and exhibits slower variations correlated with changes in river discharge. These steric changes are coherent with the tidal signal because of the tidally-pulsed river outflow, leading to an elevation of the low water levels

and a decrease in tidal amplitude. Farther downstream, the steric contribution diminishes due to mixing, and no significant effect on tidal sea-level variability is observed. Nevertheless, comparison of sea levels with satellite altimetry reveals improved agreement when the river plume is included, indicating its influence on sea-level variability and highlighting the necessity to properly resolve river plumes in models. This shows that even a river plume formed by a moderate river like the Rhine River can affect sea-level variability, underscoring the importance of taking river plume dynamics into account in coastal sea-level studies.

In addition, this thesis also explores innovative observational techniques to support future research on river plumes. A proof-of-concept is developed for the inversion of sound speed profiles from multibeam echosounder measurements. The theoretical background for this method is introduced in Chapter 4, while the inversion technique itself is presented in Chapter 5. The method is based on minimizing the mismatch between overlapping swaths caused by the use of erroneous sound speed profiles. Using empirical orthogonal functions to describe the sound speed profiles limits the number of unknowns that needs to be found during the inversion. Simulations show that the inverted sound speed profiles deviate by only 1–3 ms^{-1} from the correct profiles in the proof-of-concept. Since sound speed is influenced by depth, temperature, and salinity, the sound speed profiles derived from multibeam echosounder measurements can offer valuable insights into the vertical structure of the water column. This proof-of-concept is a first step towards the collection of temperature and salinity profiles using data that is routinely collected but not exploited.

Overall, this thesis advances our understanding of the Rhine River plume and its contribution to sea-level variability through detailed modelling and novel analysis methods. In addition, the development of a proof-of-concept for retrieving sound speed profiles from multibeam echosounder measurements offers a promising approach to provide valuable information on stratification in river plumes. Together, these contributions support improved modelling and understanding of coastal oceans, particularly river plumes, which will become more and more important, especially in the face of climate change and its impact on coastal regions.

SAMENVATTING

Rivierpluimen ontstaan wanneer zoet rivierwater de zoute oceaan instroomt, waarbij drijvende watermassa's worden gevormd die de stromingen sterk beïnvloeden. Wereldwijd zijn er honderden tot duizenden rivierpluimen met uiteenlopende vormen en eigenschappen. Door het transport van zoet water, warmte, nutriënten, sediment en verontreinigingen beïnvloeden riverpluimen de oceaancirculatie, kustzones en ecosystemen op lokale (10—100 km) en zelfs regionale schaal (meer dan 1000 km), afhankelijk van de omvang en dynamiek van de pluim.

Het doel van dit proefschrift is om ons begrip van de rivierpluim van de Rijn en de interactie met zeespiegelvariaties te verbeteren (Hoofdstuk 1). De Rijnpluim bevindt zich langs de Nederlandse kust in de zuidelijke Noordzee en ontstaat door de uitstroom van de Rijn, welke door de draaiing van de aarde naar rechts wordt afgebogen. Onder invloed van getijden, bodemwrijving en atmosferische krachten vormt zich een zeer dynamisch systeem.

In Hoofdstuk 2 wordt met behulp van een driedimensionaal numeriek model onderzocht hoe de windgedreven respons van de Rijnpluim varieert gedurende een spring-doodtijcyclus. Simulaties onder geïdealiseerde windcondities tonen aan dat de reactie van de pluim sterk verschilt tussen springtij en doodtij. Tijdens doodtij, wanneer de getijdenmenging zwakker is, is de Rijnpluim gestratificeerd en wordt de pluim beïnvloedt door Ekmantransport. Bij een kustparallelle wind uit het zuidwesten, die via het Coriolis-effect water naar de kust transporteert, wordt de pluim dikker en beweegt deze richting de kust. Bij een kustparallelle wind uit het noordoosten, die opwelling veroorzaakt door het water van de kust af te voeren, wordt de pluim dunner en verspreidt deze zich verder zeewaarts. Tijdens springtij daarentegen wordt de stratificatie verminderd door verhoogde menging, wat leidt tot een andere windgedreven respons van de Rijnpluim. Onder zuidwesten wind treedt nu geen versmalling van de pluim op, maar juist extra menging. Bij noordoosten wind wordt de pluim gemengd voordat het zoete water zich verder zeewaarts kan verspreiden. De variabiliteit tussen spring- en doodtij wordt op haar beurt weer beïnvloed door deze windgedreven veranderingen. Bij zuidwesten wind is de pluim minder gevoelig voor variaties in getijdenmenging door de sterkere stratificatie en het kleinere oppervlak. Noordoosten wind zorgt daarentegen voor een dunnere, bredere pluim die gevoeliger is voor menging. Het uitdrukken van de potentiële energie anomalie in coördinaten gebaseerd op de saliniteit bleek waardevol voor het volgen van het transport van zoet water en voor het begrijpen van de connectiviteit tussen verschillende delen van de riverpluim. Deze resultaten laten zien hoe de verhouding tussen menging en rek ("straining"), welke beide worden gedreven door wind en getij, de structuur en evolutie van de Rijnpluim bepaalt.

In Hoofdstuk 3 wordt door middel van barotrope en barocliene modelsimulaties onderzocht hoe de Rijnpluim bijdraagt aan de zeespiegelvariabiliteit langs de Nederlandse kust. Hoewel de waterstand voornamelijk wordt beïnvloed door getijden en atmosferische krachten, veroorzaakt de rivierpluim sterische veranderingen die ook

bijdragen aan zeespiegelvariabiliteit. De Rijnpluim leidt tot een positieve sterische anomalie, wat leidt tot een hogere jaargemiddelde waterstand langs de kust. Nabij de riviermonding bij Hoek van Holland vertoont de sterische hoogte een sterke getijdensignaal en langzamere variaties die samenhangen met veranderingen in rivierafvoer. De getijgedreven sterische veranderingen worden veroorzaakt door de getij-afhankelijke riveruitstroom. Dit resulteert in een verhoging van de laagwaterstanden en een vermindering van de getijdenamplitude. Verder stroomafwaarts neemt de sterische bijdrage af door menging, en is er geen significant effect op het getij meer waarneembaar. Toch toont een vergelijking van waterstanden met satellietmetingen een betere overeenkomst wanneer de rivierpluim is meegenomen in het model, wat het belang aantoont van een correcte representatie van rivierpluimen. Dit bevestigt dat zelfs een pluim van een rivier met een gemiddelde afvoer zoals de Rijn een meetbare invloed kan hebben op zeespiegelvariabiliteit en benadrukt het belang van het meenemen van rivierpluimen in zeespiegelstudies.

Daarnaast onderzoekt dit proefschrift innovatieve observatietechnieken voor toekomstig onderzoek naar rivierpluimen. Er is een proof-of-concept ontwikkeld voor het achterhalen van geluidssnelheidsprofielen op basis van multibeam echoloodmetingen. De theoretische achtergrond van deze methode wordt geïntroduceerd in Hoofdstuk 4, terwijl de inversiemethode zelf wordt uitgewerkt in Hoofdstuk 5. De methode is gebaseerd op het minimaliseren van verschillen in gemeten waterdiepte tussen overlappende banen die ontstaan bij het gebruik van foutieve geluidssnelheidsprofielen tijdens multibeam echoloodmetingen. Door gebruik te maken van empirische orthogonale functies om de profielen te beschrijven, wordt het aantal onbekenden in de inversie beperkt. Simulaties tonen aan dat de geïnverteerde profielen slechts 1—3 ms^{-1} afwijken van de correcte profielen in dit proof-of-concept. Omdat de geluidssnelheid afhankelijk is van diepte, temperatuur en saliniteit, kunnen deze profielen waardevolle informatie bieden over de verticale structuur van de waterkolom. Dit concept vormt een eerste stap richting het afleiden van temperatuur- en zoutgehalteprofielen uit gegevens die routinematig worden verzameld, maar doorgaans niet worden benut in oceanografisch onderzoek.

Deze studie draagt bij aan een beter begrip van de Rijnpluim en haar invloed op zeespiegelvariabiliteit, door middel van gedetailleerde modellering en nieuwe analysetechnieken. Daarnaast biedt het proof-of-concept voor het afleiden van geluidssnelheidsprofielen uit multibeam echoloodmetingen een veelbelovende methode om informatie te verkrijgen over stratificatie in rivierpluimen. Samen ondersteunen deze bijdragen een verbeterde modellering en kennis van kustzeeën, in het bijzonder van rivierpluimen, wat in de toekomst steeds belangrijker zal worden, zeker met het oog op klimaatverandering en de gevolgen daarvan voor kustgebieden.

CHAPTER 1
Introduction

1.1 Motivation

1.1.1 What is a river plume?

Rivers discharge yearly 40.0×10^3 km^3 ($= 7500\times$ volume of IJsselmeer) freshwater into the ocean (Trenberth et al., 2007). When river runoff enters the ocean, a river plume is formed: a buoyant body of brackish water. The input of freshwater by rivers results in density gradients in the coastal ocean, since freshwater is lighter than salty seawater. These density differences drive currents and damp turbulence in the ocean, thereby strongly influencing the coastal circulation. Worldwide, hundreds to thousands of river plumes are found with varying geometry and properties. Depending on the size of the plume, they impact oceans on local (10–100 km) and even (beyond) regional scales (> 1000 km).

1.1.2 Why are river plumes important?

The coastal zone (elevation < 100 m and distance < 100 km of the coast) is home to 27% of the world's population and 42% of the world's GDP is generated here, while it only covers 9% of the Earth's surface (Kummu et al., 2016). Due to the accumulation of human activity in this area, large quantities of wastewater, fertilizer, plastics and other pollutants are produced. Rivers transport this matter to the sea, where it ends up in river plumes.

By transporting heat, nutrients, sediments and pollutants, river plumes strongly influence coastal (eco)systems. For example, the Mississippi River plume influenced the transport of oil in the Gulf of Mexico during the Deepwater Horizon oil spill in 2010 (Kourafalou and Androulidakis, 2013). Furthermore, strong stratification induced by river plumes can result in the formation and destruction of hypoxic areas — dead zones where life dies due to the lack of oxygen — in, for example, the Gulf of Mexico (Wiseman et al., 1997; Hetland and DiMarco, 2008) and the Baltic Sea (Carstensen et al., 2014). Another example is the sargassum strandings in the Caribbean, which are associated with flooding of the Amazon River (Oviatt et al., 2019). Via the river plume, excessive amounts of nutrients are transported to the ocean, where sargassum growth is enhanced. Along the Dutch coast, the Rhine River plume affects sediment transport, resulting in the formation of turbidity maximum zones (Flores et al., 2020).

In polar regions, ocean properties are strongly influenced by plumes formed by meltwater, affecting the melting rates of glaciers that protrude into the sea (Straneo and Cenedese, 2015).

Socioeconomic trends such as demographic growth, migration and economic developments will further increase the anthropogenic pressure on the coastal zone (McGranahan et al., 2007). Meanwhile, the coastal zone is increasingly prone to flooding due to the impact of sea-level rise (Nicholls and Cazenave, 2010; Vousdoukas et al., 2018), which affects the height and frequency of extreme water levels (Woodworth et al., 2011). Understanding the coastal ocean circulation and the role of river plumes is therefore critical for coastal zone management.

1.2 River plume dynamics

There is a strong interaction between the river plume and the ocean, creating a highly dynamic environment. The dominant physical processes that control the spreading and mixing of the plume vary throughout the river plume. In this thesis, we therefore adopt the description of river plumes formulated by Horner-Devine et al. (2015) in terms of a near-, mid- and far-field region, each representing a dynamically distinct region (Figure 1.1). We refer to the direction moving away from the river mouth as the downstream direction. This section presents an overview of the current understanding of river plume dynamics in each of these three regions.

1.2.1 The near-field plume

First, the near-field region starts at the river mouth, where river runoff already interacts with the ocean (Figure 1.1). The structure of the near-field plume is determined by the properties of the outflow at the river mouth (Nash et al., 2009). The buoyancy and momentum of the outflow are determined by estuarine processes. The estuarine Richardson number Ri_E describes the non-dimensional ratio between stratifying and mixing processes in the estuary (Eq. 1.1):

$$Ri_E = g' \frac{Q_f}{W_E u_{tidal}^3} \,. \tag{1.1}$$

Here, g' represent the reduced gravity and is defined as $g' = g(\Delta\rho/\rho_0)$, where g is the gravitational acceleration (ms^{-2}) and $\Delta\rho$ the density difference of the plume relative to the ocean's density ρ_0. Q_f is the freshwater discharge (m^{3}s^{-1}), W_E the width of the river mouth (m) and u_{tidal} the tidal velocity (ms^{-1}).

The resulting vertical structure of the near-field plume depends on the river discharge, thereby affecting the downstream evolution of the river plume. Higher river discharge results in a thicker, more stratified near-field plume.

Typically, momentum dominates over buoyancy in the near-field plume, resulting in a jet-like outflow. Consequently, shear mixing (also called interfacial mixing) is maximum in the near-field plume.

In tidally-dominated areas, the near-field dynamics vary strongly in time. Due to the tidal modulation of the river outflow, a pulse of freshwater enters the ocean on every ebb tide. The edge of the pulse, which is often visible as a line of foam on aerial

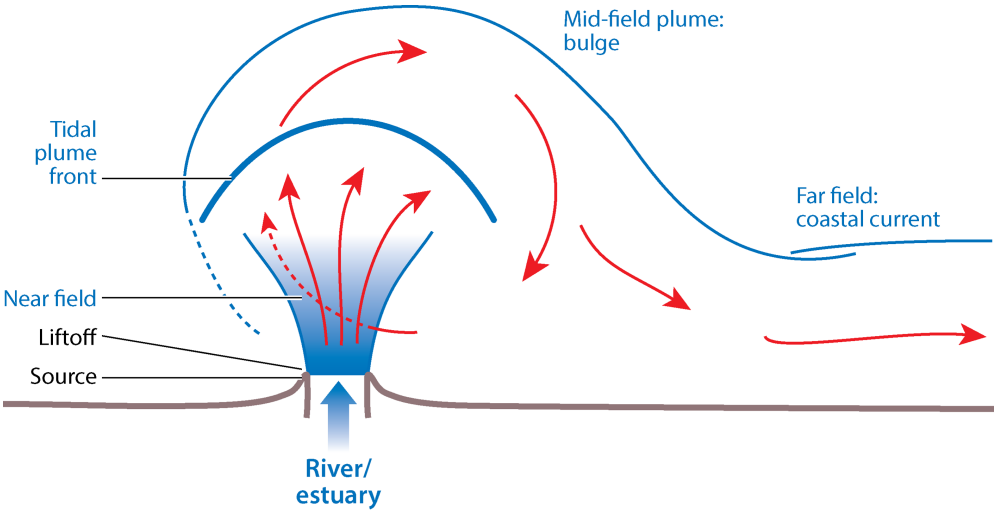

Figure 1.1: Schematic representation of a prototypical river plume (Horner-Devine et al., 2015), where the freshwater outflow is represented by blue and the red arrows indicate the flow direction.

imagery, is called a tidal plume front. These fronts are found, for example, in the plumes of the Columbia River (Orton and Jay, 2005), Rhine River (Rijnsburger et al., 2018, 2021a) and Merrimack River (Spicer et al., 2022). Near the fronts, intense turbulence is observed, being an important source of mixing.

In the case of wide river mouths, Earth's rotation dominates over the initial momentum in the plume near the mouth, similar to the far-field plume (Horner-Devine et al., 2015). This is generally the case when the river mouth is wider than the Rossby radius L_R, which is defined as:

$$L_R = \sqrt{gh}/f\,, \tag{1.2}$$

where g, h and f are the gravitational acceleration (ms^{-2}), the water depth (m) and Coriolis parameter (-), respectively (Horner-Devine et al., 2015).

1.2.2 The mid-field plume

Second, the mid-field region forms the transitional region between the near- and far-field plume (Figure 1.1). Here, the river outflow is arrested and turns into a alongshore coastal current under the influence of Earth's rotation.

Many numerical simulations of river plumes produce an anticyclonic circulation in the mid-field plume, generally known as the bulge (e.g. Oey and Mellor, 1993; Kourafalou et al., 1996; Garvine, 2001; Fong and Geyer, 2002). Actual observations of a bulge have been reported for only a couple of river plumes. Chant et al. (2008) observed the formation of a bulge in the Hudson River plume. Hickey et al. (1998) and Horner-Devine (2009) presented measurements of a bulge circulation in the Columbia River plume. Pichevin and Nof (1997) explained that, in case of a steady inflow, no force exists that can balance the momentum flux away from the mouth in the coastal

currents. As a consequence, the plume expands offshore continuously, forming an anticyclonic bulge circulation (Nof and Pichevin, 2001). The ballooning of the outflow in the offshore direction introduces a Coriolis force, which counteracts the momentum flux of the coastal current.

Fong and Geyer (2002) show that the alongshore transport of freshwater is reduced due to the offshore expansion of the bulge. They relate the alongshore transport and the shape of the bulge to the Rossby number at the river mouth:

$$Ro = \frac{U}{fW}\,, \tag{1.3}$$

where U is the depth-averaged velocity (ms^{-1}), f the Coriolis parameter (s^{-1}) and W the width of the river mouth (m). In their idealized simulations, the alongshore transport is smaller for high Rossby numbers. Ambient currents enhance the alongshore transport of freshwater and limit the ballooning of the outflow in the offshore direction, stabilizing the bulge (Fong and Geyer, 2002; Isobe, 2005).

In the mid-field plume, shear mixing can still be substantial, but is smaller than in the near-field region since the outflow momentum is lost and flow velocities are smaller. Wind-, wave- and bottom-generated (tidal) mixing become more significant, which all act over the entire plume. Winds and waves induce mixing from the surface. Winds induce a vertically sheared current, the so-called Ekman spiral, which results in vertical mixing. Previously, it was assumed that wind mixing was neglible in the near- and mid-field plume. However, Kakoulaki et al. (2014) and Spicer et al. (2022) showed that winds also induce mixing and straining in the mid-field plume. Furthermore, waves induce near-surface turbulence due to breaking, being a source of mixing. As the effect depends on the ratio between plume depth and the wave height (Kastner et al., 2018), wave mixing is more important in smaller, thinner plumes (Thomson et al., 2014). In shallow seas, bottom friction can generate shear instabilities from (tidal) currents, inducing bottom-generated mixing (Spicer et al., 2021).

1.2.3 The far-field plume

Last, the mid-field plume transitions into the far-field region, where the plume is no longer influenced by the initial momentum of the outflow (Figure 1.1). Here, the plume forms an alongshore current, which is balanced by wind stress (Fong and Geyer, 2001; Jurisa and Chant, 2013; Lentz, 2004), Earth's rotation (Garvine, 1987) and, depending on the ocean's depth, bottom friction.

Winds can significantly influence the far-field plume by displacing the plume and modifying the alongshore transport. Winds induce a transport directed 90 degrees towards the right (on the Northern Hemisphere, towards the left on the Southern Hemisphere) relative to the wind direction: the so-called Ekman transport. Downwelling-favourable winds, which blow in the direction of the alongshore current, induce an onshore Ekman transport, narrowing and thickening the plume (Figure 1.2a) (Whitney and Garvine, 2005; Moffat and Lentz, 2012). Upwelling-favourable winds, which are in the opposite direction of the coastal current, limit alongshore transport and induce an offshore Ekman transport, forcing the plume offshore while it thins (Figure 1.2b) (Fong and Geyer, 2001; Lentz, 2004), possibly detaching the plume from the coast.

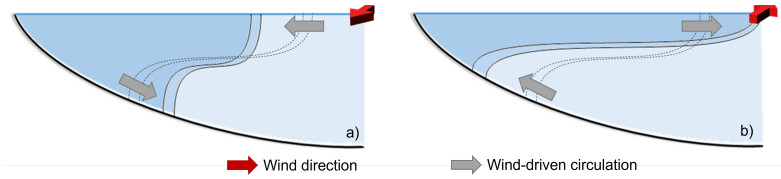

Figure 1.2: Schematic representation of the position and thickness of the river plume under the influence of Ekman transport induced by a) downwelling-favourable and b) upwelling-favourable winds. Darker blue indicates freshwater. The dashed lines indicate the plume's initial position.

In a shallow, frictional river plume, sometimes referred to as a Region Of Freshwater Influence (ROFI) (Horner-Devine et al., 2015), the structure and cross-shore extent of the far-field plume is affected by the interaction between bottom friction, tidal currents and stratification (Simpson, 1997). Examples of such plumes are Liverpool Bay and the Rhine ROFI. Bottom friction alters the vertical structure of tidal currents in shallow waters. Depending on the stratification, the tidal currents follow an elliptical path. By assuming a vertically uniform eddy viscosity, Prandle (1982) could describe the tidal currents using two counter-rotating phasors. Bottom friction has less influence on the cyclonic phasor (i.e., the tidal component rotating in the direction of the Earth's rotation) than on the anticyclonic phasor (i.e., the tidal component rotating against the direction of the Earth's rotation), and the resulting bottom boundary layer is therefore thinner. In this way, the properties of tidal currents in a well-mixed water column could be explained, such as the major axes, ellipticity, inclination and phase, and their vertical variations.

Contrastingly, when the water column is stratified, the strong decrease in eddy viscosity near the pycnocline decouples the bottom and surface layer. Therefore, the assumption of a constant eddy viscosity applied by Prandle (1982) no longer holds (Maas and van Haren, 1987; de Boer et al., 2006). To describe the effect of stratification on the vertical structure of tidal currents, Visser et al. (1994) developed a conceptual model, showing that a cross-shore component develops in the surface layer when the water column is stratified (Figure 1.3). Since the proximity of the coast requires a zero net cross-shore transport, an opposite-directed current near the bottom develops, resulting in counter-rotating tidal ellipses that form a vertically sheared current. These tidal ellipses have been observed in Liverpool Bay (Simpson et al., 1990), the Rhine ROFI (Fisher et al., 2002) and the York estuary (Simpson et al., 2005).

When these vertically sheared currents act on a horizontal density gradient, the stratification changes (Figure 1.4). This is called tidal straining. The water column stratifies when the surface velocities are directed offshore and the bottom velocities onshore, while it destratifies when the surface velocities are directed onshore and the bottom velocities offshore. Consequently, tidal straining can induce a semidiurnal cycle in the stratification, called Strain-Induced Periodic Stratification (SIPS), as has been observed in the Rhine ROFI (Simpson and Souza, 1995; Fisher et al., 2002) and Liverpool Bay (Simpson et al., 1990; Rippeth et al., 2001; Verspecht et al., 2010).

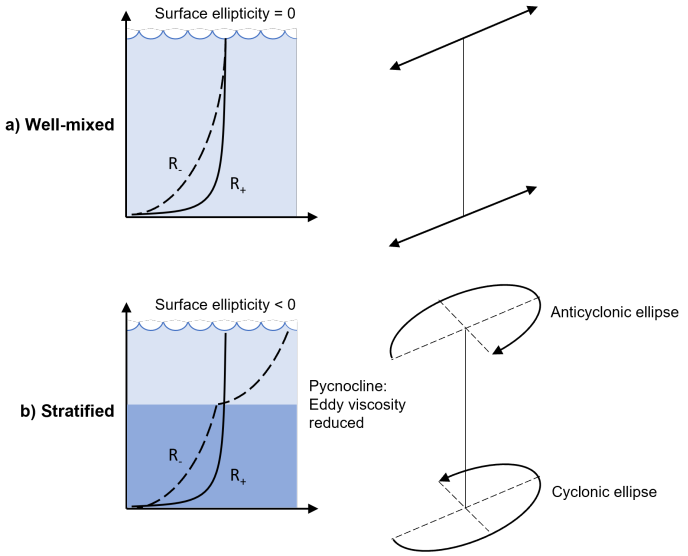

Figure 1.3: Schematic representation of the effect of bottom friction on the cyclonic (R_+) and anticyclonic phasor (R_-) of the tidal currents for a well-mixed (a) and stratified water column (b) (after Visser et al., 1994). Darker blue indicates denser water. At the pycnocline, the eddy viscosity reduces, decoupling both layers and modifying the anticyclonic boundary layer. When the water column is stratified, counter-rotating tidal ellipses are formed.

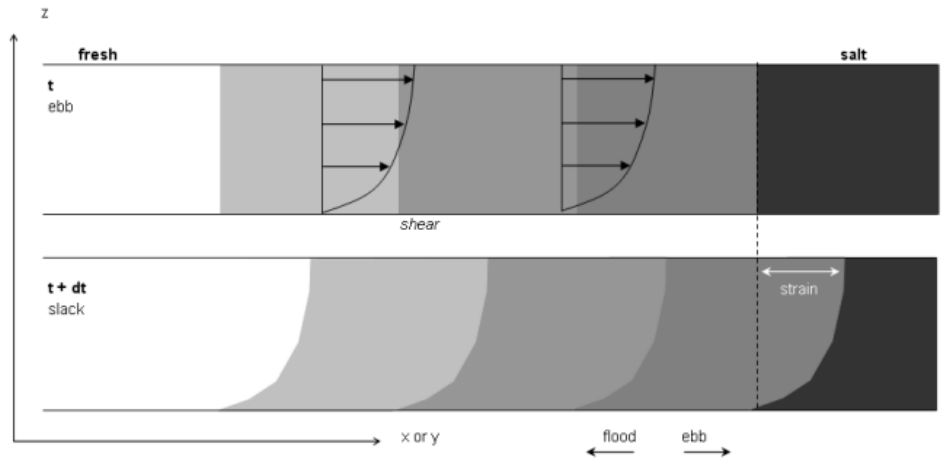

Figure 1.4: Schematic representation of tidal straining (de Boer, 2009). Colors indicate the water density (darker is denser), vectors indicate flow profile over depth.

1.2.4 Quantifying mixing and stratification

Mixing in river plumes generally occurs when the turbulence is strong enough to overcome the buoyancy. This can be presented by the Richardson number Ri: a dimensionless number defined as the ratio between buoyancy and vertical shear.

$$Ri = \frac{N^2}{(\partial u/\partial z)^2}\,, \tag{1.4}$$

where N^2 is the buoyancy frequency and $\frac{\partial u}{\partial z}$ the vertical gradient in horizontal flow velocity. The buoyancy frequency equals

$$N^2 = -\frac{g}{\rho_0}\frac{\partial \rho}{\partial z}\,, \tag{1.5}$$

where g is the gravitational acceleration (ms^{-2}), ρ the density (kgm^{-3}) and ρ_0 the reference density (kgm^{-3}). The denominator in Eq. 1.4 represents the squared vertical shear in horizontal currents, which is associated with the amount of turbulence. Mixing generally occurs when Ri is smaller than 0.25. From a physical point of view, when $Ri < 0.25$, the vertical velocity shear is strong enough to overcome the stratification, inducing mixing. Stratification, in turn, is the result of the competition between buoyancy and mixing. Mixing and stratification are therefore inextricably connected

To investigate the different mixing mechanisms in river plumes and their relative importance, mixing and stratification need to be quantified. Two different approaches are commonly used for the quantification of mixing and stratification: the potential energy anomaly analysis and the salinity variance method. Here, we discuss the definitions and limitations of these different approaches.

Potential energy anomaly

To quantify stratification and analyse mixing, Simpson (1981) introduced the potential energy anomaly ϕ (Jm^{-3}).

$$\phi = \frac{1}{H}\int_{-h}^{\eta} (\bar{\rho} - \rho) g z \, dz\,, \tag{1.6}$$

where H is the water depth (m), η the sea surface height (m), h the bed level (m), ρ the density (kgm^{-3}), $\bar{\rho}$ the depth-averaged density ($\bar{\rho} = \frac{1}{H}\int_{-h}^{\eta} \rho \, dz$), g the gravitational acceleration (ms^{-2}) and z the vertical coordinate (m) (positive upwards). The potential energy anomaly represents the amount of energy needed to vertically mix the water column, being a measure for the strength of the stratification.

By considering the rate of change of the potential energy anomaly, Simpson and Bowers (1981) derived empirical parametrizations for tidal (Eq. 1.7) and wind mixing (Eq. 1.8), providing a simple way to evaluate the relative importance of different drivers of mixing.

$$P_b = \frac{4\epsilon k_b \bar{\rho} u^3}{3\pi H} \tag{1.7}$$

$$P_w = \delta C_d \gamma \rho_a \frac{W^3}{H} \tag{1.8}$$

In Eq. 1.7, $\epsilon = 0.0037$ is the mixing efficiency, $k_b = 2.5 \times 10^{-3}$ the seabed drag coefficient, $\bar{\rho}$ the depth-averaged density (kgm^{-3}), u the depth-averaged velocity (ms^{-1}) and H the water depth (m). In Eq. 1.8, $\delta = 0.023$ represents the wind mixing efficiency, $C_d = 2.3 \times 10^{-3}$ the surface drag coefficient, $\gamma = 0.03$ the ratio of surface current speed to wind speed, ρ_a the air density (kgm^{-3}) and W the wind speed (ms^{-1}).

Using the parametrizations for wind and tidal mixing of Simpson and Bowers (1981), Pritchard and Huntley (2006) calculated a simple energy budget to evaluate the relative magnitudes of mixing processes, including frontal, wind and tidal mixing. These empirical parameterizations for wind and tidal mixing require assumptions on the stirring efficiency and drag coefficients, introducing substantial uncertainty. Furthermore, shear mixing (also known as interfacial mixing) is not accounted for. Consequently, the energy budget is hard to close. However, the use of the potential energy anomaly, including these simplified parametrizations, has still proven to be useful in many studies by quantifying the stratification and mixing: for example, for the analysis of the position of fronts in shelf seas (Simpson and Hunter, 1974; van Aken, 1986), stratification in fjords (Wiles et al., 2006) and tidal mixing and straining in river plumes and estuaries (de Boer et al., 2008; Pein et al., 2018; Spicer et al., 2021; Zhang et al., 2023).

Both de Boer et al. (2008) and Burchard and Hofmeister (2008) derived a time-dependent equation for the potential energy anomaly ϕ, closing the energy budget. Below, we follow the notation of Burchard and Hofmeister (2008).

$$
\begin{aligned}
\underbrace{\frac{\partial \phi}{\partial t}}_{\text{Rate of change}} = &- \underbrace{\nabla_h(\bar{\mathbf{u}}\phi)}_{\text{Advection}} + \underbrace{\frac{g}{H}\nabla_h\bar{\rho}\cdot\int z\mathbf{u}'dz}_{\text{Depth-mean straining}} - \underbrace{\frac{g}{H}\int(\eta - \frac{H}{2} - z)\mathbf{u}'\nabla_h\rho' dz}_{\text{Non-mean straining}} \\
&- \underbrace{\frac{g}{H}\int(\eta - \frac{H}{2} - z)w'\frac{\partial\rho'}{\partial z}dz}_{\text{Vertical advection}} + \underbrace{\frac{\rho_0}{H}\int P_b dz}_{\text{Vertical mixing}} - \underbrace{\frac{\rho_0}{2}(P_b^s + P_b^b)}_{\text{Buoyancy fluxes}} \\
&+ \underbrace{\frac{g}{H}\int(\eta - \frac{H}{2} - z)Q dz}_{\text{Density source term}} + \underbrace{\frac{g}{H}\int(\eta - \frac{H}{2} - z)\nabla_h(K_h\nabla_h\rho)dz}_{\text{Divergence of horizontal fluxes}},
\end{aligned}
\tag{1.9}
$$

where ∇_h represents the horizontal gradient operator, $\mathbf{u}$ the horizontal velocity vector, w the vertical velocity, ρ the density, ρ_0 a constant reference density, η the sea surface elevation and H the water depth. The deviation from the depth-mean quantity X is defined as $X' = X - \bar{X}$. $P_b = \frac{g}{\rho_0}K_z\frac{\partial\rho}{\partial z}$ is the vertical buoyancy flux and P_b^s and P_b^b are the surface and bottom buoyancy flux. Q is the density source term (see Burchard and Hofmeister, 2008). K_h and K_z represent the horizontal and vertical eddy diffusivity. Although only applicable to numerical model output, this results in a closed energy budget, allowing for the analysis of stratifying and mixing mechanisms in coastal seas and estuaries.

Salinity variance

To quantify mixing, Burchard and Rennau (2008) introduced the salinity variance method, which is based on the decay of a tracer (salinity). Building upon their work, Li et al. (2018b) linked stratification, straining and mixing by describing the vertical variance $(S'_v)^2 = (S - \bar{S})^2$, the horizontal variance $(S'_h)^2 = (\bar{S} - \langle S \rangle)^2$ and the total variance $(S'_{tot})^2 = (S - \langle S \rangle)^2$ at each location, such that the depth-integrated relationship equals

$$\int (S'_{tot})^2 dz = \int (S'_h)^2 dz + \int (S'_v)^2 dz \,. \tag{1.10}$$

$\langle S \rangle$ is the mean salinity and $\bar{S}$ is the depth-averaged salinity. They also derived an equation for the vertically-integrated salinity variance (neglecting horizontal mixing and divergence of horizontal diffusive fluxes):

$$\underbrace{\frac{\partial}{\partial t} \int (S'_v)^2 dz}_{\text{Rate of change}} + \underbrace{\nabla_h \cdot \int \mathbf{u}_h (S'_v)^2 dz}_{\text{Advection}} = \underbrace{\int -2\mathbf{u}'_v S_v \cdot \nabla \bar{S} dz}_{\text{Straining}} - \underbrace{\int 2K_z \left(\frac{\partial S}{\partial z} \right)^2 dz}_{\text{Mixing}} , \tag{1.11}$$

where ∇_h represents the horizontal gradient operator, $\mathbf{u}_h$ the horizontal velocity vector, K_z the vertical eddy diffusivity. The vertical salinity variance $(S_v)^2$ is a measure for the stratification (Li et al., 2018b). Note that the contribution of temperature (gradients) is not taken into account. Eq. 1.11 forms a closed budget, allowing to determine the bulk mixing in a volume. Any residual is considered numerical mixing (Li et al., 2018b). Although mixing regions can be identified (as in Li et al. (2018b) and Li et al. (2022), for example), mixing cannot be related directly to physical processes such as winds and tides.

Since the stratification is the result of the competition between buoyancy and mixing, mixing and stratification are inextricably connected. The potential energy anomaly and the salinity variance define mixing and stratification from a different perspective. Li et al. (2018b) showed that there is a linear relationship between ϕ/H and $(S'_v)^2$, although temperature is excluded in this case. This suggests that both approaches are similar. What the best approach is, depends on the goal of the analysis and the ambient conditions (e.g., importance of temperature).

1.3 The Rhine River plume

In this thesis, we focus on the Rhine River plume, also known as the Rhine Region Of Freshwater Influence (Rhine ROFI). Since the Netherlands is a low-lying country with 26% of its area below sea level, the coast is frequently nourished for coastal protection. Furthermore, the Port of Rotterdam, the largest port of Europe, is located in the adjacent Rhine-Meuse estuary. With ships becoming bigger and their draught deeper, the margins for error in hydrodynamic forecasts are becoming smaller. Because of its impact on water levels, currents and transport of matter, understanding the dynamics and implications of the Rhine River plume are of vital importance for the Netherlands. This section presents an overview of the study area, including a description of the key characteristics of the North Sea, the Rhine-Meuse estuary and the anatomy of the Rhine River plume.

1

1.3.1 The North Sea

The Rhine River plume is located in the North Sea - one of the largest shelf seas in the world (Huthnance, 1991). The North Sea is connected to the Atlantic Ocean in the north and the south. In the north, the shelf break forms a wide, open connection. The North Sea narrows towards the south between Great Britain and the mainland of Europe. Here, the English channel opens to the Atlantic Ocean. In the east, the North Sea is connected with the Baltic Sea.

The bathymetry of the North Sea is generally shallow with an average depth of 90 m (Figure 1.5). It deepens as it extends towards the Atlantic Ocean, reaching depths of 200 m near the shelf break in the north. Its maximum depth of 700 m is found in the Norwegian Trench. The shallow Dogger Bank (depth <20 m) separates the Southern North Sea from the rest of the sea. The southern basin, stretching from the UK to the coastlines of Belgium, the Netherlands and Germany, has a maximum depth of 50 m.

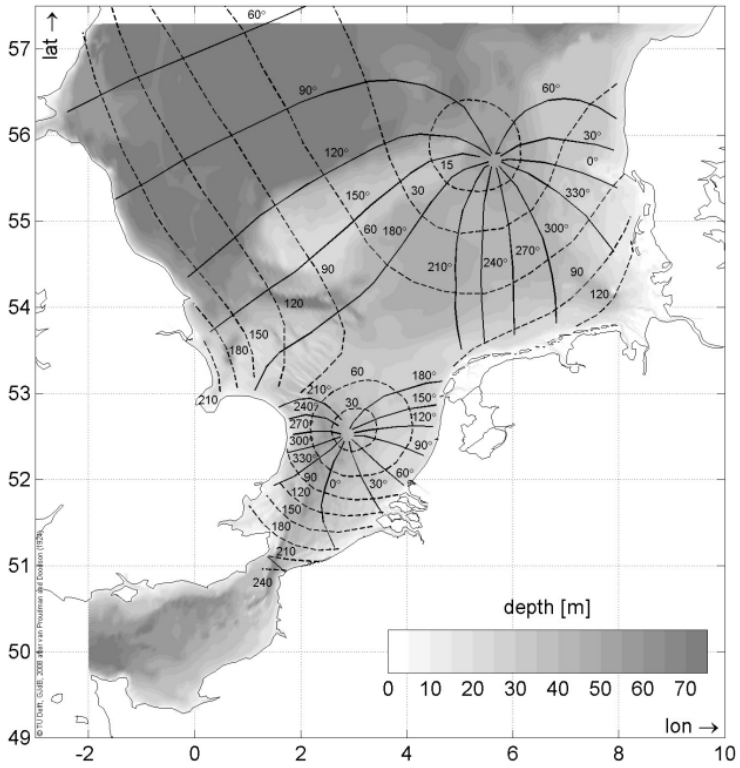

Figure 1.5: Bathymetry and co-tidal lines of the M2-tide in the North Sea (de Boer, 2009)

Sea-level variability in the North Sea is primarily driven by semidiurnal tides (Huthnance, 1991). The superposition of the main lunar and solar constituents (M2 and S2) induce a strong spring-neap cycle. The tidal wave enters from the Atlantic ocean,

primarily between Shetland and Scotland and to a lesser extent through the English Channel, and is amplified on the shelf (Figure 1.5). Three amphidromic points are formed around which the tidal wave propagates (Proudman and Doodson, 1924). The tidal wave propagates counter-clockwise through the basin as a Kelvin wave, meaning that tidal velocities are in phase with the sea surface elevation. At high water (HW) and low water (LW), the alongshore current is maximum and directed northwards and southwards, respectively. Moreover, storm surges induced by winds and/or changes in atmospheric pressure can cause significant currents and extreme sea levels in the Southern North Sea due to its funnel-shaped geometry.

1.3.2 The Rhine-Meuse estuary

The Rhine and Meuse Rivers flow into the Southern North Sea, forming the Rhine River plume. The rivers have a combined mean annual discharge of 2400 m^3s^{-1}. Their discharge varies strongly, with peak discharges in late winter and lowest discharges late summer (Figure 1.6). Nowadays, the Rhine River is fed by both meltwater and rainwater. In the future, however, this might shift towards a rainwater-fed river due to climate change, leading to lower summer discharges and higher winter discharges (Pfister et al., 2004).

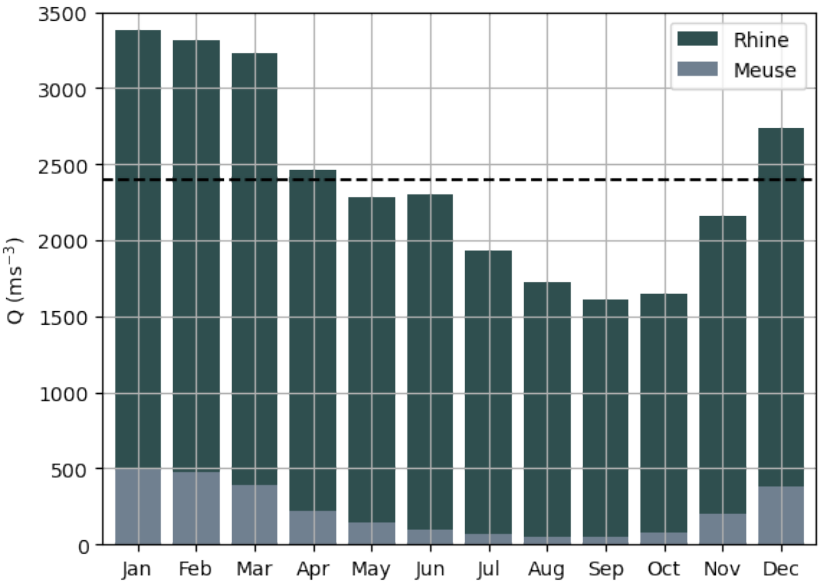

Figure 1.6: Climatological river discharge per month of the rivers Rhine (at Lobith) and Meuse (at Borgharen), based on the period 1995-2020. The dashed line indicates the combined mean river discharge. Data obtained from Global Runoff Data Centre (GRDC) database.

The rivers come together in a heavily engineered network of river branches and channels (Figure 1.7). The discharge of the Rhine River is divided over the Lek and the Boven Merwede. The Meuse River discharges into Hollands Diep. There are two

connections with the sea: the New Waterway and the Haringvliet sluices. The New Waterway is an open connection, and therefore strongly influenced by tides. The Haringvliet sluices are a closed connection, primarily used to discharge excess river runoff. They only open during ebb tide, when the river discharge is larger than 1100 m^3s^{-1}.

Figure 1.7: Distribution of river discharge in the Rhine-Meuse estuary (Rijkswaterstaat, 2019)

1.3.3 Anatomy of the Rhine River plume

The Rhine River plume is formed by the combined discharge of the Rhine and Meuse Rivers. As the discharge of the Rhine River is approximately 10 times larger than the discharge of the Meuse River, the river plume is referred to as the Rhine River plume. The plume extends 20–40 km in the cross-shore direction and over 100 km in the alongshore direction (van der Giessen et al., 1990). Here, we give an overview of our current understanding of the Rhine River plume, following the classification of the near-, mid- and far-field plume.

Near-field plume

In the near-field plume, tidal plume fronts are formed by the tidally-pulsed river outflow. Every ebb tide, a pulse of freshwater is released (de Ruijter et al., 1997). This pulse tends to spread radially. However, it is arrested by the southward directed tidal current, which limits the spreading in the northern direction. As a result, a tidal plume front is formed, which is released around low water slack when the tidal currents turn northwards (Hessner et al., 2001).

Mid-field plume

The tidal plume fronts formed in the near-field plume are advected by the tidal currents and follow an elliptical path while propagating northwards (Rijnsburger et al.,

2018, 2021a). The fronts recirculate for approximately 4 tidal cycles in the mid-field region, creating a multiple front system where they potentially interact and coalesce (Rijnsburger et al., 2021a). Moreover, satellite observations show that the tidal plume fronts are accompanied by internal waves (Rijnsburger et al., 2021b).

In the Rhine River plume, a recirculation has been observed by Rijnsburger et al. (2021a) and Jakšić (2021). Jakšić (2021) investigated the recirculation in the mid-field plume by combining HF radar measurements and model simulations. The diameter of the recirculation varies between approximately 15 km at neap tide and 5 km at spring tide. It only occurs around high water slack (between HW+3 hrs and HW+5 hrs) in the buoyant surface layer. When the tidal currents increase and turn southwards, the recirculation is suppressed. In contrast to high water slack, no recirculation occurs at low water slack. Simulations show that the recirculation is driven by baroclinic processes. This suggests that the interaction between the tides and the river plumes play a crucial role in the formation of the recirculation.

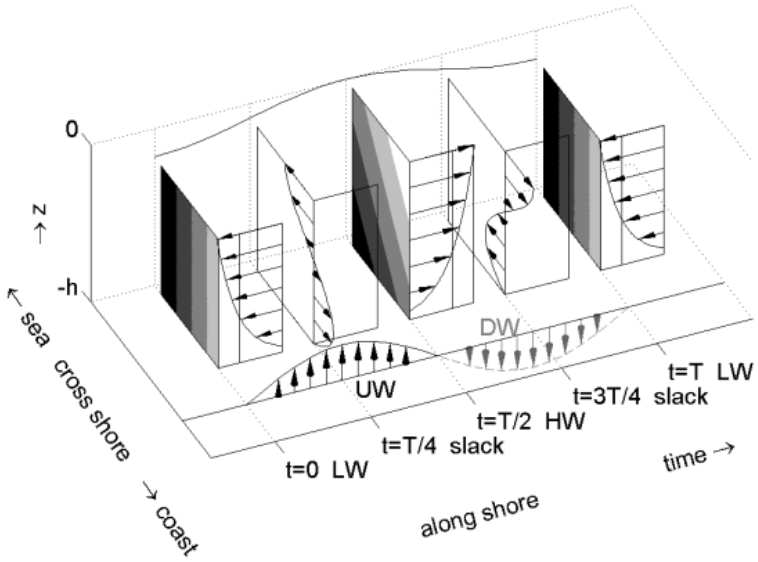

Figure 1.8: Evolution of the stratification in the far-field plume during a tidal cycle (de Boer, 2009)

Far-field plume

The dynamics in the far-field plume are dominated by Advection and Strain-Induced Periodic Stratification (ASIPS) (Rijnsburger et al., 2016; de Boer et al., 2008). As described in Section 1.2.3, bottom friction alters the vertical structure of tidal currents when the water column is stratified, resulting in the formation of counter-rotating tidal ellipses in the bottom and surface layers (Visser et al., 1994; Souza and Simpson, 1996). During ebb tide (from HW to LW), the cross-shore velocities are directed onshore near the surface and offshore near the bottom. During flood tide (from LW

to HW), the cross-shore velocities are directed offshore near the surface and onshore near the bottom. The interaction between the vertical shear in tidal velocity and the horizontal density gradient results in a semidiurnal cycle in stratification (Simpson and Souza, 1995), see Figure 1.8. During ebb tide, the plume stratifies, and during flood tide, the plume destratifies. This is called tidal straining or cross-shore straining. To a lesser extent, depth-mean alongshore advection (i.e., the movement of the water column over a certain horizontal distance without any vertical deformation) contributes to periodic stratification (de Boer et al., 2008).

Furthermore, the far-field plume is subject to a fortnightly cycle in stratification due to variations in tidal mixing (Simpson et al., 1993). Tidal mixing is weaker on neap tide and stronger on spring tide. Hence, the plume is stratified on neap tide and well-mixed on spring tide. During energetic conditions such as storms or spring tide, when the plume is vertically well-mixed, tidal ellipses are more rectilinear (Visser et al., 1994).

1.4 Towards the collection of temperature and salinity data using multibeam echosounders

The collection of field data is crucial for researching river plumes and the calibration and validation of models. However, measuring river plumes is challenging because of their highly dynamic nature combined with their large spatial extent, and the rough conditions on the open ocean.

Nowadays, more and more hydrographic surveys are conducted for, amongst others, nautical safety and marine infrastructure. These are often conducted by multibeam echosounders. A multibeam echosounder is an acoustic instrument, typically attached to the bottom of a boat, that sends out sound waves (pings). These sound waves travel through the water column and are scattered back to the device. The multibeam echosounder measures the two-way travel time and the intensity (the backscatter) of the return signal. Using the two-way travel time and angle of the returned sound waves, combined with a sound speed profile, the water depth can be determined (Lurton, 2002).

The backscatter measured by the multibeam echosounders is already widely used for oceanographic research on gas seeps (Nau et al., 2022), suspended sediment transport (Fromant et al., 2021), and internal waves (Figure 1.9) (Colbo et al., 2014). The biggest limitation, however, is that only qualitative properties of the water column can be derived from the backscatter, rather than the exact water temperature or salinity, for example.

Since the sound speed in the ocean depends on the water temperature, salinity and depth (Medwin, 1975), the sound speed profiles provide insight into the vertical structure of the water column. Therefore, the sound speed could be an important source of information for the research of river plumes. Inferring the sound speed from multibeam echosounder measurements is a first step towards the collection of temperature and salinity profiles using multibeam echosounders.

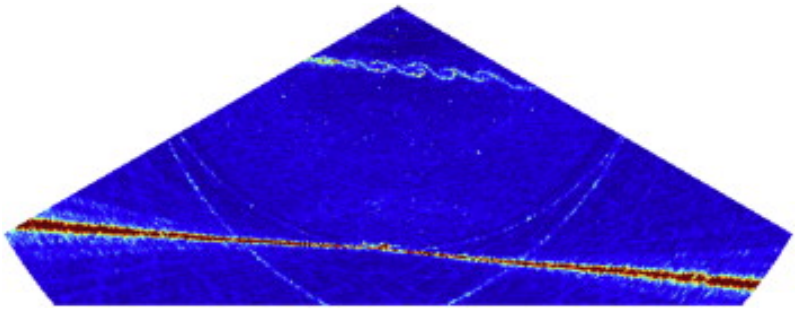

Figure 1.9: Image of water column data, showing internal lee waves, collected using a multibeam echosounder near the sill in Knight Inlet, British Columbia. Red indicates the reflection by the seafloor. [Figure after Trevorrow (2005), as cited in Colbo et al. (2014)]

1.5 Research questions & thesis outline

The goal of this thesis is to improve our understanding of river plumes and the subsequent interactions with sea-level variations by, first, examining the temporal and spatial variability of the Rhine River plume using high-resolution model simulations, and, second, exploring the feasibility of inverting multibeam echosounder measurement to provide high-resolution temperature and salinity data. The following research questions are formulated, each treated in one of the chapters:

1. How is the wind-driven response of the Rhine River plume affected by the fortnightly variability in tidal dynamics? (Chapter 2)

2. What is the impact of the Rhine River plume on sea-level variability along the Dutch coast?(Chapter 3)

3. Can multibeam echosounder measurements be exploited by inverting sound speed profiles to provide high-resolution temperature and salinity data? (Chapter 5)

In Chapter 6, the findings presented in this thesis, including their implications, are discussed and based on these results, ideas for further research are proposed. An outline of this thesis together with a brief motivation and approach to the different questions is provided in the following paragraphs.

Part 1 - River plume dynamics

In the recent decades, our understanding of river plumes in general and the Rhine River plume in particular has improved substantially. However, previous research focused on different processes and regions separately. To date, the temporal variation and the interaction between different processes is often neglected, hindering the comparison and scaling between different plumes. The current knowledge of the Rhine River plume focused on the far-field region, where ASIPS and wind- and tide-induced

mixing control the stratification, and the near- to mid-field region, where the tidal plume fronts are dominant.

In the first part of this thesis, we focus on the connection between those regions in the Rhine River plume, the interaction between the dominant physical processes and the subsequent effects on the sea-level variability. We utilize realistic modelling using the Dutch Continental Shelf Model (DCSM) (Zijl et al., 2018) to further unravel the dynamics of the Rhine River plume and the interaction between different processes and regions.

In Chapter 2, we address the first research question, focusing on the combined effect of winds and tides on the Rhine River plume. First, the model setup is validated against previously collected field data. Subsequently, we investigate the connection between the different regions and interaction between dominant physical processes (winds and tides) by idealizing the forcing conditions (constant alongshore winds and fixed river discharge). Our findings show that changes in plume structure in the near- to mid-field region are critical for the downstream evolution of the plume. This chapter is being prepared for submission:

> Keyzer, L.M., Pietrzak, J.D., Katsman, C.A., Snellen, M., Verlaan, M., Zijl, F., Afrasteh, Y., Guarneri, H., Klees, R., Slobbe, D.C. (in prep.) Spring-neap variability in the wind-driven response of the Rhine River plume.

While the influence of river plumes on the coastal ocean circulation is widely recognized, their impact on sea-level variability has received relatively little attention. However, it is known that changes in density result in changes in sea surface elevation. These are called steric changes. In Chapter 3, we address the second research question, investigating the impact of the Rhine River plume on the sea-level variability along the Dutch coast by combining tide gauge data, satellite altimetry and model hindcasts using DCSM. Our results show that the Rhine River plumes significantly influences tidal and seasonal sea-level variability. This chapter is being prepared for submission:

> Keyzer, L.M., Ehlers, F., Pietrzak, J.D., Katsman, C.A., Snellen, M., Verlaan, M., Zijl, F., Afrasteh, Y., Guarneri, H., Klees, R., Slobbe, D.C. (in prep.), The impact of a river plume on sea-level variability in a shallow shelf sea.

Part 2 - Sound speed inversion

Since models are by definition a simplification of the reality, findings should always be validated using field measurements. But due to spatiotemporal variability of river plumes, obtaining representative data is complex, expensive and time-consuming. The increased availability of multibeam echosounder data provides an opportunity for oceanographic research. As the sound speed, which is required for bathymetric measurements, depends on the temperature and salinity (Medwin, 1975), sound speed profiles provide information on the vertical structure of the water column, which is important for the research of river plumes. In the second part of this thesis, we aim to develop a new method for the inversion of sound speed profiles from multibeam echosounder measurements. This is a first step towards the collection of temperature and salinity profiles using multibeam echosounders.

Chapter 4 provides background information on how multibeam echosounders function and the basic principles of underwater acoustics. In Chapter 5, we present the proof-of-concept of a method to invert sound speed profiles from multibeam echosounder measurements. Theoretically, this method could be applied to invert salinity and temperature profiles from multibeam echosounder measurements, as the sound speed is a function of the salinity and temperature. Given the increased availability of multibeam echosounder data, this could provide the high-resolution (in time and space) temperature and salinity data, needed for the research of river plumes and other oceanic processes. This chapter is published as:

> Keyzer, L.M., Mohammadloo, T.H., Snellen, M., Pietrzak, J.D., Katsman, C.A., Afrasteh, Y., Guarneri, H., Verlaan, M., Klees, R., Slobbe, D.C., (2021). Inversion of sound speed profiles from MBES measurements using Differential Evolution. In *Proceedings of Meetings on Acoustics UACE* (Vol. 44, No. 1, p. 070035). Acoustical Society of America. https://doi.org/10.1121/2.0001508

Part I
River plume dynamics

CHAPTER 2

Spring-neap variability in the wind-driven response of the Rhine River plume

ABSTRACT

The wind-driven response of the Rhine River plume, a tidally-dominated river plume, is studied using a regional, 3D hydrodynamic model. Simulations forced by different wind conditions show how the competition between straining and mixing, both induced by winds and tides, determine the plume structure. On neap tide, when tidal mixing is relatively low and the mid- to far-field plume is strongly stratified, the wind-driven response is in accordance with Ekman dynamics. Under downwelling winds the plume is confined against the coast and thickens, while the plume spreads offshore and thins under upwelling winds. On spring tide, however, tidal mixing is 5 times stronger and the mid- to far-field plume is mainly well-mixed, affecting the wind-driven response of the Rhine River plume. Under downwelling winds, no change in plume width is found; instead, further tilting of the isopycnals induces convective mixing. Under upwelling winds, the offshore spreading of freshwater is limited by the increased tidal mixing, as mixing timescales are significantly reduced. In turn, wind-driven changes in plume structure also affect the spring-neap variability of the plume. The stratification is less sensitive to variations in tidal mixing under downwelling winds. By expressing the potential energy anomaly in terms of salinity coordinates, we show how freshwater is transferred from the near- to the far-field region of the plume via the tidal plume fronts.

2.1 Introduction

River plumes are buoyant water masses, formed by the inflow of freshwater into the ocean. River plumes strongly influence coastal systems around the world by transporting, amongst other, freshwater, sediments, nutrients and pollutants. Where this river-borne matter ends up depends on the dispersion and mixing of these river plumes. To analyse river plumes, they are usually described using three distinct dynamical regions – the near-field region, the mid-field region and the far-field region (Horner-Devine et al., 2015). In the near-field region, the freshwater flows from the estuary into the ocean and the dynamics are dominated by advection and shear mixing (Hetland, 2010). In the mid-field region, the Coriolis force starts to influence the plume dynamics and turns the plume towards the coast. A recirculating bulge can develop in the absence of strong ambient forcing (i.e., winds or tides). Moreover, these regions can be seen as the freshwater source to the far-field region (Hetland, 2010). In the far-field region, the dynamics are primarily governed by the geostrophic balance and mixing is mainly driven by the winds (Fong and Geyer, 2001; Hetland, 2005).

Several studies have shown that winds significantly influence river plumes by inducing vertical mixing and changing their position (e.g. Berdeal et al., 2002; Choi and Wilkin, 2007; Osadchiev et al., 2021). Typically, a river plume is attached to the coast due to Earth's rotation (Yankovsky and Chapman, 1997). Under upwelling winds, however, the alongshore current is arrested and the river plume detaches from the coast due to offshore-directed Ekman transport (Munchow and Garvine, 1993). Fong and Geyer (2001) developed a conceptual model to show how an Ekman-induced straining mechanism forces the plume offshore under upwelling winds, while the plume thins due to shear mixing. After adding entrainment to this theory, Lentz (2004) was able to reproduce observations of the plume's detachment from the coast in Chesapeake Bay. A river plume can also detach from the coast under offshore-directed winds (Jurisa and Chant, 2013). Under downwelling winds, the river plume remains attached to the coast due to the onshore-directed Ekman transport and the alongshore currents are amplified (Simpson, 1997). Similar to Fong and Geyer (2001), Moffat and Lentz (2012) developed a conceptual model for this case of downwelling winds, showing that onshore Ekman transport causes the isopycnals to steepen, leading to narrowing and thickening of the plume. However, in case of strong downwelling winds, when the water column is vertically well-mixed due to wind mixing, the plume width does not change (Lentz and Largier, 2006). These studies often focused on the wind-driven response of the far-field plume.

However, tidal dynamics are often ignored or simplified when studying the wind-driven response, while tides are known to strongly interact with river plumes. Tides can induce a strong time-dependency in the structure of the river plume. Bottom-generated tidal mixing can be an important source of mixing (Spicer et al., 2021), impacting the stratification of river plumes. In the near- to mid-field region, the river outflow can be modulated by the tides, resulting in a pulsed discharge. When the outflow is arrested by tidal currents, tidal plume fronts are formed, as found in, for example, the Columbia River (Kilcher and Nash, 2010), Connecticut River (O'Donnell et al., 1998) and Rhine Region Of Freshwater Influence (ROFI) (Rijnsburger et al., 2021a). In the mid- to far-field region of shallow frictional systems, like Liverpool Bay (Simpson et al., 1990) and the Rhine ROFI (Visser et al., 1994; Simpson and Souza,

1995), tidal currents are vertically sheared due to the influence of bottom friction. When acting on a horizontal density gradient, this leads to the (de-)stratification of the water column; a phenomenon known as tidal straining (Simpson et al., 1990). Although tidal dynamics in river plumes are extensively studied, the combined effect of winds and tides on river plumes remains largely unclear.

Currently, only a few studies investigated the wind-driven dynamics in the near- and mid-field plume under realistic forcing (Kakoulaki et al., 2014; Flores et al., 2017; Rijnsburger et al., 2018; Kastner et al., 2018; Spicer et al., 2022). Kakoulaki et al. (2014) were the first to observe that winds also induce a significant amount of mixing in the near-field region. (Kastner et al., 2018) attributed these wind-induced changes in mixing to the different plume geometry. Using model simulations of the tidally-pulsed Merrimack River plume, Spicer et al. (2022) showed how wind effects influence mixing in the near- and mid-field plume on tidal timescales. However, it is not known what the effect of changes in mixing and plume structure is on the downstream evolution of the plume.

The goal of this study is to investigate how the fortnightly variability in tidal dynamics affects the response to upwelling- and downwelling-favourable winds of the Rhine River plume (in the literature also called the Rhine ROFI), which is known to be strongly influenced by tides and winds (Rijnsburger et al., 2016, 2018, 2021a). In particular, we aim to 1) assess how tide- and wind-induced dynamics affect the near- to mid-field region of the Rhine River plume during a spring-neap cycle and 2) evaluate how mixing and changes in plume structure in the near- to mid-field region affect the wind-driven response of the far-field region of the Rhine River plume.

Analysis of the relative importance of tides and winds and their impact on the different regions is challenging due to the dynamic response of the plume and the interaction between tides, winds and stratification. Simpson (1981) introduced the potential energy anomaly, which has been used to quantify the different processes contributing to stratification and mixing (Burchard and Hofmeister, 2008; de Boer et al., 2008). However, the changing position of the plume hinders a direct comparison under different forcing conditions. To this end, Hetland (2005) introduced the concept of salinity coordinates: a coordinate system that translates with the plume's position as it depends on the local salinity. In this study, we build upon this method and evaluate the potential energy anomaly in terms of salinity coordinates. This allows for the direct comparison of plume structure under different forcing conditions, regardless of the plume's position.

For this study, we use the Dutch Continental Shelf Model (Zijl et al., 2018) – a regional 3D model of the North Sea that is able to accurately model the tides and includes buoyant and meteorological forcing. The model setup is described in Section 2. First, a model hindcast of the summer of 2014 is validated against previously collected field data (Section 3). Subsequently, the combined effect of tides and winds is investigated by analysing the simulations of a spring-neap cycle under varying wind conditions. The methods to assess the wind-driven response are described in more detail in Section 4. The wind-driven response of the Rhine ROFI is examined in a geographic coordinate system (Section 5) and a salinity coordinate system (Section 6). The implications of the results are discussed in Section 7 and the main conclusions can be found in Section 8.

2.2 Study area & numerical model

2.2.1 The Rhine River plume

The Rhine River plume, or also known as the Rhine ROFI, is a shallow, frictional river plume in the southern North Sea, which is strongly influenced by tides. The near- to mid-field region of the plume is dominated by tidal plume fronts, which exists for multiple tidal cycles and interact (Rijnsburger et al., 2021a). These fronts are formed by the pulsed river outflow in a strong tidal cross-flow (Hessner et al., 2001). In the mid- to far-field region, where Coriolis becomes important, the river plume is deflected towards the right against the coast. Here, the spring-neap cycle induces a fortnightly cycle in the stratification (Simpson et al., 1993); the river plume is stratified on neap tide and mainly well-mixed on spring tide. When the plume is stratified, the eddy viscosity decreases at the pycnocline, decoupling the surface and bottom layers (Visser et al., 1994). Consequently, the frictional anticyclonic boundary layer reaches the surface, and counter-rotating tidal ellipses are formed in the surface and bottom layer (Visser et al., 1994; Souza and James, 1996; de Boer et al., 2006). A 180 degrees phase difference between the bottom and surface ellipses causes that the surface currents are directed offshore while the bottom currents are directed onshore during the flood phase of the tidal cycle, and vice versa during the ebb phase. As a result, tidal straining induces a semidiurnal cycle in the stratification, stratifying the far-field region of the river plume during flood and destratifying this region during ebb (Simpson and Souza, 1995; Fisher et al., 2002; de Boer et al., 2008). Moreover, winds modify the stratification; wind stirring can dominate over tidal mixing and is able to vertically mix the water column (Souza and Simpson, 1996; Souza and James, 1996).

2.2.2 Dutch Continental Shelf Model

To study the wind-driven response of the Rhine River plume, we use the Dutch Continental Shelf Model (DCSM) (Zijl et al., 2018). DCSM uses an unstructured grid that covers the northwest European continental shelf. The use of an unstructured grid allows for covering a large domain to obtain an accurate representation of the tides and increasing the grid resolution required to capture the dominant physical processes in the Rhine River plume. Here, we provide a brief overview of the most important model settings (see Zijl et al. (2018) for more details) and describe the different model simulations used in this study.

DCSM is a model configuration in D-Flow Flexible Mesh (D-Flow FM), a hydrodynamic model developed by Deltares that solves the shallow water equations on an unstructured grid. More details and the governing equations can be found in Kernkamp et al. (2011). The domain of DCSM ranges between 15°W–13°E and 43–64°N (Figure 2.1a). The horizontal cell size varies with the depth, from 1/10° in east-west direction by 1/15° in north-south direction in the deep Atlantic Ocean decreasing to approximately 220 m along the Dutch coast in 5 steps of a factor 2. The first three refinements follow the 800 m, 200 m and 50 m isobaths. Compared to the original model schematization of Zijl et al. (2018), the grid is further refined in two steps for this study, resulting in a resolution of approximately 220 m in the Rhine River plume

(Figure 2.1b). Moreover, the Rhine-Meuse estuary is included until approximately 30 km inland (Figure 2.1c). Vertically, 20 sigma layers of uniform thickness are used. A spatially varying bottom roughness coefficient is used to calibrate the water levels (see Zijl et al., 2018).

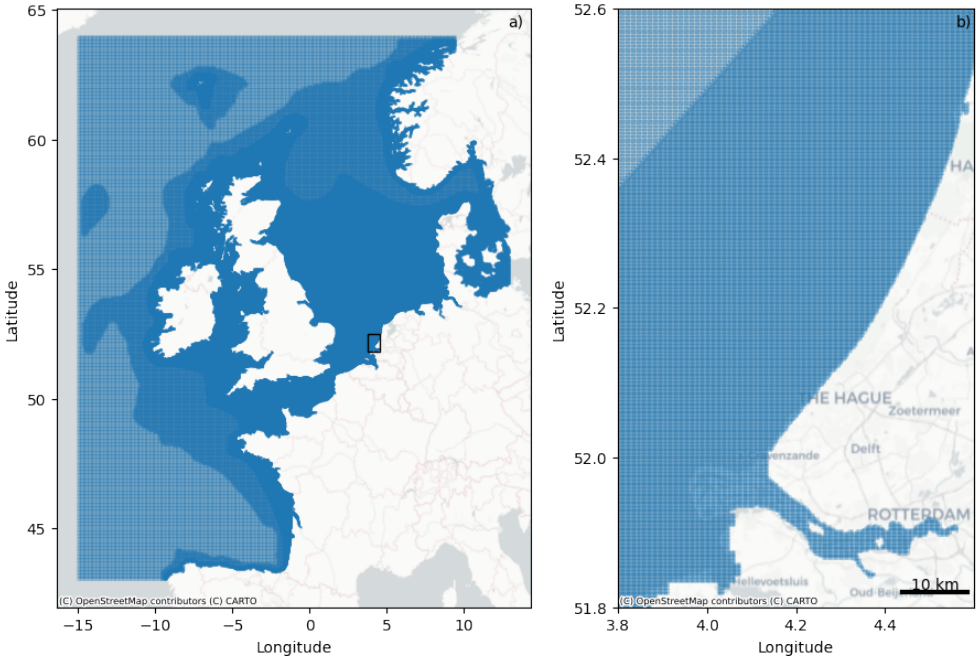

Figure 2.1: a) Computational grid of DCSM, the different colours of blue indicate the first three grid refinements. b) Grid extension including part of the Rhine-Meuse estuary until approximately 30 km inland.

In the north, west and south, the model has (partially) open boundaries. There, the water level is defined using 33 harmonic constituents, taken from the global tide model FES2012. Furthermore, inverse barometer corrections and steric corrections are applied to account for variations in air pressure and density. Temperature and salinity are prescribed based on climatological monthly mean fields, which are taken from the World Ocean Atlas 2018 (Levitus et al., 2014). Furthermore, meteorological surface forcing is applied. Time- and space-varying wind speed and air pressure are taken from the ERA5 reanalysis (Hersbach et al., 2018). To account for the heat exchange with the atmosphere, a surface heat-flux model is used, which requires the input of wind speed, air temperature, cloud cover, dew point temperature and incoming solar radiation. These are also taken from the ERA5 dataset, except for the incoming solar radiation, which is a function of latitude and is corrected for the cloud cover. The discharges of 895 rivers throughout the domain are included using climatological monthly means based on E-HYPE data (Donnelly et al., 2016). Because of our focus on the Dutch coastal zone, the more accurate, actual daily discharge is used for the 6 largest river discharges in the Netherlands (available at https://waterinfo.rws.nl/),

including the Haringvliet, Nieuwe Waterweg and IJmuiden. Since associated water temperatures and salinity are not available, these are set to a constant of 11 °C and 0.001 PSU, respectively. Waves, and thus wave-induced mixing, are not included.

In D-Flow FM, transport of conservative matter is integrated explicitly in time using a higher order scheme based upon the monotonized central limiter. Local time stepping is applied to satisfy the 3D Courant criterion in each cell. For momentum transport, the same higher order scheme is applied in the horizontal and upwind in the vertical. Because local time stepping is computationally expensive for the momentum transport, the global timestep is limited by a maximum 2D Courant number (0.7). For turbulent closure, the $k-\epsilon$ model is combined with a background vertical eddy viscosity and diffusivity, set to 5×10^{-5} and 5×10^{-6} m^2s^{-1} respectively. To compute the horizontal viscosity, the Smagorinsky sub-grid model is used; the empirical coefficient is set to 0.2.

2.2.3 Model validation

In previous work, DCSM has already been successfully validated for water levels, sea surface temperature, mean cross-shore surface salinity gradients, residual transport through the English channel and flow velocities (Zijl et al., 2018). In addition, we validate the model against tide gauge data at the river mouth (Hoek van Holland) and ADCP and CTD measurements 10 km north of the river mouth collected during the STRAINS campaign in September 2014 (Pietrzak et al., 2018; Rijnsburger et al., 2018; Flores et al., 2018). This validation is presented in detail in the appendix. In summary, an accurate representation of the water level is obtained (RMSE $= 9.2$ cm) and the modelled vertical structure of the water column is in good agreement with the observations. As expected, the cross-shore velocities in the surface and bottom layers are directed opposite and change direction twice a day, inducing the typical semidiurnal cycle in the stratification. Moreover, the agreement in vertical structure of the cross-shore velocities indicates that the depth of the pycnocline is resolved correctly. Regarding the salinity, we find a RMSE of 2.77 PSU in the surface layer and 0.36 PSU in the bottom layer. The higher RMSE in the surface layer is a consequence of the passage of tidal plume fronts, which are highly non-hydrostatic and dynamic. However, the bulk properties of the fronts are adequately captured, which is the focus of this study.

2.2.4 Model simulations

For this study, we performed four different simulations with varying wind conditions (Table 2.1). Since we focus on the variability during a spring-neap cycle, we do not only need an accurate representation of the tidal signal, but also allow the density fields to develop and adjust to the tidal forcing. Therefore, the simulations start with a spin-up period of one year. During this period, realistic forcing is included as described in Section 2.2.2. After the spin-up phase, the first simulation spans the period 01 July 2014 - 06 October 2014 and uses realistic forcing to validate the model against field observations. Next, we set up new simulations to explore the wind-driven response to upwelling- and downwelling favourable winds during the same spring-neap cycle as we considered for validation (September 2014). For these simulations, the discharge

of the Rhine River was kept at 1000 m^3/s, corresponding to summer conditions. The first 10 days of the month were used as relaxation time to eliminate the effect of the varying river discharge present during the spin-up phase. Hereafter, the wind fields were modified. For the first simulation, no wind forcing was included to assess the spring-neap variability. This run also acts as our reference case, when assessing the influence of the wind. To investigate the wind-driven response, two additional simulations were done with a constant wind of 5 m/s during the spring-neap cycle. For the first case, a downwelling-favourable southwesterly wind was applied, hereafter referred to as downwelling wind. For the second case, a upwelling-favourable northeasterly wind was imposed, hereafter referred to as upwelling wind.

Table 2.1: Forcing conditions per simulation.

Run	River discharge (m^3s^{-1})	Wind speed (ms^{-1})	Wind direction (°)
Validation	Daily varying	Hourly varying	Hourly varying
No wind	1000	0	-
Downwelling wind	1000	5	225
Upwelling wind	1000	5	45

2.3 Methods

To assess the effect of tides and winds on the Rhine River plume, we focus on the spreading of the freshwater and on the stratification. First, we define the different metrics used to analyse the spreading of freshwater and the stratification. Next, we introduce a salinity-based coordinate system, that allows for the analysis of these metrics regardless of the plume's position.

2.3.1 Freshwater thickness

We quantify the spreading of the freshwater using the thickness of the freshwater layer h_f (m), which is obtained by integrating the freshwater content over the plume depth h_p (m):

$$h_f = \int_{-h_p}^{\eta} \frac{s_0 - s}{s_0}\, dz\,. \tag{2.1}$$

η is the sea surface height (m), s the salinity (PSU) and $s_0 = 32.5$ PSU the reference salinity. The 32.5 PSU isohaline is considered as the river plume boundary in this study.

2.3.2 Potential energy anomaly

The stratification is arguably one of the most important properties of river plumes such as the Rhine River plume, since it modifies the vertical structure of the currents and affects vertical mixing (de Boer et al., 2006). To quantify the strength of the

stratification, Simpson (1981) introduced the potential energy anomaly ϕ (Jm^{-3}), which represents the amount of energy needed to vertically mix the water column.

$$\phi(x,y,t) = \frac{1}{H}\int_{-h}^{\eta}(\bar{\rho}-\rho)gz\,dz\,, \tag{2.2}$$

where H is the water depth (m), η the sea surface height (m), h the bed level (m), ρ the density (kgm^{-3}), $\bar{\rho}$ the depth-averaged density ($\bar{\rho} = \frac{1}{H}\int_{-h}^{\eta}\rho\,dz$), g the gravitational acceleration (ms^{-2}) and z the vertical coordinate (m) (positive upwards).

By integrating ϕ over the plume area A, we obtain the total potential energy anomaly E_ϕ (J) - a time series of the total amount of energy needed to vertically mix the entire river plume (G.J. de Boer, personal communication, 2022), regardless of its position.

$$E_\phi(t) = H\int_A \phi\,dx\,dy\,, \tag{2.3}$$

Stratification is the result of the competition between buoyancy and mixing. To interpret variations in stratification, it is important to understand the strength of the mixing processes. To this end, we can estimate a mixing scale T:

$$T = \frac{\phi}{P}\,, \tag{2.4}$$

where P is the total mixing power. We assume that the total mixing power is the sum of tidal mixing and wind mixing. Simpson and Bowers (1981) derived expressions for tidal and wind mixing based on observational data. Tidal mixing P_b (Wm^{-2}) represents the rate of turbulent mixing near the seabed.

$$P_b = \frac{4\epsilon k_b \bar{\rho} u^3}{3\pi H}\,, \tag{2.5}$$

where $\epsilon = 0.0037$ is the mixing efficiency, $k_b = 2.5\times10^{-3}$ the seabed drag coefficient, $\bar{\rho}$ the depth-averaged density (kgm^{-3}), u the depth-averaged velocity (ms^{-1}) and H the water depth (m). Wind mixing P_b (Wm^{-2}) represents the rate of energy input at the surface due to wind stress.

$$P_w = \delta C_d \gamma \rho_a \frac{W^3}{H}\,, \tag{2.6}$$

where $\delta = 0.023$ is the wind mixing efficiency, $C_d = 2.3\times10^{-3}$ the surface drag coefficient, $\gamma = 0.03$ the ratio of surface current speed to wind speed, ρ_a the air density (kgm^{-3}) and W the wind speed (ms^{-1}).

2.3.3 Salinity coordinates

Comparing the results of the different simulations is complicated by the changing position of the river plume due to the different tidal and wind conditions. The plume is not permanently present at certain locations, while at other locations the governing regime (i.e. near-, mid- and far-field region of the plume) varies. To investigate the plume properties regardless of its location, Hetland (2005) introduced the concept

of salinity coordinates: a coordinate system based on the salinity instead of the geographic position. A view of the river plume in salinity space is obtained by binning the data according to the local salinity into salinity classes (bin width $= 0.1$ PSU). By taking the volume integral, the freshwater volume per salinity class V_f (m^3) is determined, showing the spreading of freshwater in salinity space.

$$V_f(s_A, t) = \iiint_{s<s_A} \frac{s_0 - s}{s_0}\, dV\,, \tag{2.7}$$

where s_0 is the reference salinity and s the local salinity. The plume is bounded by the isohaline s_A. In this study, s_0 and s_A are taken to be equal (32.5 PSU). Hetland (2005) considered the river plume to be a freshwater balance - the change in freshwater content $\partial V_f/\partial t$ in the river plume depends on the freshwater discharge Q_r ($m^3 s^{-1}$) and the salt flux f (PSU ms^{-1}) along an isohaline area A (m^2):

$$s_A \frac{\partial V_f}{\partial t} = s_A Q_r + \int_A f\, dA\,. \tag{2.8}$$

Since mixing shifts freshwater to higher salinity classes, the spreading of freshwater in salinity space, i.e. the freshwater distribution ($\partial V_f/\partial s$), is an indicator for the amount of mixing in the river plume. To quantify mixing, i.e. the freshwater flux in salinity space, a closed freshwater budget is required. However, other freshwater sources often interfere with the river plume, complicating the closure of the freshwater budget. Instead of fully bounding the volume by a constant isohaline, we consider in this study the area between 51.9 °N and 52.4 °N, bounded by the river mouth and the 32.5 PSU isohaline, to minimize the effect of other freshwater sources such as the Haringvliet sluices 15 km south of the river mouth and the IJmuiden sluices 60 km north. This allows us to evaluate solely the mixing of freshwater that originates from the Rhine River (i.e. New Waterway).

Similarly, we can also analyse the stratification in salinity coordinates by binning ϕ per salinity class:

$$\phi(s_l, t) = \int_{s<s_l} d\phi\,. \tag{2.9}$$

As ϕ is a function of x and y only (not z), the results are binned based on the surface salinity (s_l). This allows us to identify differences in stratification within the plume regardless of its position (e.g., the different dynamical regions and tidal plume fronts).

2.4 Model results

The simulations of a spring-neap cycle are forced by different wind conditions, showing the dynamic response of the Rhine River plume to different tidal and wind conditions. First, we assess the spring-neap variability using a simulation without wind forcing by comparing cross sections and maps of the salinity during a tidal cycle. Thereafter, we analyse the wind-driven response of the Rhine River plume using idealized simulations with constant downwelling and upwelling winds of 5 ms^{-1}.

2.4.1 Spring-neap variability of the Rhine River plume

The near- to mid-field region of the Rhine River plume is a highly dynamic area, which is dominated by tidal plume fronts (Rijnsburger et al., 2021a). These fronts are formed every tidal cycle, and are clearly visible in the salinity maps in Figure 2.2. On high water slack (HWS), a first tidal plume front is formed (Figure 2.2a,i). Due to the southward directed tidal currents on ebb, this front is advected southwards (Figure 2.2b,j). Moreover, northward spreading of freshwater is arrested and a second tidal plume front forms north of the mouth. When the tidal currents turn towards the north after low water slack (LWS), this tidal plume front starts propagating northwards along the coast (Figure 2.2c–d,k–l). On HWS, the tidal currents turn onshore and the fronts propagate shorewards. During the next tidal cycle, a new tidal plume front is formed, while the ones from previous tidal cycles are still present (referred to as relic fronts). Under the influence of tides and Coriolis, the tidal plume fronts propagate northwards while swinging anticyclonically. This anticyclonic pathway is a result of the counter-rotating tidal ellipses, resulting from the decoupling of the surface and bottom layers (de Boer et al., 2006).

On neap tide (Figure 2.2a–d), the tidal plume fronts do not escape the mid-field region. Due to relatively weak tidal mixing, the salinity gradients between the tidal plume front and the background plume are weaker, resulting in a lower intrinsic propagation speed of the fronts. Furthermore, tidal advection is not strong enough to separate the different fronts. Consequently, the newly released tidal plume front coalesces with relic fronts in the mid-field region of the Rhine River plume.

On spring tide (Figure 2.2i–l), stronger tidal currents enhance mixing and advection of the tidal plume fronts. Due to increased tidal mixing, the background plume is saltier and, consequently, the salinity gradients are stronger. In combination with enhanced advection, this results in faster propagating fronts. Consequently, a train of fronts is formed, reaching into the mid- and far-field region of the Rhine River plume.

The background plume varies strongly between neap and spring tide, as seen in the cross sections in Figure 2.2. On neap tide (Figure 2.2e-h), the surface salinity is lower due to weaker tidal mixing. The tidal currents not only advect the tidal plume fronts, but also move the background plume on- and offshore. During flood (from LW to HW), the cross-shore component of the surface currents is directed offshore, moving the plume in the seaward direction. During ebb (from HW to LW), the cross-shore component of the surface currents is directed onshore, advecting the plume onshore. On spring tide (Figure 2.2m-p), when tidal mixing is stronger, the plume is saltier, vertically well-mixed and narrower. Increased tidal mixing hinders the offshore spreading during flood and causes the plume to be more confined against the coast. So, in the absence of winds, a river plume was found that is governed by the tides, with strong variations between neap and spring tide.

2.4.2 The wind-driven response

Figure 2.3 shows that the addition of winds generally causes a response of the river plume analogous to Ekman dynamics – the river plume is moved at an angle of 90 degrees to the right of the wind direction. However, there are some distinct differences between neap and spring tide.

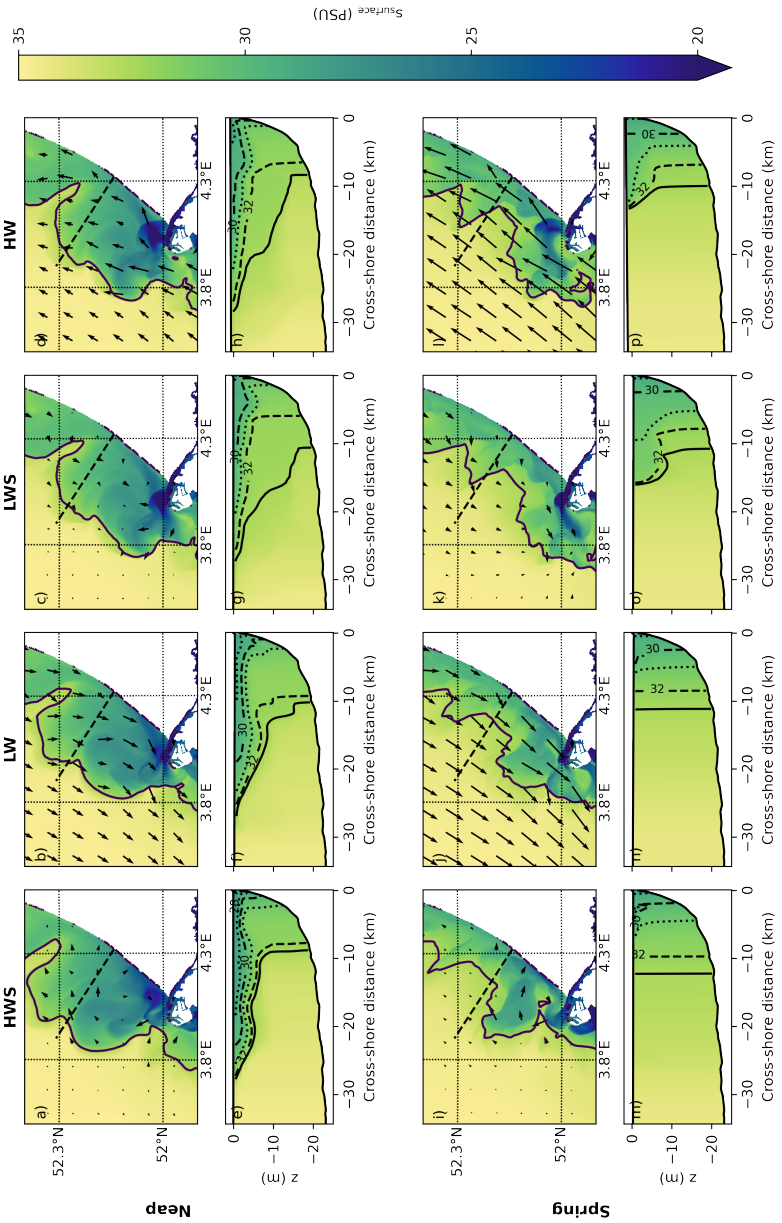

Figure 2.2: The surface salinity during a tidal cycle on neap (a–d) and spring tide (i–l), showing the evolution of the Rhine River plume. Surface current vectors are overlaid. The black line indicates the 32.5 PSU contour. The dashed line denotes the location of the cross sections that are presented in e–h and m–p. Here, the black line indicates the 32.5 PSU contour again, while the dashed and dotted lines represent the odd and even isohalines.

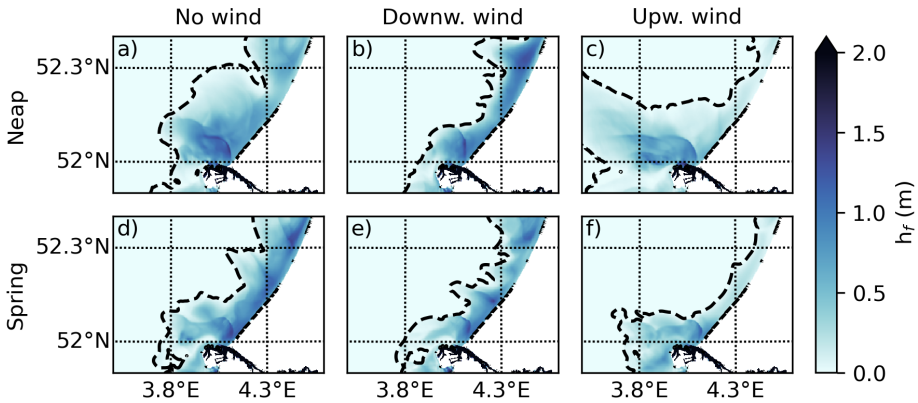

Figure 2.3: Thickness of the freshwater layer h_f at HW during neap (top — a–c) and spring tide (bottom — d-f) under three different wind conditions: no wind (left — a,d), downwelling winds (middle — b,e) and upwelling winds (right — c,f). The dashed black line indicates the 32.5 PSU contour.

Downwelling winds

Under downwelling-favourable winds (SW), there is an onshore-directed Ekman transport (Figure 2.3b,e). Consequently, the freshwater layer narrows and thickens along the coast on neap tide (Figure 2.3b). Since the tidal currents are aligned with the wind during flood, the tidal plume fronts propagate northwards faster. Consequently, a train of fronts is formed in this case, while they coalesce in the absence of wind. On spring tide, tidal plume fronts move even faster. However, no significant changes in plume structure are observed due to the downwelling winds: the freshwater thickness is similar to the situation without wind forcing on spring tide and no narrowing of the plume is found due to onshore-directed Ekman transport (Figure 2.3e).

Upwelling winds

Under upwelling-favourable winds (NE), the Ekman transport is directed towards the northwest (Figure 2.3c,f). The alongshore transport of freshwater is blocked and the northward propagation of the tidal plume fronts is limited. Instead, freshwater is transported in the offshore direction. The remaining band of freshwater along the coast originates from previous tidal cycles during the spin-up period with different wind conditions. On neap tide, when tidal mixing is weaker, the Rhine River plume detaches from the coast (Figure 2.3c). While the tidal currents move the plume back and forth within a tidal cycle (see the case without wind in Figure 2.2a-d), the plume spreads farther offshore every tidal cycle (not shown here). In agreement with the findings of Fong and Geyer (2001), the freshwater layer thins in the offshore direction. On spring tide, however, the offshore spreading is limited (Figure 2.3f). Only the most recently released tidal plume front is visible and freshwater is mixed with ambient seawater within the mid-field region. Consequently, no far-field plume develops in the offshore direction.

2.4.3 Vertical plume structure

Tides and winds both induce vertical mixing, affecting the vertical structure of the plume. We assess the vertical plume structure using the potential energy anomaly. To explain the differences in stratification between the scenarios, we consider mixing timescales and cross sections of the plume.

Figure 2.4 shows ϕ at HW for the different simulations. The stratification varies significantly between neap and spring tide. On neap tide, the Rhine River plume is stratified for all three simulations (Figure 2.4a–c). In the absence of winds, a strongly stratified region (where $\phi > 60\,Jm^{-3}$) is formed due to the coalescence of tidal plume fronts (Figure 2.4a). Due to the addition of winds, mixing increases and ϕ is reduced. Under downwelling winds, the plume narrows due to the onshore Ekman transport and only the coastal waters are stratified (Figure 2.4b). Under upwelling winds, the plume spreads in offshore direction, resulting in stratified offshore waters (Figure 2.4c). The coastal waters towards the north, where some remaining freshwater was found, are vertically well-mixed. ϕ reduces in the offshore direction, which is caused by the thinning of the plume as described by Fong and Geyer (2001).

On spring tide, most of the plume is well-mixed for all three simulations (Figure 2.4d-f). Only the near-field region and the (relic) tidal plume fronts are stratified, albeit weaker than on neap tide due to enhanced mixing in the estuary. The mid- and far-field region are vertically well-mixed due to the stronger tidal mixing in the Rhine River plume in all three simulations, and we find a limited response to Ekman dynamics. Under downwelling winds, we do not find that the plume narrows as it did on neap tide (Figure 2.4e). Under upwelling winds, the offshore spreading of the plume is limited (Figure 2.4f).

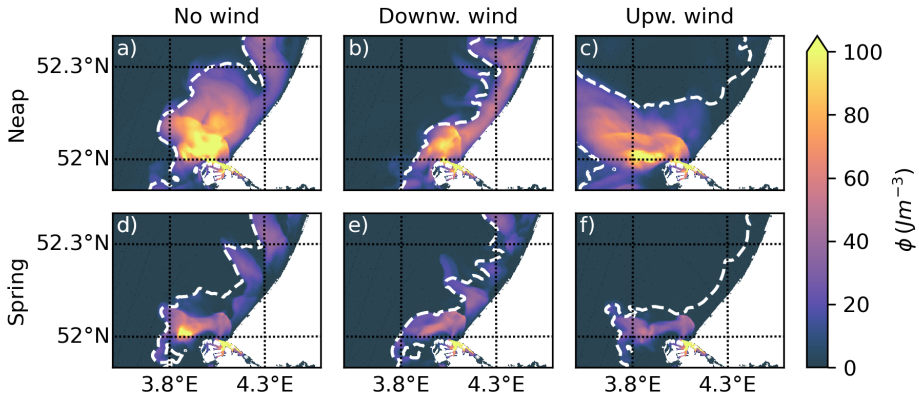

Figure 2.4: Potential energy anomaly (ϕ) at HW during neap (top — a–c) and spring tide (bottom — d–f) under three different wind conditions: no wind (left — a,d), downwelling winds (middle — b,e) and upwelling winds (right — c,f). The dashed white line indicates the 32.5 PSU contour, as also shown in Figure 2.3.

To understand the differences in the wind-driven response of the plume between neap and spring tide, we evaluate the strength of the stratification and mixing processes during a spring-neap cycle in the near-field plume (Figure 2.5). We find no

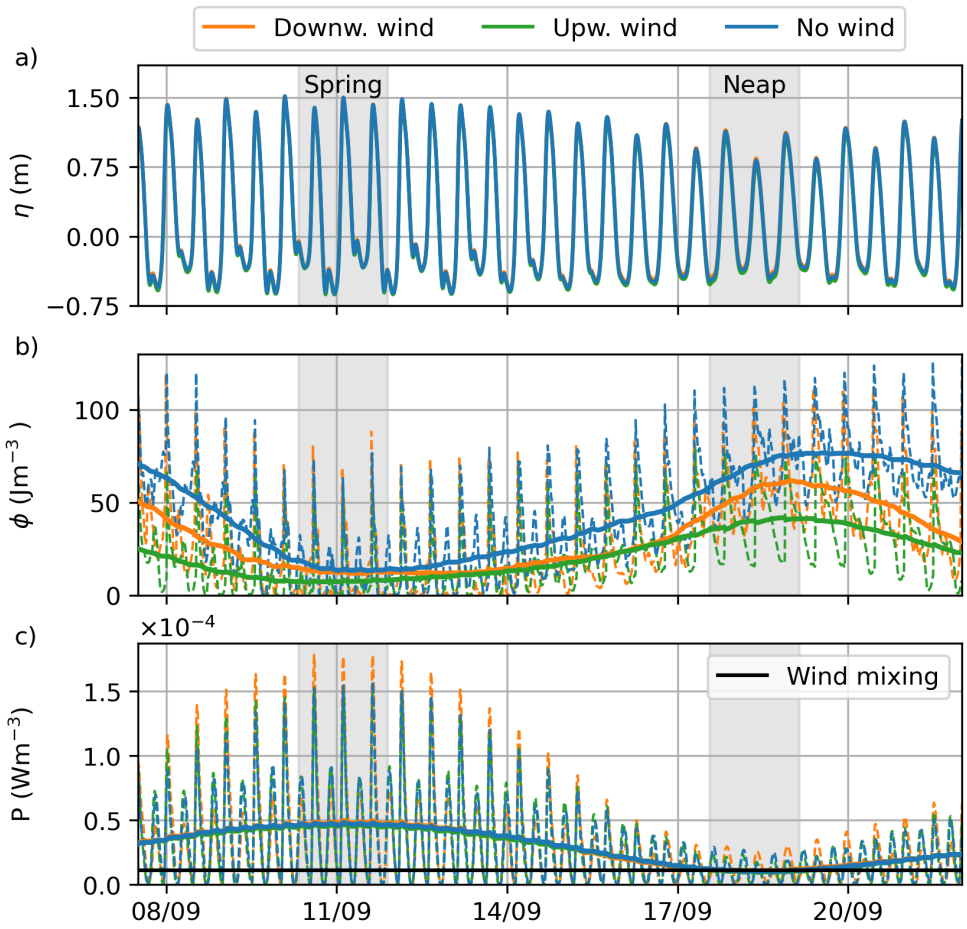

Figure 2.5: At 2 km downstream of the river mouth, time series are taken of the water level (a), the potential energy anomaly (Eq. 2.2) (b), and the tidal mixing (Eq. 2.5) (c) for the simulation without wind (blue), with downwelling winds (orange) and with upwelling winds (green). The thick solid lines indicate tidal averages. The solid black line indicates the wind mixing for a wind speed of 5 ms^{-1} (Eq. 2.6).

difference in water level between the different simulations (Figure 2.5a). The peaks in ϕ indicate the passing of the tidal plume fronts (Figure 2.5b). On spring tide, ϕ is relatively small for all three simulations, indicating that the plume is mainly well-mixed regardless of the wind conditions. In contrast, larger differences in ϕ are found between the different simulations on neap tide. In the absence of winds (blue lines), and thus when no wind mixing is present, the stratification is strongest. Under downwelling winds (orange lines), ϕ is larger due to the thickening of the plume than under upwelling winds (green lines), when the plume thins. Figure 2.5c shows that tidal mixing is similar for the three simulations. On spring tide, tidal mixing is 5 times stronger than during neap tide. For a wind speed of 5 ms^{-1} and an air density of 1.24 kgm^{-3}, we estimate a wind mixing power of 1.1×10^{-5} Wm^{-3} (Eq. 2.6) (black line). This is similar to the tidal mixing at neap tide (Figure 2.5c, around 18-19 September).

This different response to upwelling winds on neap and spring tide can be explained by estimating the mixing timescale during a spring-neap cycle using Eq. 2.4 and the tidally-averaged values of ϕ and P on spring and neap tide from Figure 2.5. On neap tide, we find a mixing timescale of 42 tidal cycles, exceeding the duration of a spring-neap cycle. Consequently, the plume has sufficient time to spread in the offshore direction on neap tide. On spring tide, however, we estimate a mixing timescale of only 3 tidal cycles. This shows the limited amount of time for the plume to spread offshore before it is mixed with the ambient sea water, and explains the different response between neap and spring tide.

To explain the different response to downwelling winds on neap and spring tide, cross sections of the tidally-averaged salinity in the mid-field plume are compared for the simulations without wind forcing (Figure 2.6a,b) and with downwelling winds

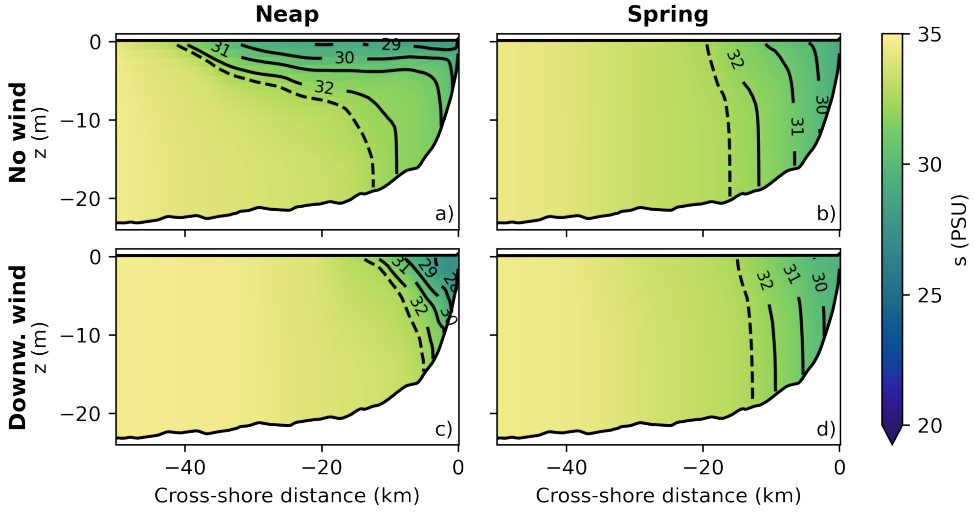

Figure 2.6: Cross-sectional contour plot of the tidally-averaged salinity during neap (left — a,c) and spring tide (right — b,d) without winds (top — a,b) and under downwelling winds (bottom — c,d). The dashed isohaline (32.5 PSU) is considered as the river plume boundary. The location of the cross sectino is shown in Figure 2.2.

(Figure 2.6c,d). On neap tide, when the plume is stratified, downwelling winds cause the isopycnals to steepen due to onshore-directed Ekman transport. Consequently, the plume is narrowed. On spring tide, however, the plume is vertically well-mixed due to stronger tidal mixing, and thus are the isopycnals already vertical. Since further tilting of the isopycnals results in unstable stratification and additional (convective) mixing, little narrowing of the plume is found under downwelling winds.

In summary, the wind-driven response of the Rhine River plume depends on the vertical plume structure. On neap tide, when the plume is strongly stratified, the wind-driven response is in accordance with Ekman dynamics. On spring tide, however, the stratification is weaker. Consequently, the plume is mixed before it can spread offshore under upwelling winds, while the plume does not narrow under downwelling winds since the isopycnals are already vertical.

2.5 Salinity-coordinate analysis

It was found that the plume structure in the near- to mid-field region strongly depends on the winds and tides. The question remains how changes in the near- to mid-field plume affect the wind-driven response of the far-field plume. Using Eq. 2.9 and 2.7, we compare the stratification and mixing rates for the different scenarios regardless of its position to analyse the connectivity between the different plume regions in time and (salinity) space. First, we evaluate the potential energy anomaly in salinity space to analyse the evolution of the stratification and to identify the different regions of the plume and their characteristic features (e.g., tidal plume fronts, tidal straining). Next, we evaluate the freshwater distribution in salinity space to investigate the mixing rates in the different plume regions.

2.5.1 Potential energy anomaly

Figure 2.7 shows the total potential energy anomaly (Eq. 2.3) and the potential energy anomaly expressed in salinity coordinates (Eq. 2.9). The total potential energy anomaly exhibits a semidiurnal cycle (Figure 2.7a-b). This is predominantly caused by variability of the stratification in the higher salinity classes ($S > 28$ PSU). The timing of this cycle corresponds to tidal straining, as observed by Simpson and Souza (1995); Fisher et al. (2002); de Boer et al. (2008). Stratification is minimal around LW. Between LW and HW, the surface currents are directed offshore, increasing the stratification. The stratification is maximum at HW. Between HW and LW, the stratification decreases due to the onshore-directed surface currents. For all cases, the stratification is stronger on neap tide than on spring tide.

On neap tide, high values of ϕ are found in the higher salinity classes (¿28 PSU) (Figure 2.7c,e,g), reflecting the strongly stratified mid- and far-field plume (see Figure 2.4). Under downwelling winds, ϕ is lower in the higher salinity classes, compared to the situation without wind. This is caused by the narrowing of the plume, reducing the stratified area (see Figures 2.3 and 2.4). ϕ is largest under upwelling winds, since the plume area expands in the offshore direction (see Figure 2.3 and 2.4). On spring tide (Figure 2.7d,f,h), we find relatively low values of ϕ in the higher salinity classes, reflecting that the mid- and far-field plume are mainly well-mixed (see Figure 2.4).

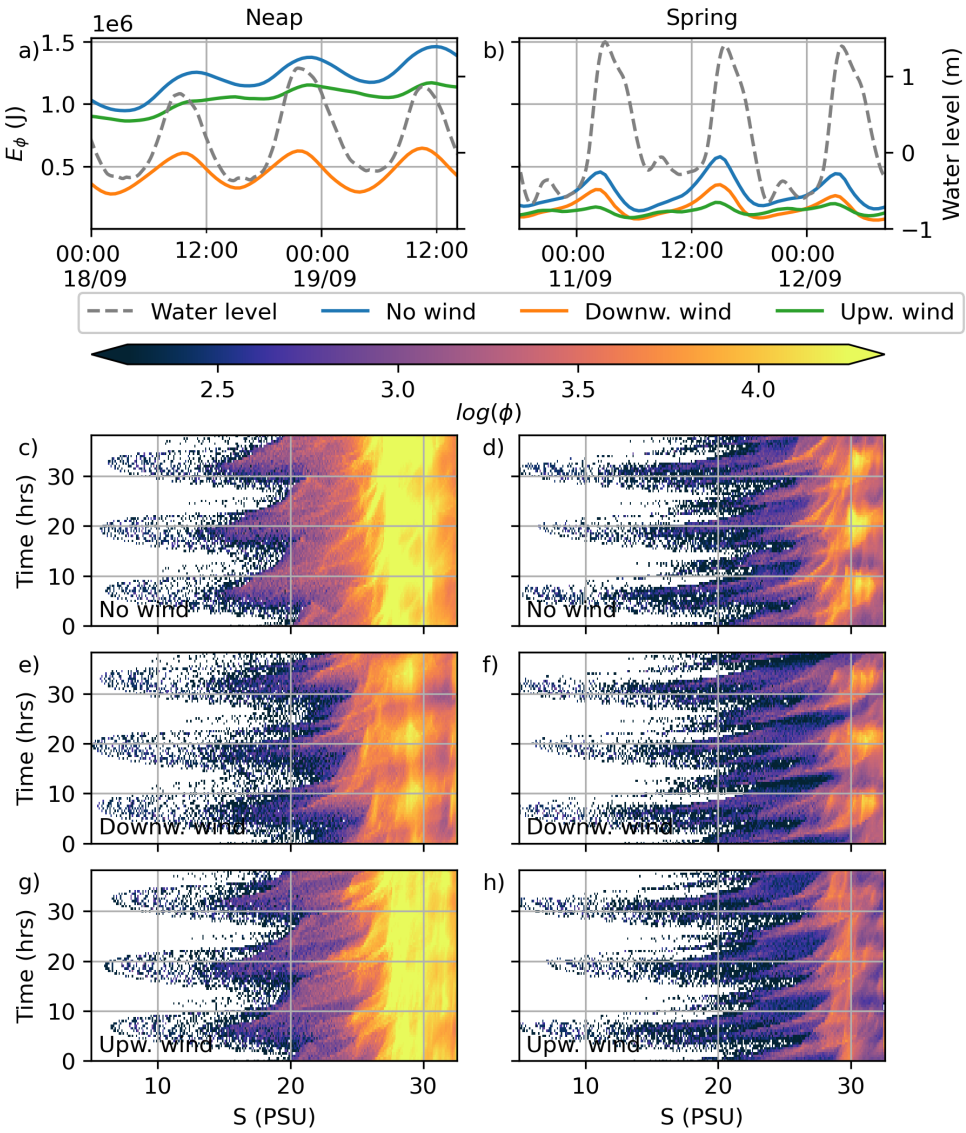

Figure 2.7: a,b) $E_\phi(t)$ per scenario. The dashed grey line indicates the water level. c–h) $\phi(s_l, t)$ for each simulation on neap (left) and spring tide (right). Each row depicts different wind conditions

The tidal plume fronts transfer freshwater to higher salinity classes, connecting the near-field plume with the mid- and far-field region. The tidal plume fronts correspond to the high values of ϕ between 20–25 PSU in Figure 2.7 (orangish areas) and are especially clear under downwelling winds or on spring tide, when a train of fronts was found (Figure 2.3 and 2.4). Every tidal cycle, two tidal plume fronts are formed. The first curve originates around LW, corresponds to the tidal plume front formed at LW and is advected southwards. The second curve corresponds to the tidal plume front formed north of the mouth and propagates northwards after LWS. On spring tide, the tidal plume fronts are mixed relatively fast, reaching higher salinity classes within a tidal cycle. On neap tide, contrastingly, the tidal plume fronts coalesce, forming the strongly stratified mid-field plume.

2.5.2 Freshwater distribution

Next, we determine the freshwater distribution for the different scenarios using Eq. 2.7, providing insight in the amount of mixing (Figure 2.8). Figures 2.8a and b show the tidally-averaged freshwater distribution over the salinity classes for neap and spring tide, respectively. In the absence of wind (blue lines), more freshwater accumulates in higher salinity classes on spring tide than on neap tide, indicating increased tidal mixing. The onset of winds significantly alters the freshwater distribution. Under downwelling winds (orange lines), a decrease in freshwater volume is found, especially in the higher salinity classes. This is mainly caused by a strong export of freshwater through the northern boundary, since alongshore transport is amplified by the downwelling wind (not shown here). Under upwelling winds (green lines), the freshwater content is also smaller than for the reference case. The total mixing is stronger due to wind-induced mixing and the larger surface area of the plume, which amplifies the effect of tidal mixing. The strong peak around 31 PSU, which is found at both neap and spring tide, corresponds to the remaining band of freshwater along the coast (see Figure 2.3c,f), which originated during the spin-up period. These coastal waters slowly mix over time with the shelf waters.

In Figure 2.8c–h, the time-dependent freshwater anomalies are shown for the different scenarios. Changes in the higher salinity classes (¿ 28 PSU) are most likely caused by the export and import of freshwater through the boundaries of our domain. Although this hinders the physical interpretation of what happens in these classes, we can still evaluate the transport of freshwater in the rest of the plume, where mixing rates are largest.

In the lowest salinity classes (¡20 PSU), the pulsed river outflow is clearly visible in all panels. Due to estuarine dynamics, the outflow and its salinity vary. The salinity of the outflow is lowest at LWS, just before the tidal currents turn. The outflow is fresher on neap tide due to lower estuarine mixing. The alongshore winds do not significantly influence the river outflow.

The positive anomalies between 20–28 PSU show the transfer of freshwater from the lower salinity classes (i.e. the near- to mid-field region in Figure 2.3) towards higher salinity classes (i.e. the mid- to far-field region in Figure 2.3). In the absence of winds (Figure 2.8c–d), freshwater is transferred quicker and to higher salinity classes on spring tide than on neap tide, due to stronger tidal mixing. The positive anomalies follow an exponential curve, indicating that mixing rates decrease in higher salinity

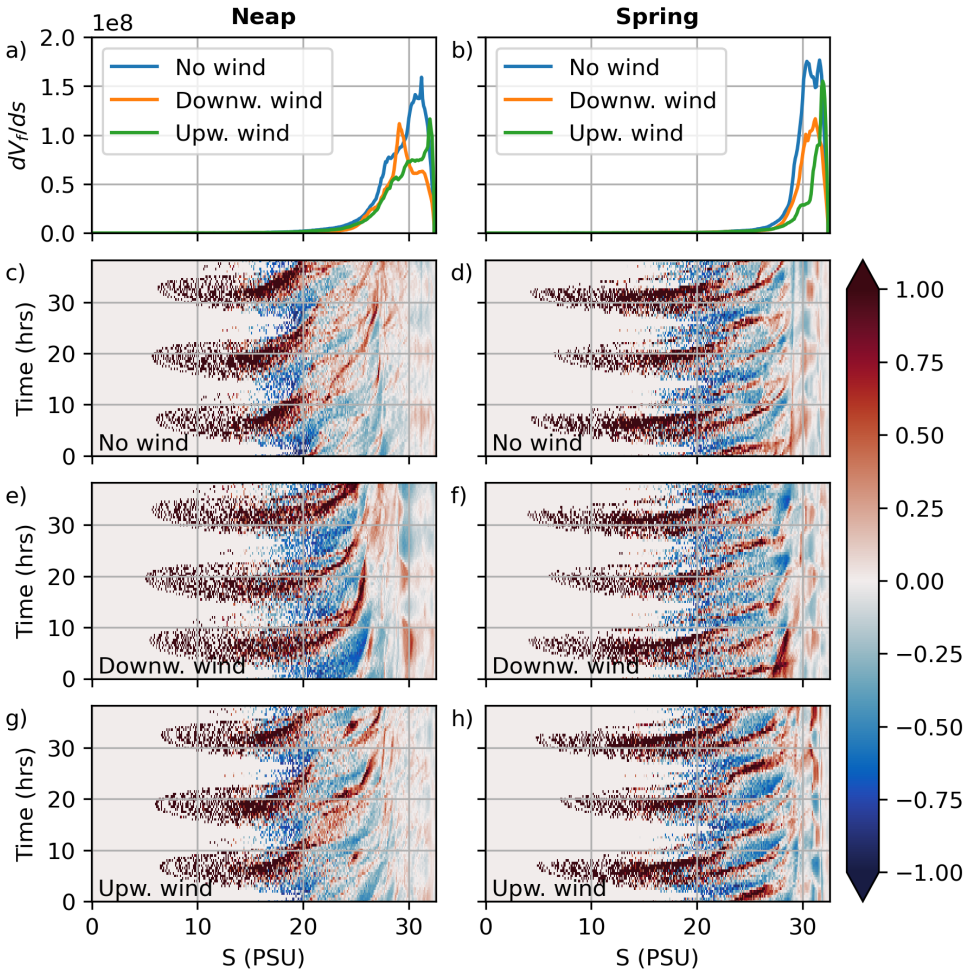

Figure 2.8: Freshwater volumes in salinity space on neap (left) and spring tide (right). a,b) Tidally-averaged freshwater distributions for neap and spring tide. c–h) Time-dependent freshwater anomalies w.r.t. tidally-averaged freshwater volume per salinity class for three different wind conditions: no wind (c–d), downwelling wind (e–f) and upwelling wind (g–h).

classes.

On neap tide, the positive anomaly originating from the outflow (starting around 20 PSU and developing towards 25 PSU) is more distinct under downwelling winds than in the absence of winds (Figure 2.8e–f). This reflects the formation of a train of separate tidal plume fronts (Figure 2.3b,e), while they coalesced in the absence of winds (Figure 2.3a,d). The positive anomaly vanishes 12 hours after the formation (around 25 PSU), indicating the tidal plume front leaves the domain.

On spring tide (Figure 2.8f), no significant changes in the freshwater distribution are found due to the onset of downwelling winds. Under upwelling winds (Figure 2.8g–h), the positive anomalies are more distinct than in the reference case. This reflects that the fronts are stronger since they were arrested by the wind. In contrast to neap tide (Figure 2.8e), the fronts are mixed before leaving the domain and the freshwater is transported towards higher salinity classes.

In summary, the salinity-coordinate analysis showed that tidal plume fronts transfer freshwater from the near-field plume towards the mid- to far-field plume. Their evolution is strongly influenced by winds and tides, affecting the downstream evolution of the plume. The strongest mixing is found in the lower salinity classes (i.e., the near- to mid-field plume).

2.6 Discussion

While different studies investigated the wind-driven response under alongshore winds (Fong and Geyer, 2001; Lentz, 2004; Whitney and Garvine, 2005; Lentz and Largier, 2006), they focused on the far-field plume and long timescales, and omitted or simplified the impact of tidal dynamics on the near-field region. Moreover, more recent work showed that the near- and mid-field region are also prone to wind-driven mixing (Kakoulaki et al., 2014; Kastner et al., 2018; Spicer et al., 2022). Therefore, it is important to understand the effect of tides and winds on the near- to mid-field region of the Rhine River plume, and how this affects the wind-driven response of the far-field plume. Here, we integrate our findings from the different analyses, discussing how the wind-driven response of the Rhine River plume is affected by tidal dynamics.

We find that the vertical plume structure is critical for the wind-driven response of the Rhine River plume. However, winds do not only modify the structure of the plume, but also change its position. Therefore, we expressed the potential energy anomaly in terms of salinity coordinates, building upon the work of Hetland (2005) who introduced the concept of salinity coordinates. This allows us to analyse the stratification regardless of the plume's position. We demonstrated that our new method can be used to identify the different regions of the plume and their characteristic features (e.g., tidal plume fronts, tidal straining) and directly compare the stratification under different wind conditions.

The state of the near- to mid-field region of the Rhine River plume, which is dominated by tidal plume fronts (Rijnsburger et al., 2021a), varies not only with the tidal conditions, but also strongly depends on the wind conditions. Tidal plume fronts are advected in the wind direction. Under downwelling winds, alongshore propagation is enhanced during the flood phase (northwards) and limited during the ebb phase (southwards), resulting in a train of fronts that reaches into the far-field region both

on neap and spring tide. In contrast, upwelling winds hinder the northward propagation of tidal plume fronts during flood and enhance southward propagation during ebb. As a result, the fronts do not escape the mid-field region, again both on neap and spring tide.

These changes in plume structure are critical for the downstream evolution of the plume. Our analysis using salinity coordinates showed how freshwater is transferred from the near-field plume, where mixing rates are highest, to the far-field plume via the tidal plume fronts. Although smaller mixing rates are found in the far-field plume and relatively little change in the freshwater distribution, the position and stratification varies strongly between the different scenarios.

On neap tide, when tidal mixing is weaker and the far-field region is stratified, the wind-driven response is in accordance with Ekman dynamics. In agreement with Whitney and Garvine (2005) and Lentz and Largier (2006), the plume is confined against the coast and thickens under downwelling winds. Under upwelling winds, the river plume is detached from the coast, as also observed by Lentz (2004). Following the mechanism described by Fong and Geyer (2001), the plume thins as it spreads offshore. The Rhine River plume is different from other plumes in that tidal currents move the plume on- and offshore during a tidal cycle (Figure 2.2), which induce a semidiurnal cycle in the stratification (Figure 2.7a), as also observed by Souza and Simpson (1996).

On spring tide, however, the far-field plume is mainly well-mixed due to stronger tidal mixing. In contrast to neap tide, the plume is not narrowed due to downwelling winds. This is in agreement with Lentz and Largier (2006), who observed that the plume width does not change if the plume is vertically well-mixed. Since the far-field plume is vertically well-mixed, downwelling winds will not tilt the isopycnals any further, as this would result in unstable stratification and additional mixing. However, here tidal mixing homogenizes the water column, while they found wind mixing was the cause. Under upwelling winds, the near-field plume is only weakly stratified. In contrast with Fong and Geyer (2001) and Lentz (2004), we find limited offshore displacement of the plume. Weak stratification and stronger tidal mixing results in shorter mixing timescales. As a result, the plume is mixed with ambient sea water before freshwater can be transported offshore.

Conversely, wind-driven changes in plume structure affect the impact of tidal mixing during a spring-neap cycle. In agreement with Simpson et al. (1993), who observed a fortnightly cycle in the stratification, the mid- to far-field region is stratified on neap tide, but mainly well-mixed on spring tide due to the variations in tidal mixing. However, as shown by Hetland (2005), a smaller plume area must be compensated by stronger wind mixing to obtain the same freshwater flux. Here, we find that the same effect holds for tidal mixing instead of wind mixing, affecting the spring-neap variability of the Rhine River plume. As the plume spreads offshore under upwelling winds, the surface area of the Rhine River plume increases. Consequently, the plume is more susceptible to tidal mixing, and thus, larger changes in stratification are found between spring and neap tide. However, under downwelling winds, when the plume is narrower, the surface area is smaller. This reduces the impact of the spring-neap variability in tidal mixing on the stratification.

2.7 Conclusions

In summary, the response of the frictional, tidally-pulsed Rhine River plume to alongshore winds varies strongly during a spring-neap cycle. The plume's structure is a result of the competition between mixing and straining, induced by both winds and tides. On neap tide, when tidal mixing is weaker and consequently the far-field region is stratified, the wind-driven response is in accordance with Ekman dynamics. The plume is confined against the coast and thickens under downwelling winds (SW), but spreads offshore, thins and detaches from the coast under upwelling winds (NE). On spring tide, however, the Rhine River plume is mainly well-mixed due to stronger tidal mixing. Consequently, the plume does not narrow in response to downwelling winds, since further tilting of the isopycnals only induces additional mixing. Under upwelling winds, the plume is mixed before it can spread offshore.

In turn, the spring-neap variability of the plume is affected by the wind-driven changes in plume structure. The Rhine River plume is less sensitive to variations in tidal mixing during a spring-neap cycle under downwelling winds, due to stronger stratification and a smaller interfacial area. In contrast, the thinner and larger plume under upwelling winds is more susceptible to changes in tidal mixing.

Hence, the phasing of tides and winds determines the state of the river plume. Although winds are more variable than assumed in this study and the resulting response of the far-field region might be less pronounced, the near- and mid-field plume are also sensitive to winds and tides. Changes in these regions affect the downstream evolution of the plume. Therefore, it is important to consider these implications for future work on coastal processes and the transport of freshwater, sediments, nutrients, and pollutants, for example.

CHAPTER 3

The impact of a river plume on sea-level variability in a shallow shelf sea

ABSTRACT

While river plumes are known to influence ocean properties and circulation, their impact on sea-level variability is poorly understood, especially on shorter timescales and in shallow coastal and shelf seas. In this study, we investigate the effect of the Rhine River plume on sea-level variability along the Dutch coast using a high-resolution hydrodynamic model. By comparing baroclinic and barotropic simulations, we isolate the steric contribution of the plume to sea-level variability and assess its spatial and temporal characteristics. The Rhine River plume induces a positive anomaly in steric height, elevating the annual mean sea level along the Dutch coast. Near the river mouth, this signal exhibits strong tidal variability driven by the tidally-pulsed outflow, while slower fluctuations correlate with variations in river discharge. These steric changes modulate the tidal signal, leading to a decrease in tidal amplitude. Farther downstream, the steric variability diminishes due to mixing, and no significant effect on tidal sea-level variability is observed. Comparison with satellite altimetry reveals improved agreement when the river plume is included, indicating its influence on sea-level variability and highlighting the necessity to properly resolve river plumes in models. Our results show that even the plume of a moderate river like the Rhine River plume can affect sea-level variability, underscoring the importance of taking river plume dynamics into account in coastal sea-level studies.

3.1 Introduction

Climates are changing globally due to the continuous emission of greenhouse gasses from human activities (IPCC, 2023a). As a consequence, sea levels are rising faster and faster (IPCC, 2023b). IPCC (2023b) projected a global-mean sea-level rise of up to 1.01 m by 2100 mainly caused by ocean warming and melting glaciers and ice sheets. Consequently, low-lying but densely populated coastal areas around the world are threatened by coastal flooding due to higher extreme water levels (McGranahan et al., 2007; Muis et al., 2016; Vousdoukas et al., 2018; Tebaldi et al., 2021). This is not only caused by sea-level rise, but also due to (the interaction with) numerous coastal processes that act on different spatial and temporal scales, such as tides, storm surges and river runoff (Woodworth et al., 2019). Hence, there is an increasing need to understand and quantify processes contributing to sea-level variability; partly for (extreme) water level forecasts and partly to distinguish them from long-term, climate-related signals.

When river runoff enters the ocean, buoyant water bodies are formed – so-called river plumes. The interaction between the ocean and river plumes is highly dynamic, strongly affecting the ocean circulation and the mixing and transport of freshwater (Horner-Devine et al., 2015). In the southern North Sea, for example, river runoff of the Rhine, Ems, Weser, and Elbe rivers drives a coastal current along the Dutch and German coast (Huthnance, 1991; Ricker and Stanev, 2020). The river plumes play an important role in the transport of suspended matter (Pietrzak et al., 2011), such as sediments, nutrients and pollutants. The dynamics of river plumes are extensively studied using models (e.g. Berdeal et al., 2002; Choi and Wilkin, 2007) and observations (e.g. de Boer et al., 2009; Flores et al., 2017; Frey and Osadchiev, 2021). The spreading of river plumes is primarily driven by the Earth's rotation (Yankovsky and Chapman, 1997), wind-driven (Ekman) transport (Fong and Geyer, 2001; Lentz, 2004), tidal currents (Simpson, 1997; Horner-Devine et al., 2009) and the induced (horizontal and vertical) mixing associated with these processes. However, the impact of river plumes on sea-level variability has received relatively little attention.

In theory, the sea-level change due to river runoff consists of a manometric (or mass) component and a steric component (Jordà and Gomis, 2013; Gregory et al., 2019). Using a simple exercise based on the Amazon River, Durand et al. (2019) suggests that river runoff could significantly impact the global mean sea level only because of the mass added to the ocean. However, this manometric contribution is expected to be weak on local to regional scale, since river discharge varies more slowly than barotropic adjustment takes. This effect can be locally enhanced when water is trapped in semi-enclosed basins or seas, for example (Volkov et al., 2016). Furthermore, river runoff will change the density of the coastal ocean, since the riverine water is fresher and, therefore, lighter than the saltier ocean water. This effect is called the steric component. On local to regional scale, the steric contribution is believed to be stronger than the mass component, as the adjustment through baroclinic processes takes longer (Durand et al., 2019). However, in shelf and coastal seas where the depth is limited, steric changes are often considered to be negligible.

In practice, sea-level variability induced by river plumes is hard to observe. Since plumes are usually confined against the coast by Earth's rotation, they are hard to be sampled using conventional satellite radar altimetry due to the contamination of

the radar waveforms by reflections from land (Vignudelli et al., 2019; Durand et al., 2019). Let alone that to isolate the signal, accurate background models are required to remove the non-plume water level signals. Vinogradov and Ponte (2011) suggested that river runoff is among the reasons for the observed differences between water levels obtained using conventional low-resolution mode altimetry and tide gauges. Moreover, how the signal of river plumes is reflected in tide gauge data remains a key question.

A number of studies investigated the impact of river runoff on the sea level. Using a statistical analysis based on tide gauge data, Meade and Emery (1971) found that river discharge explains between 20% and 31% of interannual sea-level variability along the eastern coasts of the United States. Piecuch et al. (2018) derived a theoretical halosteric sea-level anomaly based on the river discharge, which supports the findings of Meade and Emery (1971) and predicts a positive sea-level anomaly up to 10 cm for the World's largest rivers. The regional modelling study of Giffard et al. (2019) shows how steric changes induced by the Amazon River cause an increase of the mean dynamic topography of +11 cm at the river mouth and +3.3 cm around the Caribbean Archipelago, while little response to seasonal variability in river discharge was found. More recently, global modelling studies by Piecuch et al. (2018) and Chandanpurkar et al. (2022) showed how river discharge induces sea-level variability on seasonal timescales.

The above studies show that river runoff can induce substantial sea-level variability on monthly and longer timescales. However, the transport and mixing of freshwater in river plumes is known to be highly dynamic (Horner-Devine et al., 2015), which cannot be resolved by the relatively coarse regional and global models that are used. Conversely, higher-resolution operational storm surge forecast models are often of barotropic nature, excluding river runoff. Therefore, high-resolution modelling is required to investigate the effect of river plume (dynamics) on sea-level variability. This insight could potentially explain part of the mismatch between (offshore) satellite altimetry and (coastal) tide gauge data (Vinogradov and Ponte, 2011) and be relevant for the assessment of (changing) extreme water levels (Woodworth et al., 2019).

In this study, we focus on sea-level variability in the Southern North Sea along the low-lying coast of the Netherlands (Figure 3.1). The North Sea is a shallow shelf sea, where sea-level variability is primarily driven by tides and surges. Along the Dutch coast, the coastal circulation is strongly influenced by the Rhine River plume (in literature also referred to as the Rhine ROFI (Region Of Freshwater Influence) (Simpson et al., 1993)). The Rhine River plume is a frictional, tidally-dominated river plume, the structure of which depends on the phasing of the tides and winds (Pietrzak et al., in prep.). Due to the interaction between the tidally-pulsed river outflow and the alongshore tidal currents, tidal plume fronts are formed every tidal cycle (Rijnsburger et al., 2021a). These fronts recirculate in the strongly stratified mid-field region of the plume. Farther downstream, in the far-field plume, the plume moves on- and offshore under the influence of elliptical tidal currents, which are, in turn, a result of the interaction between the stratification and the tides (Visser et al., 1994; Souza and Simpson, 1996; de Boer et al., 2006). Here, we investigate the contribution of the river plume dynamics to sea-level variability. To do this, we use simulations from a high-resolution 3D model of the North Sea that is able to resolve the dominant dynamics of the Rhine River plume (Chapter 2).

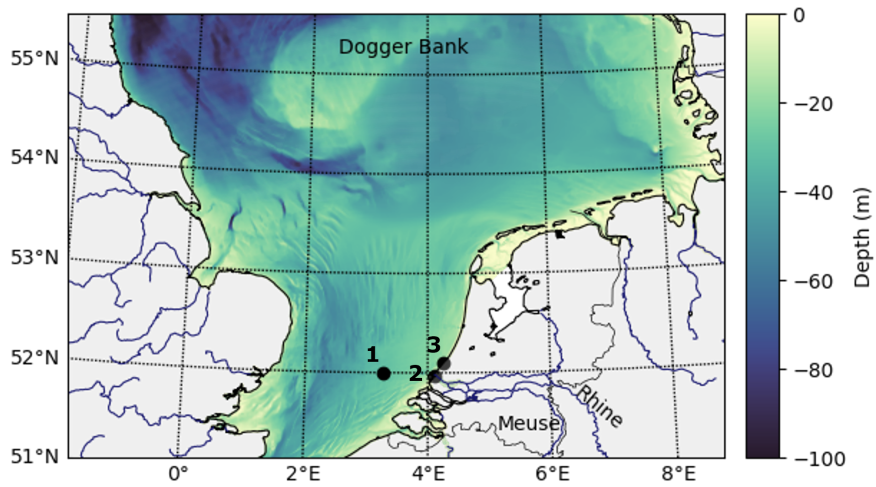

Figure 3.1: Overview of Southern North Sea with the Dogger Bank in the north, the British coast in the west, the Dutch, German and Danish coastlines in the east and the Rhine and Meuse Rivers flowing into the North Sea near Hoek van Holland. The black dots indicate the tidal stations of (1) Europlatform, (2) Hoek van Holland and (3) Scheveningen.

This paper is structured to systematically investigate the impact of the Rhine River plume on sea-level variability along the Dutch coast. Section 3.2 describes the numerical modelling approach, including the setup of the baroclinic (including the river plume) and barotropic runs (excluding the river plume) that form the basis of this study. In Section 3.3, we describe the methods used to evaluate the influence of the river plume on sea-level variability, including the definition of the freshwater thickness used to locate the river plume, an analytical framework for river runoff-induced sea-level changes, and the definitions of steric, halosteric, and thermosteric height. Section 3.4 focuses on understanding the Rhine River plume and its influence on steric height. We also compare modelled sea level with satellite altimetry to provide an initial indication of the plume's role in sea-level variability. Section 3.5 examines the spatio-temporal variability in steric height, in order to understand the potential of the river plume to affect sea-level variability. In Section 3.6, we evaluate the steric contribution to sea-level variability by comparing the baroclinic and barotropic model runs at Hoek van Holland and Scheveningen (locations (2) and (3) in Figure 3.1). Finally, we discuss our results and their implications in Section 3.7.

3.2 Numerical modelling approach

3.2.1 Model setup

In this study, the 3D Dutch Continental Shelf Model is used. The model setup was developed and validated by Zijl et al. (2018) and previously used to study the Rhine River

plume (Chapter 2). The model domain covers the entire northwest European shelf (5°W–13°E and 43–64°N), with a varying grid size, decreasing down to 200 m along the Dutch coast. At the open ocean boundaries, water levels, salinity and temperature are prescribed. For the rivers, the climatological river runoff from European Hydrological Predictions for the Environment (Donnelly et al., 2016) is included, except for the rivers in the Netherlands for which the historical daily discharge is used (available at https://waterinfo.rws.nl/). Furthermore, meteorological forcing, including winds, air pressure and heat exchange at the surface, is applied, which is obtained from the ECMWF's ERA5 reanalysis dataset (Hersbach et al., 2018). A spatially-varying bottom roughness is used to calibrate the water levels (Zijl et al., 2018). This model has already been extensively validated (Zijl et al., 2018, and Chapter 2), including for water levels, flow velocities, salinity and cross-shore density gradients. These studies show that that water levels and the key features of the Rhine River plume such as tidal straining and the formation of tidal plume fronts are accurately reproduced. We refer to Zijl et al. (2018) and Chapter 2 of this thesis for more details regarding the model setup and validation and to Kernkamp et al. (2011) for the governing equations and their discretizations.

3.2.2 Model validation at Hoek van Holland

For this study, we perform an additional validation at Hoek van Holland - a tide gauge station located near the river mouth (location (2) in Figure 3.1). When comparing the modelled and observed water levels for the entire year of 2019, we find a bias of -5.1 cm and a RMSE of 8.2 cm at Hoek van Holland. The tidal signal is evaluated by comparing the reconstructed tidal signals, obtained by a harmonic analysis of the modelled and measured water levels at Hoek van Holland using UTide (Codiga, 2011). A RMSE of 6.7 cm is found for the tidal signal. The RMSE of the surge, which is defined as the difference between the total water level and the tidal signal, equals 5.4 cm. This shows that sea-level variability induced by tides and by atmospheric and buoyant forcing are reproduced with similar accuracy at Hoek van Holland. These values are similar to what was found for different periods (Zijl et al., 2018, and Chapter 2).

In addition, we evaluate how the tidally-pulsed river outflow and sea level are reproduced at Hoek van Holland during three selected spring-neap cycles with different discharge conditions (Figure 3.2). The winds are relatively calm (< 10 ms^{-1}) during these periods, and the river discharge is either low (1000 m^{3}s^{-1} - Figure 3.2 - left column), average (2000 m^{3}s^{-1} - Figure 3.2 - middle column) or high (3000 m^{3}s^{-1} - - Figure 3.2 - right column). For all periods, good agreement between the modelled and measured water levels is found. The small difference in RMSE between the different periods is mainly associated with varying wind conditions, rather than the impact of varying discharge conditions.

Validation of the modelled steric height would require measurements of temperature and salinity throughout the entire water column. However, only salinity measurements near the surface (at -2.5 m NAP) are available. A comparison of these measurements with the modelled salinity (Figure 3.2g–i) shows that the tidal variability, which is an indicator for the tidally-pulsed outflow, is reasonably well reproduced, especially given the relatively coarse representation of the estuary. Figure 3.2 shows that the model is able to reproduce the tidally-pulsed outflow and sea-level variability

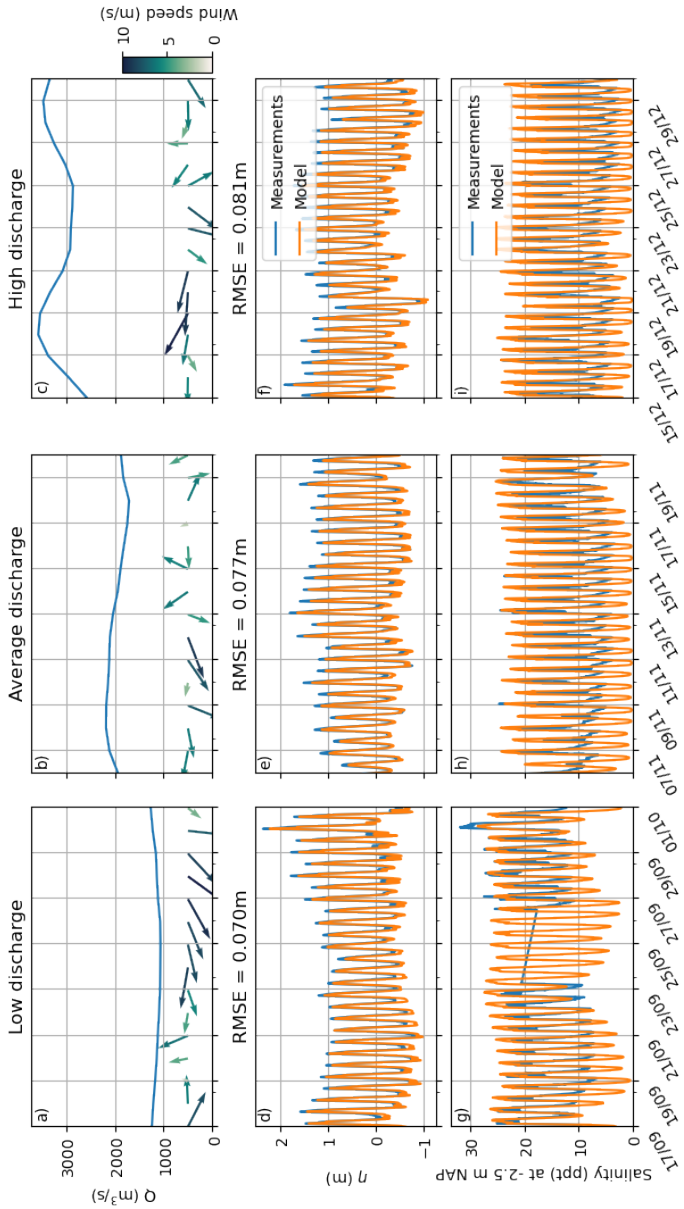

Figure 3.2: Model validation at Hoek van Holland during two-week periods with (left) low (1000 m^3s^{-1}), (middle) average (2000 m^3s^{-1}), and (right) high discharge conditions (3000 m^3s^{-1}). a-c) discharge Q at Lobith, coloured vectors indicate the prevailing winds. d-f) comparison between the modelled and measured sea level η, the RMSE is provided for each period. g-i) comparison between the modelled and measured salinity at -2.5 m NAP.

at Hoek van Holland well under different discharge conditions. Based on this and the outcomes of Zijl et al. (2018) and Chapter 2, we therefore judge the model is fit to assess the impact of the Rhine River plume on sea-level variability.

3.2.3 Model simulations

To investigate the effect of the Rhine River plume on the sea-level variability, we conduct two model simulations. First, we perform a hindcast for 2019. This simulation includes all forcing as described before. Second, we run a perturbed simulation, where river runoff is still included but buoyant forcing is excluded by setting a constant density of 1025 kgm^{-3} in the whole domain. In this case, no river plume is formed. We refer to the different simulations as the baroclinic and barotropic run, respectively.

In order to verify that the baroclinic signal can be isolated by comparing the baroclinic and barotropic run and that no large-scale changes in tidal forcing are induced, water levels are compared at Europlatform (EURPFM) – an offshore tide gauge station located 60 km southwest of the river mouth (location (1) in Figure 3.1). Since this location is located outside the river plume, we expect little difference in sea-level variability between both runs due to limited variations in steric height here.

In Table 3.1, we compare the total variance, which is based on the sea level as computed by the model, and the tidal variance, which is based on the tidal signals obtained by a harmonic analysis using UTide (Codiga, 2011). No significant differences in either total or tidal variance are found between the baroclinic and barotropic model run. This suggests that the tides are not significantly affected by including baroclinic effects, and differences between the baroclinic and barotropic run in the Rhine River plume can be assumed to be attributable to other processes.

Table 3.1: Comparison of MSL, total sea-level variance and tidal variance between the baroclinic and barotropic run at Europlatform.

Run	MSL (m)	Total variance (m^2)	Tidal variance (m^2)
Baroclinic run	0.0058	0.368	0.331
Barotropic run	0.0055	0.376	0.340

3.3 Methods

In this study, we use different measures to assess the effect of the river plume on sea-level variability, which we introduce in this section. First, we define the freshwater thickness, which is used for determing the location of the river plume. Next, we explain analytically how river runoff induces sea-level changes. Lastly, we define the steric height and the halo- and thermosteric components.

3.3.1 Freshwater thickness

For determining the location of the river plume, we use the freshwater thickness h_f (m) (Eq. 3.1). h_f can be seen as the thickness a layer of pure freshwater would have if

there would be no vertical mixing between (salt) ocean water and (fresh) river water.

$$h_f = \int_{-h_p}^{\eta} \left[\frac{S_0 - S}{S_0} \right] dz \,, \tag{3.1}$$

where h_p is the plume depth (m) and S_0 the reference salinity (32.5 PSU). The 32.5 PSU isohaline is considered as the river plume boundary in this study and also used to determine the plume depth.

3.3.2 Sea-level changes due to river runoff

When river runoff enters the ocean, the ocean mass changes due to the addition of extra water and the density changes due to the inflow of freshwater. When assuming hydrostatic pressure, the resulting sea-level change can be described using Eq. 3.2 (Gregory et al., 2019).

$$\underbrace{\frac{\partial \eta}{\partial t}}_{\text{Sea-level changes}} = \underbrace{\frac{1}{\rho_0 g} \frac{\partial P_b}{\partial t}}_{\text{Manometric changes}} \underbrace{- \frac{1}{\rho_0} \int_{-H}^{\eta} \frac{\partial \rho \left(S,T,p\right)}{\partial t} dz}_{\text{Steric changes}} \,, \tag{3.2}$$

where η is the sea level (m), ρ_0 the reference density (kgm^{-3}), g the gravitational acceleration (ms^{-2}), P_b the bottom pressure (Nm^{-2}), H the water depth (m), ρ the density (kgm^{-3}), T the water temperature (°C), S the salinity (PSU) and p the pressure (Nm^{-2}). Sea-level change consists of a manometric and a steric component. The manometric component represents the change in sea level due to the changing ocean mass (i.e., the barystatic effect when globally averaged). The manometric component is of a barotropic nature, i.e. the addition of mass causes an external pressure gradient. The resulting (barotropic) adjustment of the sea level is relatively fast. The steric component is the sea-level change due to the changing water density, caused by variations in water temperature and/or salinity. The steric effect is of a baroclinic nature, i.e. changes in density induce (much smaller) internal pressure gradients. As a consequence, the (baroclinic) adjustment of the sea level to steric changes is relatively slow.

3.3.3 Steric height

As we focus on the river plume, which induces density gradients, we limit our analysis to the steric component of sea-level changes. The steric height is calculated as:

$$h_{steric} = -\frac{1}{\rho_0} \int_{-h}^{\eta} \left[\rho \left(S,T,p\right) - \rho_0 \right] dz \,. \tag{3.3}$$

We evaluate the steric height with respect to the density that is used in the barotropic run ($\rho_0 = 1025\,\text{kgm}^{-3}$). Note that a small tidal signal can be produced due to the integration over the entire water column, even when the density is constant in time.

The steric height can be separated into a halosteric and a thermosteric contribution, which are induced by variations in salinity and temperature, respectively. Since

both temperature and salinity vary significantly in the North Sea, we calculate these different contributions using Eqs. 3.4 and 3.5 to evaluate their distinct roles.

$$h_{halo} = -\frac{1}{\rho_0}\int_{-h}^{\eta}\left[\rho\left(S,\bar{T},p\right)-\rho_0\right]dz\,. \tag{3.4}$$

$$h_{thermo} = -\frac{1}{\rho_0}\int_{-h}^{\eta}\left[\rho\left(\bar{S},T,p\right)-\rho_0\right]dz\,. \tag{3.5}$$

The overbars represent the annual mean depth-averaged values.

3.4 Understanding the Rhine River plume

To investigate the effect of the Rhine River plume on sea-level variability, we start by analyzing the tidal and plume dynamics and compute the resulting change in steric height. This provides the context necessary for understanding how the river plume may affect sea-level variability. Next, we evaluate the role of the river plume in the model's representation of sea-level variability by comparing the modelled sea levels with satellite altimetry data, providing a first indication that the river plume influences sea-level variability.

3.4.1 Tidal and plume dynamics

To understand the tidal and plume dynamics and the resulting change in steric height, we evaluate the evolution of the sea level, freshwater thickness and steric height during a tidal cycle (Figure 3.3). The instantaneous sea level is dominated by the tidal signal (Figure 3.3a-d). The tidal Kelvin wave with a semidiurnal tidal cycle can be clearly seen propagating anticlockwise and its amplitude decreases in the offshore direction.

The river plume strongly interacts with the tides (de Boer et al., 2006; Rijnsburger et al., 2021a, and Chapter 2). This can be seen from the freshwater thickness (Figure 3.3e-h). The freshwater layer is thickest near the river mouth. The river outflow is deflected towards the right due to Earth's rotation, forming a river plume in which freshwater is transported northwards under the influence of tides and winds (Rijnsburger et al., 2021a, and Chapter 2). Due to mixing, the freshwater thickness reduces in the northward direction.

The river plume induces an increased steric height along the coast (Figure 3.3i-l). The steric height mainly depends on the amount of freshwater in the water column (i.e. the freshwater thickness), and thus also varies during a tidal cycle due to interaction pf the river plume with tides and winds. The steric height is largely independent from the stratification (not shown here). However, it is known that the stratification affects the mixing and transport of freshwater (Horner-Devine et al., 2015), thereby indirectly influencing the steric height. Offshore, no variability in steric height is found on tidal timescales.

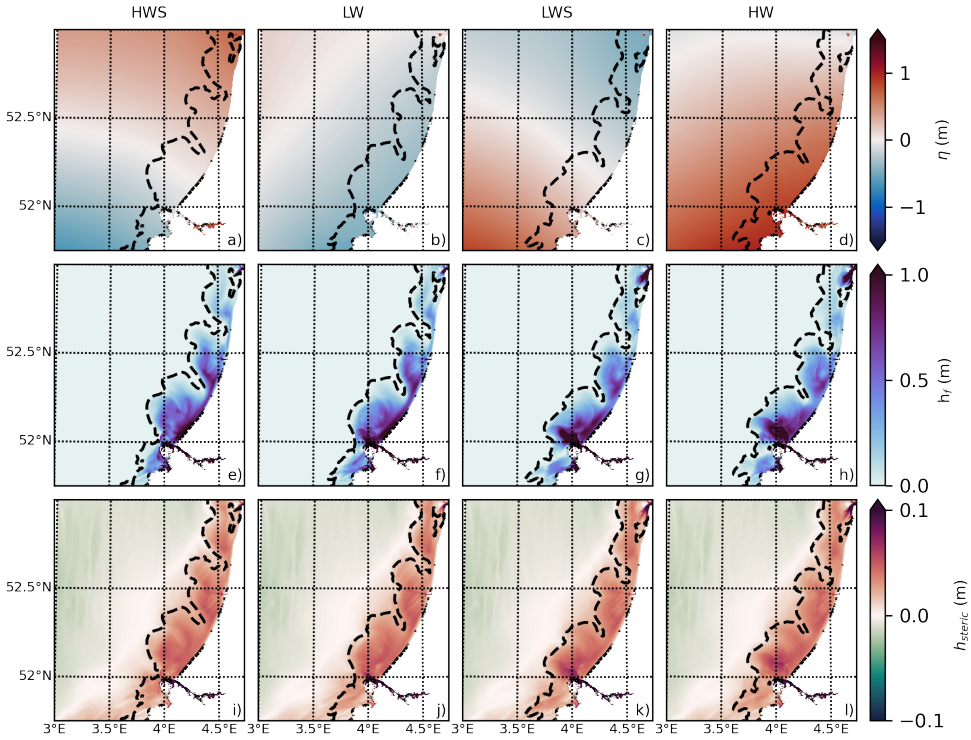

Figure 3.3: Variability in the Rhine River plume during a tidal cycle: a-d) sea level η (m), e-h) freshwater thickness h_f (m), and i-l) steric height h_{steric} (m). The dashed line represents the 32.5 PSU contour, indicating the Rhine River plume.

3.4.2 Comparison with satellite altimetry and the role of the river plume

If we compare SAR altimeter-derived sea levels with modelled sea levels from the baroclinic and barotropic runs, however, we find a first indication that the Rhine River plume influences sea-level variability. Hereto, we use SAR altimeter-derived sea levels acquired by Sentinel-3B (Donlon et al., 2012) along relative orbit 370, which ground track crosses the near-field region of the Rhine River plume (red line in Figure 3.4a). In this study, the altimeter-derived water level is reconstructed by applying a processing algorithm that starts from Level-1a products (EUMETSAT for Copernicus, 2022), oversamples the L1b waveforms in range and disregard parts of the waveform's trailing edges due to land contamination (Ehlers et al., 2023; Schlembach et al., 2023), as we aim to retrieve the water levels close to the coast. Furthermore, we apply all necessary corrections as in Dinardo et al. (2018, see their Eq. 4).

Figure 3.4b shows the averaged difference between the modelled and altimeter-derived water levels for the baroclinic and barotropic run. We compare three different metrics to evaluate the effect of the river plume. First, the mean difference between the modelled and altimeter-derived water levels is -4.2 cm for the baroclinic run and

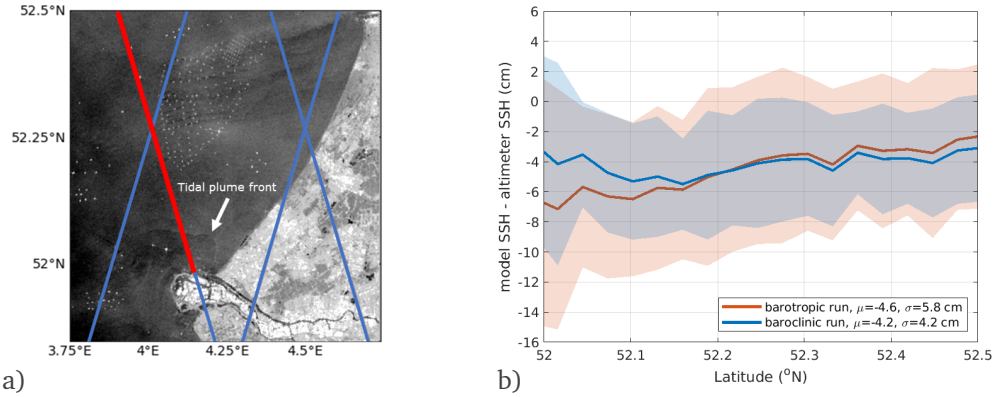

Figure 3.4: a) SAR image taken by Sentinel 1, showing the tidal plume front (indicated by the white arrow). The blue lines indicate the repeat orbit of Sentinel 3A and B. The data along the red segment is used in panel b. b) The difference between the modelled and altimeter-derived water levels for the baroclinic (blue) and barotropic run (red) along Sentinel-3B's ground track of relative orbit 370 (red segment in panel a) averaged over one year. The altimetry data is averaged in the along-track direction (340 m resolution onto 3.4 km) to diminish the amount of random noise. The solid lines represent the mean difference of the 14 overpasses in 2019, the shaded area represents the one-standard deviation.

-4.6 cm for the barotropic run. This likely includes differences in vertical datums between the model and altimeter, but also shows that including the river plume improves the representation of the average water level. Second, we find an increased slope in the along-track direction for the barotropic run, with larger differences near the coast. Third, the standard deviation is smaller for the baroclinic run ($\sigma = 4.2$ cm) than for the barotropic run ($\sigma = 5.8$ cm), indicating that the variability is better represented by the baroclinic run. These three metrics indicate that the modelled water levels are better represented along the satellite track when the river plume is included, providing a first indication that the Rhine River plume influences sea-level variability.

3.5 Spatio-temporal variability in steric height

After having found a first indication of the Rhine River plume's potential influence on sea-level variability, we focus in this section on the spatio-temporal variability in steric height. Using the output of the baroclinic run, we first assess both annual mean fields and seasonal variability of the freshwater thickness, steric height and sea level, describing the mean background state of the Rhine River plume. Next, we focus on the seasonal variability in steric height. Lastly, we zoom in on Hoek van Holland — a tide gauge station near the river mouth where the largest steric changes are expected because of the fresh river outflow — to examine the temporal variability in steric height in more detail. These analyses provide insight into how the river plume influences the steric height, and it's potential effect on sea-level variability.

3.5.1 Annual mean fields and seasonal variability

We begin by analyzing the annual mean freshwater thickness, steric height, and sea level, as well as the seasonal variability of each variable, which is represented by the standard deviation of the monthly-averaged fields (Figure 3.5). The freshwater thickness (Figure 3.5a) shows the location of the Rhine River plume along the coast (indicated by the area for which $h_f > 0$). Most freshwater is found close to the coast, and the variability, indicated by the contour lines, decreases in the cross-shore direction.

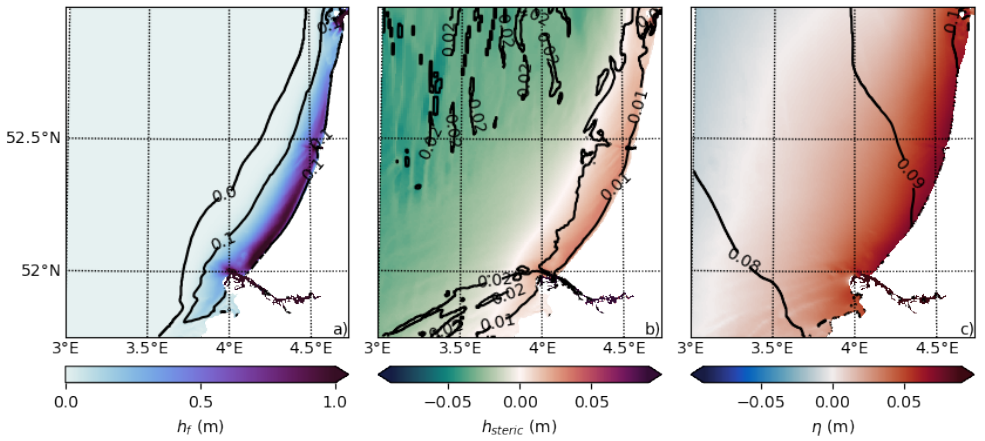

Figure 3.5: Yearly-averaged a) freshwater thickness h_f (m), b) steric height h_{steric} (b), and c) sea level η (m). The contour lines indicate the standard deviation of the monthly-averaged fields.

The river plume induces an increased steric height along the coast of approximately 10 cm (Figure 3.5b). It is noteworthy that the offshore variability in steric height is similar to the variability within the river plume, indicating that seasonal steric changes are not only driven by the river plume but also by large-scale variability (Figure 3.5b).

Figure 3.5c shows an increased annual mean sea level along the coast. The increase in sea level along the coast is comparable to the increase in steric height, indicating the significant contribution of the river plume to the annual mean sea level. When considering the seasonal variability, however, the contour lines indicating sea-level variability (Figure 3.5c) do not correspond to contour lines indicating the variability in steric height (Figure 3.5b). This indicates that the seasonal variability of the river plume is not the dominant driver of seasonal sea-level variability. Nevertheless, since the variability in steric height is of the same order of magnitude as the sea-level variability, the river plume cannot be neglected as a driver of sea-level variability.

3.5.2 Drivers of seasonal steric variability

To further examine the variability in steric height that is observed in Figure 3.5b, we evaluate the steric height per season (Figure 3.6a-d). The steric height is higher near the coast than offshore throughout the entire year. Furthermore, the steric height

shows a seasonal cycle, and is lowest during the winter (Figure 3.6a) and highest during the summer (Figure 3.6c). Decomposing the steric height into a halo- and thermosteric component using Eqs. 3.4 and 3.5 allows us to explore what drives the spatial and temporal variability in steric height.

The spatial variability in steric height is driven by the halosteric component (Figure 3.6e-h). The halosteric height is highest along the coast, which is caused by the freshwater of the river plume. The seasonal variability in the halosteric height along the coast is less than 1 cm. However, the width (i.e., the cross-shore distance from the coast) of the positive halosteric contribution varies. This is in line with what is expected from the wind-driven response of the river plume (Chapter 2). Winds induce Ekman transport, which is directed at an angle of 90 degrees to the right of the wind direction in the northern hemisphere. During the spring, the dominant wind direction is from the north-northeast. Consequently, the plume is forced offshore and the plume width increases. In contrast, the dominant wind direction during the autumn is from the south, causing the plume to narrow due to onshore-directed Ekman transport.

The seasonal cycle in steric height is induced by the thermosteric component (Figure 3.6i-l). The thermosteric height is spatially more uniform and does not show a

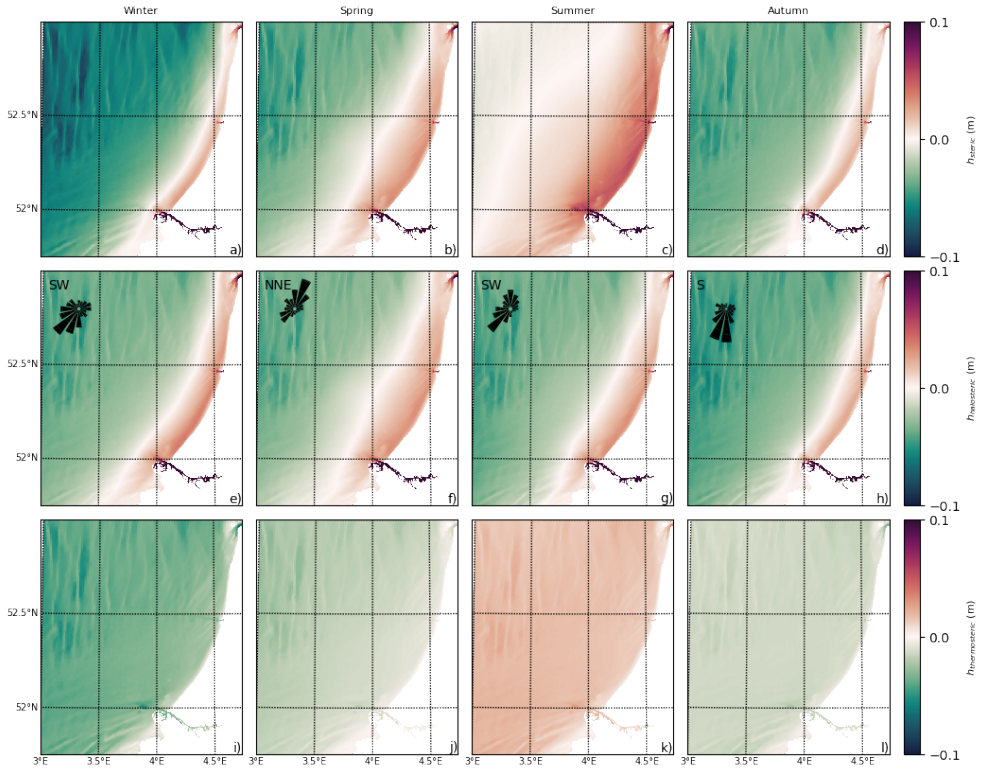

Figure 3.6: Steric h_{steric} (m) (a-d), halosteric $h_{\text{halosteric}}$ (e-h) and thermosteric height $h_{\text{thermosteric}}$ (i-l) per season. In the upper-left corner of panels e-h the wind rose is shown for each season.

specific signal related to the river plume. It is caused by the strong seasonal cycle in sea water temperatures with lowest temperatures in the winter and highest temperatures in the summer. So, the Rhine River plume induces an elevation in steric height and sea level along the coast, but induces little seasonal variability in steric height and sea level.

3.5.3 Temporal variability of the steric height at Hoek van Holland

Next, we evaluate the temporal variability of the steric height at Hoek van Holland during the year of 2019 (Figure 3.7). During the year, the river discharge varies (Figure 3.7a), which we expect to influence the steric height given the dependency on the freshwater thickness (see Figure 3.3). The steric signal shows strong tidal variability (blue line Figure 3.7b) and slower variations captured by the 10-day moving average (orange line Figure 3.7b). This slower varying signal correlates with the river discharge at Lobith, with a correlation coefficient of 0.67. The positive correlation indicates that the steric height is higher when the river discharge is larger. However, the fact that the minimum steric height (October) does not correspond to the lowest river discharge (Augustus-September) indicates the importance of estuarine processes: the mixing and mixing and transport of freshwater influences the steric height.

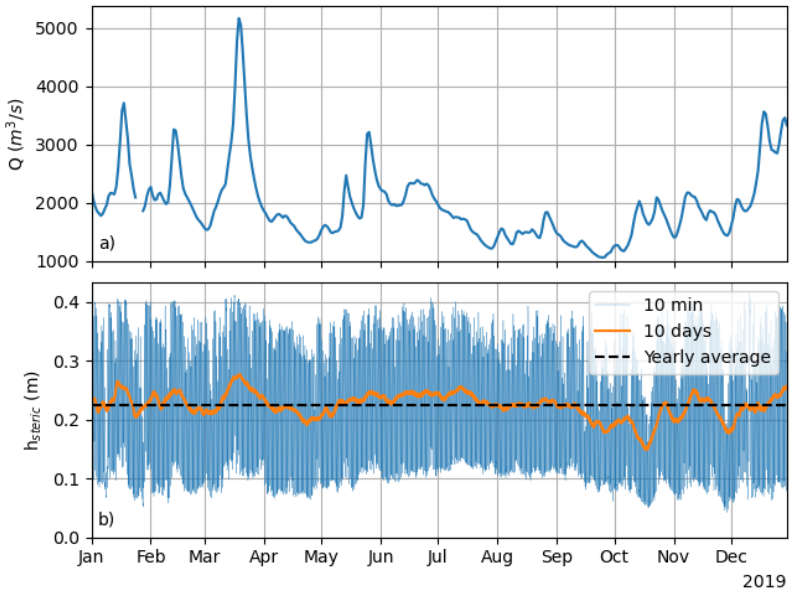

Figure 3.7: Time series of (a) the Rhine river discharge Q at Lobith and (b) the steric height h_{steric} at Hoek van Holland for the year 2019. In panel b, the blue line indicates the instantaneous values, the orange line the 10-day averaged values, and the dashed line the yearly averaged value.

The strong tidal variability in steric height at Hoek van Holland (orange line in Figure 3.8a) is caused by the tidally-pulsed outflow. At Hoek van Holland, the sea level exhibits a semidiurnal tidal signal (blue line in Figure 3.8a). Between high water

(HW) and low water (LW), there is an outflow and the salinity decreases (Figure 3.8b,c). At LW, the tidal currents turn, resulting in an inflow of saltier water into the estuary between LW and HW. At HW, the currents turn again. Consequently, the steric height exhibits a semidiurnal signal that is 180 degrees out of phase with the tidal signal. In line with the phasing of the outflow, the steric height reaches its maximum around LW, when the salinity is lowest, and reaches its minimum at HW, when the salinity is highest.

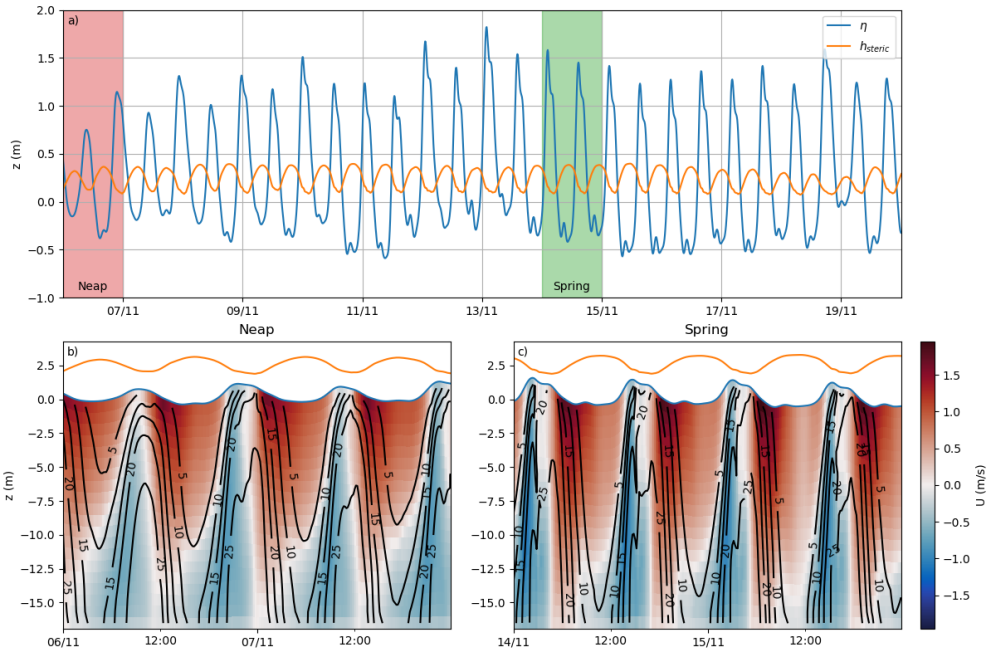

Figure 3.8: a) Time series of the sea level (blue) and steric height (orange) at Hoek van Holland during a spring-neap cycle. Note this is the same period for which the model is validated in Figure 3.2b. b,c) The tidally-pulsed river outflow during neap (b) and spring tide (c): colors indicate the along-channel velocity with red being outflow into the North Sea and blue inflow into the estuary, the black contour lines the salinity. The blue line shows the sea level and the orange line the normalized steric height.

3.6 Steric contribution to sea-level variability

Having identified the variability in steric height in the Rhine River plume, we assess in this section the steric contribution to sea-level variability. We compare results from the baroclinic and barotropic run, focusing on the locations Hoek van Holland and Scheveningen (locations (2) and (3) in Figure 3.1). First, we evaluate the difference in sea-level and tidal variance at these locations. Next, we evaluate per location whether the differences can be attributed to steric changes. This analysis provides a final link between the river plume and sea-level variability along the Dutch coast.

3.6.1 Sea-level variability: baroclinic vs barotropic run

To quantify the effect of the river plume on sea-level variability, we compare the sea-level variability between the baroclinic and barotropic runs, focusing on the locations Hoek van Holland, Scheveningen and Europlatform (see Figure 3.1). Table 3.2 shows the change in annual mean sea level, sea-level variance, tidal variance and M2 amplitude at all three locations.

At Hoek van Holland, located near the river mouth, the mean sea level for the baroclinic run is 15 cm higher than the barotropic run, and the variance is 15.8% smaller. Tidal analysis of both time series using the same set of constituents shows that the variance of the reconstructed tidal signal is smaller for the baroclinic run, indicating a smaller tidal range for the baroclinic run. The M2 amplitude equals 0.74 m and 0.81 m for the baroclinic and barotropic run, respectively.

At Scheveningen, located further downstream in the plume, the changes in sea-level variability between the baroclinic and barotropic run are much smaller than for Hoek van Holland. Here, the annual mean sea level is 4 cm higher for the baroclinic run, in line with Figure 3.5. In terms of variance, there is no difference between the baroclinic and barotropic run at Scheveningen.

Table 3.2: Change in annual mean sea level ΔMSL (m), sea-level variance $\Delta\sigma^2$ (m^2), tidal variance $\Delta\sigma^2_{tidal}$ (m^2) and M2 amplitude ΔA_{M2} (m) between the baroclinic and barotropic run at Hoek van Holland and Scheveningen. Between brackets the percent change is shown.

	Hoek van Holland	Scheveningen
ΔMSL	+0.149	+0.037
$\Delta\sigma^2$	-0.067 (-16%)	+0.002 (0%)
$\Delta\sigma^2_{tidal}$	-0.062 (-17%)	+0.002 (+1%)
ΔA_{M2}	-0.07 (-9%)	+0.00 (0%)

Since tides are known to interact with changes in mean sea level (Haigh et al., 2020), the river plume might also indirectly modulate the tides due to the elevated sea level along the coast (see Figure (3.5). However, the change in both tidal variance and M2 amplitude at Scheveningen (Table 3.2) shows that no change in tidal amplitude is found. We also observed very little change in tidal variance at Europlatform (Table 3.1). These results indicate that the Rhine River plume, or any other baroclinic processes, do not induce any larger-scale changes in tides along the Dutch coast.

3.6.2 Steric contribution at Hoek van Holland

To explain the difference in sea-level variability between the baroclinic and barotropic run, we focus on the steric contribution. First, we quantify the steric contribution to sea-level variability at Hoek van Holland. Following Piecuch and Wadehra (2020), we define the percent variance in sea level explained by the steric height V as

$$V = 1 - \frac{\sigma^2(\eta - h_{steric})}{\sigma^2(\eta)}\,, \tag{3.6}$$

where σ^2 is the variance (m^2). For the hindcast of 2019, it follows that $V = 0.76$, meaning that 24% of the sea-level variance is explained by variations in steric height at Hoek van Holland.

To further examine the steric contribution to sea-level variability, we compare the difference in sea level between the baroclinic and barotropic run with the steric height (Figure 3.9). The baroclinic (blue line) and barotropic sea level (orange line) are in phase and the HW levels are similar (Figure 3.9a). The largest difference is found at LW, with higher LW levels for the baroclinic run.

The difference in sea level between the baroclinic and barotropic run (orange line) closely follows the steric height (blue line) (Figure 3.9b), with a strong correlation observed ($r = 0.89$ for the entire year). The maximum steric height is reached at LW, when the salinity is lowest because of the tidally-pulsed outflow (Figure 3.8), elevating the level of LW. Consequently, the tidal range (i.e. the difference between HW and LW) is reduced by steric changes, which is in line with the lower M2 amplitude (Table 3.2). Therefore, the sea-level variance is smaller and the mean sea level is higher at Hoek van Holland for the baroclinic run.

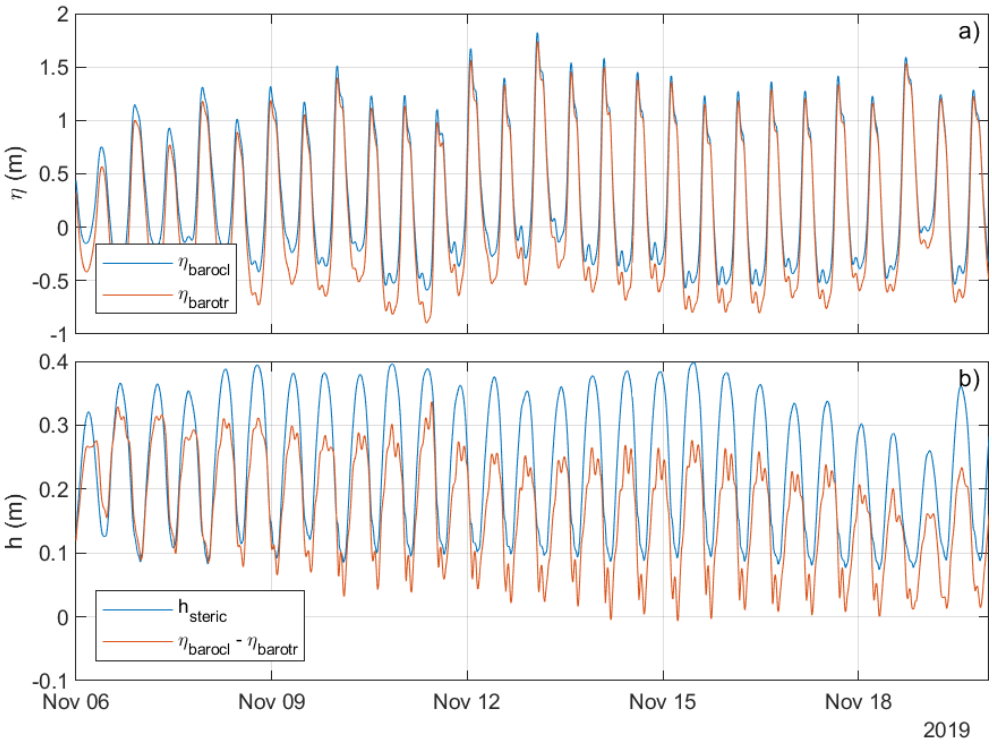

Figure 3.9: a) Sea level from the baroclinic (blue) and barotropic run (orange) for a two-week period with average discharge conditions. b) as panel a but for the steric height (blue) and the difference in sea level between both runs ($\eta_{\text{barocl.}} - \eta_{\text{barotr.}}$) (orange) at Hoek van Holland.

We have seen that the steric height shows strong tidal variability but also varies

more slowly during the year (Figure 3.7). To examine the steric contribution to sea-level variability on various timescales, we evaluate the power spectra of the steric height, sea levels and their differences (Figure 3.10). The power spectra of the baroclinic and barotropic sea level (Figure 3.10a,b) show very similar patterns, with most energy present at the semidiurnal frequencies. This is as expected as M2 and S2 are the major tidal constituents. Similarly, the power spectrum of the steric height shows large peaks for the semidiurnal frequencies (Figure 3.10c), which corresponds to observed tidal variability in steric height (see Figures 3.6 and 3.9).

The difference in power spectral density between the baroclinic and barotropic sea level spectra (Figure 3.10d) shows that the power spectral density is significantly lower for the baroclinic run at the semidiurnal frequency. This is in line with our previous observations in Figures 3.8 and 3.9, where we found that the LW levels are higher for the baroclinic run, reducing the tidal range (i.e. the M2 amplitude) and thus the power spectral density for the semidiurnal frequency. At other frequencies, we observe hardly any difference. This indicates that it is mainly the semidiurnal sea-level variability that is decreased the most by the baroclinic processes.

To confirm this finding, we evaluate in Figure 3.10e the difference in power spectral density between the power spectrum of the difference in sea level between the baroclinic and barotropic run (= time series indicated with blue line in Figure 3.9b) and the steric height. The difference at the semidiurnal frequency is on order of magnitude smaller than the difference in Figure 3.10d. This confirms that steric changes can largely explain the difference in semidiurnal sea-level variability between the baroclinic and barotropic run at Hoek van Holland.

3.6.3 Steric contribution at Scheveningen

We find no significant difference in sea-level variability at Scheveningen in (Table 3.2), so we do not expect a significant steric contribution here. To examine the difference in sea-level variability between Hoek van Holland and Scheveningen, we evaluate the power spectra of the steric height, sea levels and their differences for Scheveningen in the same way. (Figure 3.11). The power spectra of the baroclinic and barotropic sea level (Figure 3.10a,b) are almost equal. Similar to Hoek van Holland, most energy is present at the semidiurnal frequencies, which again is expected because of the semidiurnal tide. In contrast to Hoek van Holland, the energy in the power spectrum of the steric height is much less (Figure 3.10c). There is hardly any difference in power spectral density between the baroclinic and barotropic run (Figure 3.10d), nor an influence of the steric height (Figure 3.10e). This suggests that the observed effect on sea-level variability at Hoek van Holland is a local effect.

However, we find a pronounced signal of a tidal plume front, which is a characteristic feature of the river plume, in the sea level of a few centimeters (Figure 3.12). Tidal plume fronts are formed due to the tidally-pulsed river outflow in a tidal cross-flow (Hessner et al., 2001; Rijnsburger et al., 2021a). Freshwater accumulates in these fronts (Figure 3.12a), locally increasing the steric height (Figure 3.12b). These fronts propagate alongshore under the influence of tides and winds (Rijnsburger et al., 2021a, and Chapter 2). The fact that this has no significant effect on the sea-level variability at Scheveningen can be explained by the dynamics of a tidal plume front. First, the dynamics are highly non-linear because of their interaction with winds and tides

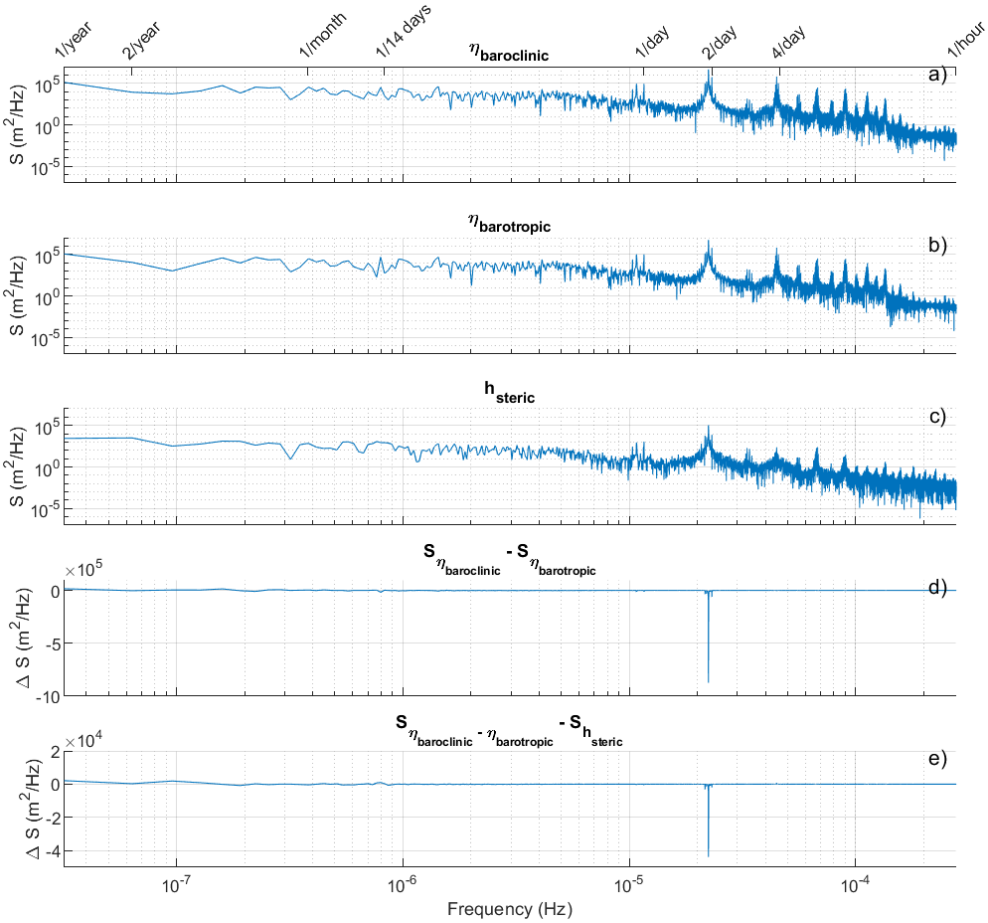

Figure 3.10: Power spectral density S at Hoek van Holland of a) the sea level from the baroclinic run, b) the sea level from the barotropic run, and c) the steric height. d) The difference in power spectral density ΔS between the power spectra of the baroclinic and barotropic sea level. e) The difference in power spectral density ΔS between the power spectra of the difference in sea level and the steric height.

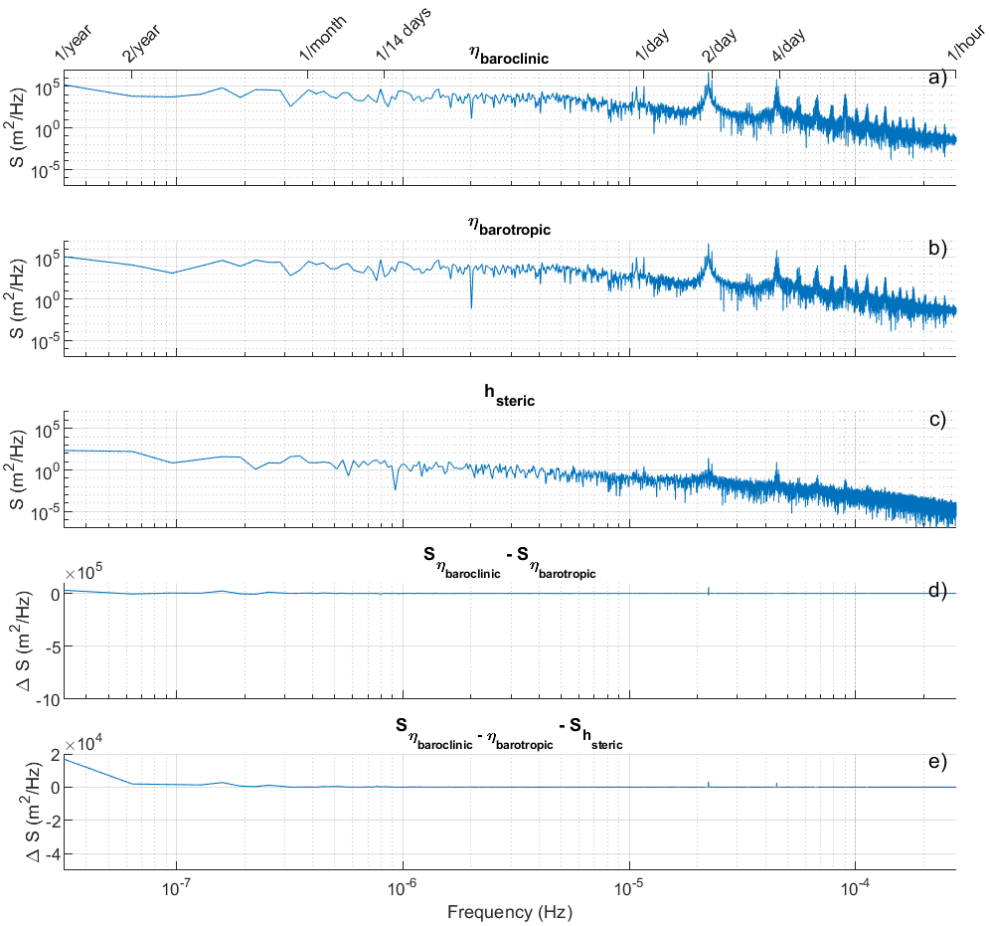

Figure 3.11: Power spectral density S at Scheveningen of a) the sea level from the baroclinic run, b) the sea level from the barotropic run, and c) the steric height. d) The difference in power spectral density ΔS between the power spectra of the baroclinic and barotropic sea level. e) The difference in power spectral density ΔS between the power spectra of the difference in sea level and the steric height. Note that the scale of the y-axis is fixed for the comparison with Figure 3.10.

(Rijnsburger et al., 2021a, and Chapter 2), and therefore their pathways are highly variable. In contrast to the river mouth, where the steric changes were coherent with the tidal signal, this is no longer the case. Second, tidal plume fronts undergo mixing while propagating, and therefore the induced steric contribution diminishes quickly away from the mouth. As a consequence, little change in sea-level variability is found at Scheveningen.

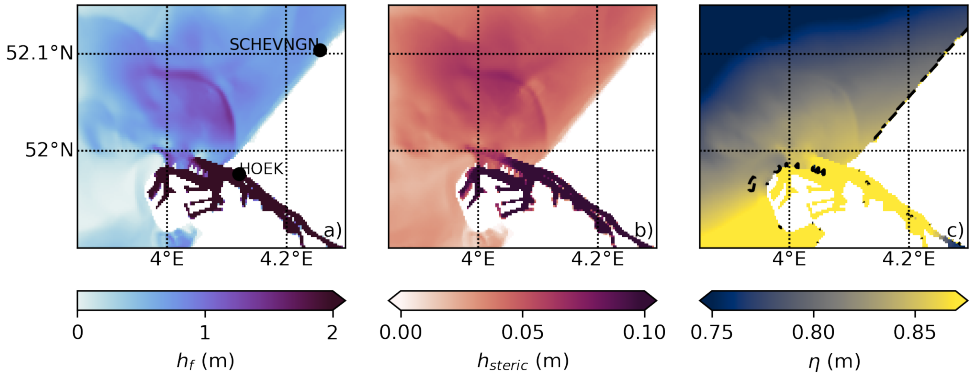

Figure 3.12: a) Freshwater thickness h_f (m), b) steric height h_{steric} (m), and c) sea level η (m) in the near-field plume at HW. Note that this a zoom of Figures 3.3 d,h and l with adjusted colour scales to visualize the (effect of the) tidal plume front.

3.7 Discussion

River runoff is recognized as a significant driver of sea-level variability on various spatial and temporal scales (Woodworth et al., 2019). This study builds on that understanding by exploring the contribution of the Rhine River plume to sea-level variability using a high-resolution model that is able to resolve the dominant dynamics of the river plume. Our findings demonstrate that the timescale and magnitude of runoff-induced sea-level variability strongly depends on plume dynamics, which vary on seasonal and tidal timescales. This study complements and extends, therefore, previous regional modelling studies on the oceanic response to river discharge (Piecuch et al., 2018; Giffard et al., 2019; Piecuch and Wadehra, 2020), who focused on seasonal and interannual variability.

Our results show that the Rhine River plume induce a positive steric anomaly along the Dutch coast, increasing the mean sea level along the Dutch coast. The steric height varies spatially and decays offshore and downstream due to the mixing of freshwater. On seasonal timescales, we find that the steric variability induced by the river plume depends on the wind-driven response of the plume rather than seasonal variations in river discharge, which is similar to what was found for the Amazon River (Giffard et al., 2019).

In the river mouth, the most significant contribution to sea-level variability is found. At Hoek van Holland, we identified variability in steric height on tidal timescales induced by the tidally-pulsed outflow, and on longer timescales captured by a

10-day moving average that correlate with variations in river discharge. Due to the phasing of tidal variations in steric height, the low water levels are higher. Consequently, the observed tidal amplitude and the sea-level variance are reduced. Tidally-pulsed river outflows are found in many river plumes worldwide (e.g., Columbia River (Orton and Jay, 2005; Nash et al., 2009), Merrimack River and Connecticut River (Spicer et al., 2021)), underscoring the potential importance of this mechanism as driver of sea-level variability.

While the sea-level variability induced by the river plume is significant, it only explains a part of the total sea-level variability. This is fully expected, as tides and surges are known to be the dominant drivers of sea-level variability in the North Sea (Huthnance, 1991). Nonetheless, the (non-linear) interaction between steric changes and the dominant drivers of sea-level variability is crucial to unravel in order to analyse patterns and trends in sea level and its forcing mechanisms, which becomes increasingly important in the face of climate change and changing (extreme) water levels (Woodworth et al., 2019). For example, the river plume affects the mean sea level. Although no significant large-scale tidal changes were observed in this case, mean sea-level changes affect the phase and amplitude of short- and long-term tidal constituents, such as M2 and Sa (Haigh et al., 2020).

3.7.1 Implications for monitoring and modelling

A key contribution of this study is the improved agreement between altimeter- and model-derived sea levels when the river plume is included in the model simulation, confirming the importance of river plumes as a driver of sea-level variability and the ability of our model to capture this. This highlights the necessity of accurately representing estuaries and river plumes in models used for coastal sea-level studies.

Satellite SAR altimetry can capture the spatial variability in coastal sea level (e.g. Dinardo et al., 2018), albeit on lower temporal resolution than tide gauge stations. However, there has been a mismatch between satellite altimetry data and tide gauge data for coastal sea levels (Vinogradov and Ponte, 2011). Despite recent advances, it remains a challenge to obtain accurate water levels within 10 km distance from the coast (Vignudelli et al., 2019). Our findings supports the suggestion by Vinogradov and Ponte (2011) that river runoff is among the reasons for the observed differences between water levels obtained using conventional low-resolution mode altimetry and tide gauges. For those interested in using altimeter-derived coastal water levels to study a particular component of the water level (e.g., tides or surges), it is important to be aware that there is a signal of the river plume in the water levels that needs to be corrected for as well.

Furthermore, our results show how steric changes could modulate the tidal signal at a tide gauge, thereby potentially affecting the amplitudes and phases of tidal constituents. Similarly, the local wind-driven response of the sea level can be influenced by the wind-driven response of a river plume (Chapter 2). This raises the question which processes drive the observed sea-level variability at a tide gauge. The answer to this question has implications for how the tide gauge data should be interpreted (e.g., for tidal analysis or low-frequency sea-level variability studies) and used for the calibration of models that are used for (extreme) water level forecasts and sea-level projections. For example, it can be questioned whether tide gauge data collected near

a river mouth can be directly used to calibrate a barotropic model due to the potential steric changes which are not captured by a barotropic model.

To measure the steric height, only a small adjustment of the setup of tide gauge stations would suffice.

$$h_{\text{steric}} = -\frac{1}{\rho_0} \int_{-h_{\text{sensor}}}^{\eta} \left[\frac{P}{(\eta - h_{\text{sensor}})\, g} - \rho_0 \right] dz \,. \tag{3.7}$$

By adding a pressure sensor on a fixed height h_{sensor} (m) (preferably on the bottom such that the entire water column is taken into account), the pressure P (Nm^{-2}) can be related to the density ρ (kgm^{-3}) and subsequently to the (change in) steric height h_{steric} (m) (Eq. 3.7). This would not only improve our understanding of steric changes, but could also be used for model validation and the correction of sea-level records used for the analysis of tidal constituents and long-term trends, for example.

3.7.2 Impact of changing river flows on future sea levels

Global climate change causes not only sea-level changes (Intergovernmental Panel on Climate Change, 2023b), but also affects river flows (Gudmundsson et al., 2021). Changing river discharges will change the structure of river plumes (Horner-Devine et al., 2015), causing a change in steric height. Current models used for sea-level projections, which typically have a horizontal resolution in the order of 25–100 km (Hermans et al., 2022), are too coarse to resolve river plume dynamics and the resulting impact on sea levels. To be able to account for these effects, such models require a sufficiently high spatial resolution combined with accurate discharge projections. This is especially relevant for extreme water levels, as we have shown that steric changes interact with tides and winds. To a lesser extent, changing river flows will affect low-frequency sea-level variability and long-term tidal constituents. This is important since river discharges are changing due to the intensification of the hydrological cycle (Rottler et al., 2020; Gloor et al., 2013).

In conclusion, our findings show that the Rhine River plume influences sea-level variability due to the induced changes in steric height. Its contribution is highly variable in space and time, modulated by the interaction with tides and winds. This study provides a comprehensive assessment of how river plumes, even from relatively moderate rivers like the Rhine River, can affect sea-level variability. Therefore, river plumes, which are often omitted or not resolved in current sea-level studies, should be factored into future studies on sea-level.

Part II
Sound speed inversion

CHAPTER 4

Principles of multibeam echosounders

In the second part of this thesis, we aim to develop a method to invert sound speed profiles from the measurements of a multibeam echosounder (MBES) — an acoustic instrument used for seafloor mapping. To be able to invert sound speed profiles from MBES measurements, we must understand the principles of the MBES and underwater acoustics. First, we briefly introduce the MBES. Next, we discuss the propagation of sound in the ocean in order to understand how sound propagates through the water column to and from the MBES. Then, we explain the working principles of bathymetric MBES measurements, including how to account for variations in the sound speed. Lastly, we provide an overview of other studies exploiting MBES measurements using inversion methods. The provided knowledge in this chapter helps understanding Chapter 5.

4.1 Introduction to multibeam echosounders

A multibeam echosounder (MBES) is an acoustic instrument that is used for hydrographic surveys. An MBES is usually mounted under the hull of a vessel and consists of a transmitter and a receiving module (multiple hydrophones). A sound signal, called a ping, is emitted with a certain frequency. This frequency typically varies between 12–500 kHz (Lurton, 2002). Higher frequency signals provide smaller beam widths, while lower frequency signals attenuate slower and propagate deeper into the ocean. The seabed scatters the acoustic signal back to the receiver. At reception, the two-way travel time and the intensity of the returned signal are measured by the MBES. By applying delays or phase shifts to the signals received by the different hydrophones the information is obtained as a function of the beam angle over a swath perpendicular to the sailing direction. This is called beamforming. This information can be used to derive the water depth and/or seafloor properties (Lurton, 2002). From a pair of two-way travel time and beam angle in combination with a sound speed profile (SSP), the water depth is calculated using ray tracing (i.e. reconstructing the acoustic path) (Lurton, 2002; Mohammadloo et al., 2019). The backscatter, which is the intensity of the returned signal, depends on the type of sediment and roughness of the seabed, and can therefore be used for seabed classification (Simons and Snellen, 2009; Gaida et al., 2018). Modern MBES systems can also provide water column data, which is the backscatter over the water column. This allows to create 3D images of the wa-

ter column, used for the identification of fish, detection of seeps and oceanographic measurements of suspended sediment, mixing and internal waves (Colbo et al., 2014).

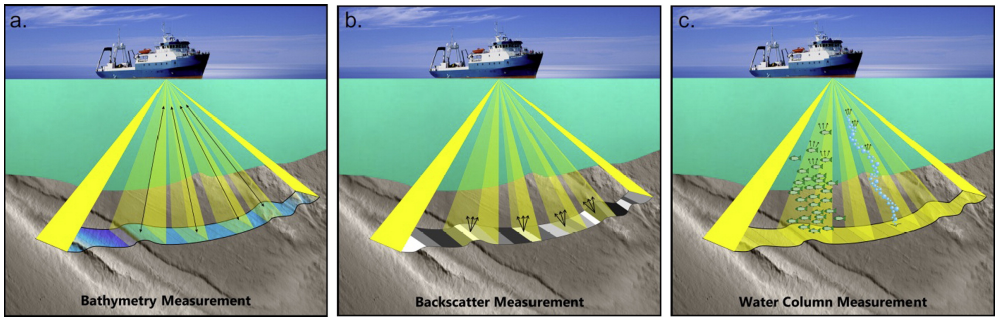

Figure 4.1: Illustration of the different types of MBES measurements: a) bathymetric measurement; b) backscatter measurement; c) water column measurement (Colbo et al., 2014).

4.2 Propagation of sound

To understand the working principles of the MBES, it is important to understand how sound propagates through the water column to and from the MBES. In this section, we explain the fundamentals of underwater acoustics that are required for understanding the working principles of the MBES.

4.2.1 Acoustic waves

From a physical point of view, sound can be seen as a vibration or a pressure wave propagating through a medium such as water or air. The acoustic wave consists of periods of compression, with increased pressure, and rarefaction, with decreased pressure. These waves can be characterized using properties such as the frequency (or its inverse, the wave period) and amplitude (the intensity). The propagation of acoustic waves is described by the linear wave equation:

$$\Delta p = \frac{\partial^2 p}{\partial x^2} + \frac{\partial^2 p}{\partial y^2} + \frac{\partial^2 p}{\partial z^2} = \frac{1}{c^2}\frac{\partial^2 p}{\partial t^2}\,. \tag{4.1}$$

Here, Δ is the Laplace operator, describing the divergence of the gradient in space (x,y,z), p the acoustic pressure (Nm^{-2}), t the time (s) and c the propagation speed (ms^{-2}). The propagation speed is given by

$$c = \sqrt{\frac{B}{\rho}}\,, \tag{4.2}$$

where B is the bulk modulus of the medium (Nm^{-2}) and ρ its density (kgm^{-3}). During propagation, the waves can be refracted, reflected and attenuated, changing the intensity and direction of the acoustic wave.

4.2.2 Sound speed in the ocean

The propagation speed of sound in the ocean is approximately 1500 ms^{-1}, but varies with the water temperature, salinity and depth. Medwin (1975) proposed the following empirical equation for the sound speed:

$$c = 1449.2 + 4.6T - 0.055T^2 + 0.000029T^3 - (1.34 - 0.01T)(S - 35) + 0.017z\,, \quad (4.3)$$

where c is the sound speed (ms^{-1}), T the water temperature (°C) and S the salinity (PSU). The domain of applicability is $0 < T < 35$ °C, $0 < S < 45$ PSU and $0 < z < 1000$ m.

The sound speed variations during the course of a survey depend on the location. In the deep, open ocean, ocean properties, and thus the sound speed profile, are usually relatively stable in time and space. Generally, the water temperature decreases towards the poles. The salinity also varies in the ocean, with the saltiest waters found near the equator due to strong evaporation and fresher water near the poles due to melt water. Seasonal changes due to surface heating will not affect the sound speed profile during the course of a survey.

In shallow coastal and shelf seas, however, water temperature and salinity, and thereby the sound speed, can vary significantly in time and space (horizontally and vertically) due to strong (tidal) currents, surface heating/cooling and the influence of river runoff. The sound speed varies not only horizontally, but also with depth due to stratification. In the Rhine River plume, for example, the interaction between freshwater, tides and winds is highly dynamic. Tidal straining induces a semidiurnal cycle in the stratification (de Boer et al., 2008; Rijnsburger et al., 2016), tidal plume fronts propagate along the coast (Rijnsburger et al., 2021a) and they even can be accompanied by internal waves (Rijnsburger et al., 2021b). Therefore, significant variations in sound speed can occur during the course of the survey.

4.2.3 Snell's Law

When the sound speed changes, the direction of the acoustic wave changes. This is called refraction, and can be described using Snell's Law:

$$\frac{\cos\theta}{c} = \text{constant}\,, \quad (4.4)$$

where θ is the direction of the acoustic wave. Snell's law is applied in ray tracing to reconstruct the path of the acoustic signal to and from the MBES.

4.2.4 Interaction with the seabed

When the acoustic wave reaches the seabed, it interacts with the seabed and is attenuated (Figure 4.2). In the case of a perfectly flat bottom, part of the signal is reflected (reflection) and the other part of the signal enters the seabed (transmission). In case of reflection, the angle of the reflected signal equals the angle of the incident wave ($\theta_r = \theta_i$). In case of transmission, θ_t depends on the change in sound speed (Snell's Law - Eq. 4.4). The ratio between reflection into the water column R and transmission into the seabed T depends on the incident angle θ_i and the properties of these media (c_0, c_1, ρ_0, ρ_1):

$$R(\theta_i) = \frac{\rho_1 c_1 \sin\theta_i - \rho_0 c_0 \sin\theta_t}{\rho_1 c_1 \sin\theta_i + \rho_0 c_0 \sin\theta_t} . \tag{4.5}$$

$$T(\theta_i) = \frac{2\rho_1 c_1 \sin\theta_i}{\rho_1 c_1 \sin\theta_i + \rho_0 c_0 \sin\theta_t} . \tag{4.6}$$

Refraction and transmission are linked through:

$$T(\theta_i) = R(\theta_i) + 1 . \tag{4.7}$$

This implies that the pressure of the transmitted wave can exceed that of the incident wave. However, energy conservation is maintained because the sum of the reflected and transmitted intensities equals the intensity of the incident wave (Lurton, 2002).

In reality, however, the seabed is far from perfectly flat. Because of small irregularities in the bottom, the acoustic wave scatters in all directions, including in the direction back towards the MBES. This is called backscattering (Figure 4.2). The amount of scattering depends on the incident angle, the frequency of the signal and geophysical bottom parameters such as the roughness. It is most significant when the acoustic wavelength ($\lambda = c/f$) is of the same order of magnitude as the bottom roughness or smaller. An MBES exploits this acoustic phenomenon by measuring the two-way travel time and strength of the backscattered signal using a bottom detection algorithm.

4.3 Bathymetric measurements

To understand how MBES measurements can be exploited for the inversion of sound speed profiles, it is important to understand the working principles of bathymetric measurements. An MBES measures the two-way travel time of the pings along a swath (Figure 4.3), which is used to determine the water depth. When the sound speed profile is known, the path of the ray can be reconstructed per beam angle based on the two-way travel time. Combined with the position and orientation of the system,

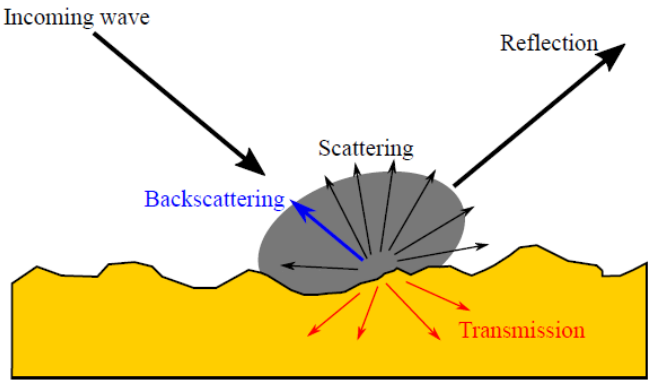

Figure 4.2: Interactions between incoming acoustic wave and seabed: reflection, transmission and (back)scattering (Mohammadloo, 2020).

the across-track distance and the water depth can be calculated for each beam using a ray-tracing algorithm. In this section, we explain the working principles by illustrating what happens when a constant sound speed (or a erroneous sound speed profile) is used when calculating the water depth, showing how sound speed variations should be taken into account using a ray-tracing algorithm and describing the resolution (in time and space) of bathymetric MBES measurements.

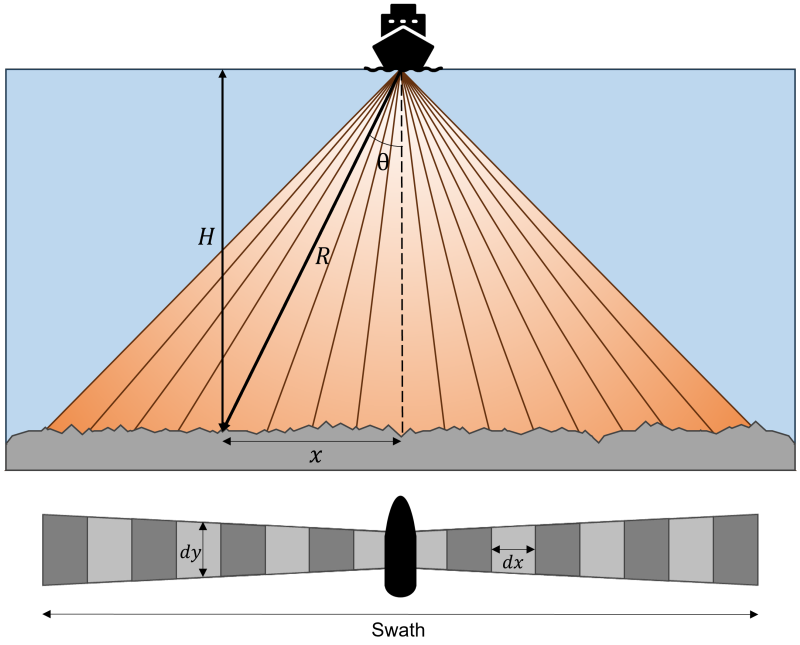

Figure 4.3: Geometry of multibeam echosounder: front view with beams and bathymetric measurement for beam angle θ (upper) and top view with the swath, across-track resolution δx and along-track resolution δy (lower) (after Mohammadloo, 2020; Lurton, 2002).

4.3.1 Using a constant sound speed

When assuming a constant sound speed, the acoustic path of the ray is straight and the length of the ray R equals

$$R = \frac{ct}{2}\,, \tag{4.8}$$

where t is the two-way travel time (s) and c the sound speed (ms^1). Following from basic trigonometry, the water depth H (m) and across-track distance x (m) relative to the MBES position are

$$H = R\sin\theta\,, \tag{4.9}$$

$$x = R\cos\theta\,. \tag{4.10}$$

Since the water depth and across-track distance are calculated relative to the MBES system, it is critical to know the exact position of the MBES system in order to accurately determine the 3D geographical position of the seabed. Failing to correct for movements such as pitch, heave, yaw and roll results in wrongly estimated positions of the bathymetry (Lurton, 2002).

However, the sound speed varies with depth due to variations in salinity and/or temperature. According to (Snell's law — Eq. 4.4), this will impact the ray's path and, therefore, the calculated depth and across-track position. Not properly accounting for those changes results in a deformation of the estimated bathymetry. These effects are commonly known as smileys (concave distortion) and frownys (convex distortion). Figure 4.4 illustrates using a synthetic example how the estimated bathymetry is distorted when a constant sound speed is assumed instead of using the actual SSP. Because the depth-averaged sound speed is equal for both profiles, no bias occurs. Errors in the estimated location of the seabed (x,z) are increasing towards the outer beams, since refraction is not accounted for.

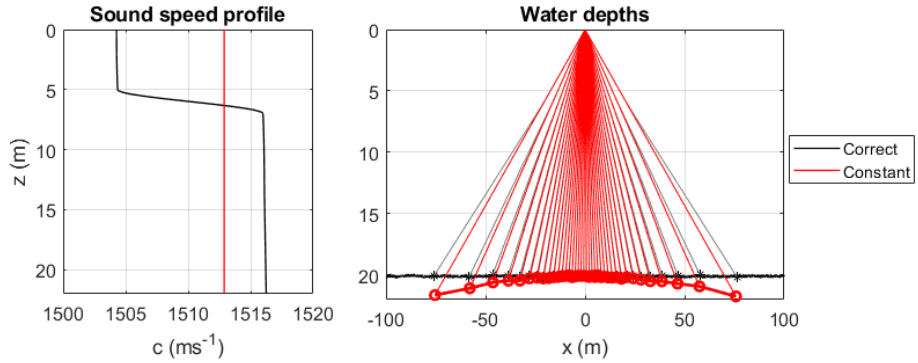

Figure 4.4: A convex distortion of the bathymetry (a frowny) due to the use of an erroneous SSP in a bathymetric MBES measurement. The black stars indicate the correctly measured bathymetry using the correct SSP shown in the left panel. The red circles indicate the distorted bathymetry obtained using a constant SSP.

Moreover, when beamsteering is applied at reception, using an incorrect sound speed introduces an error in the applied time delays (Mohammadloo et al., 2019). Consequently, the actual beam angle differs from the steering angle, again resulting in a deformation of the estimated bathymetry.

For accurate bathymetric measurements, the sound speed needs therefore to be known for the entire water column. To measure the SSP, one can measure the sound speed directly using a sound velocity profiler or by lowering a CTD to measure the salinity and temperature over depth, which in turn are used to determine the corresponding sound speed (using Eq. 4.3, for example). In theory, an accurately estimated bathymetry can also be obtained using an incorrect sound speed profile (Geng and Zielinski, 1999). This is the case when the surface sound speed and the depth-integrated sound speed are equal to that of the correct sound speed profile. When a sound speed profile fulfills these conditions, it is called an equivalent sound speed profile.

4.3.2 Ray tracing

To account for sound speed variations in the water column when reconstructing the acoustic path of the ray, a ray-tracing algorithm needs to be used, which generally consists of the steps described below. Per layer, the change in sound speed is determined and subsequently the change in beam angle and the resulting path of the acoustic ray (Figure 4.5).

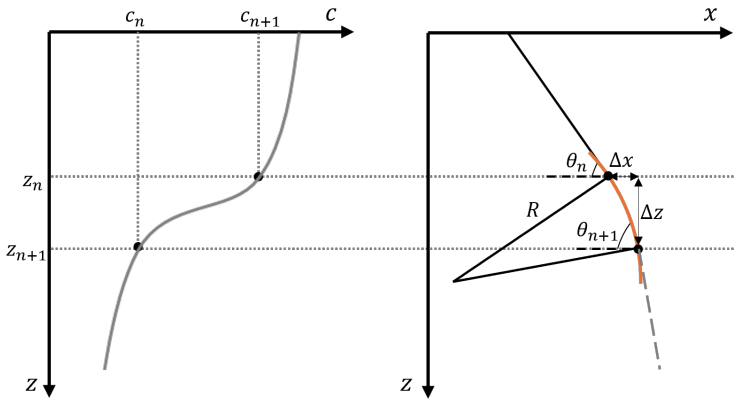

Figure 4.5: Schematization of the ray tracing algorithm (after Li et al., 2018a): left) sound speed profile and sound speeds for layer n, right) refraction of ray in layer n, assuming a constant sound speed gradient.

The water column is divided into n layers and a linear sound speed gradient is assumed over the depth of each layer. Note that horizontal sound speed gradients are ignored, and only vertical sound speed gradients are taken into account.

1. Using these assumptions, the vertical sound speed gradient between two layers g equals

$$g = \frac{c_{n+1} - c_n}{z_{n+1} - z_n}. \tag{4.11}$$

2. Using Snell's law (see Eq. 4.4), the change in beam angle within layer n is determined:

$$\theta_{n+1} = \arccos\left(\cos\theta_n \frac{c_{n+1}}{c_n}\right). \tag{4.12}$$

3. The radius of curvature of the ray R equals

$$R = -\frac{c_n}{g\cos\theta_n}. \tag{4.13}$$

When $R < 0$, so when the sound speed gradient is negative, the ray is refracted downwards (as is the case in Figure 4.5). When $R > 0$, so when the sound speed gradient is positive, the ray is refracted upwards.

4. The new position follows from

$$\Delta x = R(\sin\theta_{n+1} - \sin\theta_n)\,, \tag{4.14}$$
$$\Delta z = R(\cos\theta_n - \cos\theta_{n+1})\,. \tag{4.15}$$

5. The travel time is

$$t_{n+1} = t_n + \frac{1}{g}\left(\log\frac{\tan\frac{\pi}{2} - \theta_{n+1}}{2} - \log\frac{\tan\frac{\pi}{2} - \theta_n}{2}\right)\,. \tag{4.16}$$

6. Steps 1–5 are repeated until $t_n \geq \frac{T}{2}$.

Using this algorithm, the water depth can be accurately determined based on a pair of beam angles and two-way travel times when the sound speed profile is known.

4.3.3 Resolution

The spatial resolution of bathymetric MBES measurements primarily depends on the beam angle and water depth. MBES often offer two different configurations for the beam angles: equiangular or equidistant. For equiangular systems, the beam width is constant over the entire swath, but the across-track resolution worsens towards the outer beams. For equidistant systems, the beam width varies such that the across-track resolution is constant over the swath.

The across-track resolution of the bathymetric MBES measurements δx (Figure 4.3) is given by

$$\delta x = \frac{H\theta_T}{\cos^2\theta} \tag{4.17}$$

where H is the water depth (m), θ the beam angle (rad) and θ_T the beam width (rad).

In the along-track direction, the resolution δy is determined by the beam opening angle θ_L and is given by

$$\delta y = \theta_L R\,, \tag{4.18}$$

where R the ray length (m) (Lurton, 2002). δx and δy increase towards the outer beams due to the increased ray length (Figure 4.3). In practice, the actual along- and across-track resolution are coarser, as bathymetric measurements are often gridded.

The along-track coverage is determined by the ping rate and vessel speed. The most effective ping rate involves transmitting the next ping immediately after receiving the echo of the preceding ping, with a delay corresponding to the propagation time of the outermost beam.

$$T_R > \frac{2H}{c\cos\theta_{max}} + T + \delta T\,, \tag{4.19}$$

where T_R is the repetition period (s), θ_{max} the beam angle of the most outer beam and δT the lengthening of the signal (s) (Lurton, 2002). To achieve 100% spatial coverage, the vessel speed should be limited such that the distance by the vessel between two successive pings is less than the along-track resolution. The resulting maximum vessel speed V_{max} is given by

$$V_{max} \leq \frac{c}{2}\theta_L\cos\theta_{max}\,. \tag{4.20}$$

The range resolution δz is given by

$$\delta z = \frac{cT}{2}\,, \tag{4.21}$$

where c is the sound speed (ms^{-1}) and T the pulse duration (s).

4.4 Sound speed inversion

A representative SSP is crucial for accurate bathymetric MBES measurements, but collecting SSPs is very time-consuming and costly. Hence, inversion methods are being developed to estimate the SSPs and/or improve the accuracy of bathymetric measurements. Snellen and Simons (2008) applied Matched Field Inversion (MFI) to successfully estimate the SSP, amongst other geo-acoustical parameters. MFI is a processing technique that compares the acoustic field measured by an array of hydrophones with a modelled acoustic field. By adjusting the model parameters, the difference between the measured and modelled signal is minimized, finding the set of environmental parameters that best match the observed data. By describing the vertical profile as function of a limited number of basic functions (EOFs), the SSP could be reconstructed based on a limited number of unknowns.

It is common practice to carry out MBES surveys with a small overlap between adjacent swaths to avoid the relatively large errors at the outer beams, for example resulting from the use of erroneous SSPs. When processing the measurements, a mismatch in bathymetry between overlapping swaths is found. Mohammadloo et al. (2019) exploited the overlap between swaths to correct bathymetric measurements. They optimize the estimated sound speed by minimizing the difference in depth between the different swaths. Consequently, the mismatch between overlapping swaths is reduced, resulting in an improved accuracy of the measured bathymetry.

In the next chapter, we aim to exploit the overlap between adjacent swaths to estimate the SSP. Changes in sound speed are an indicator for variations in ocean properties (salinity, temperature). MBES measurements can therefore be an important source of data in the field of oceanography.

CHAPTER 5

Inversion of sound speed profiles from multibeam echosounder measurements using Differential Evolution

ABSTRACT

The sound speed provides insight in ocean properties, as it depends on depth, temperature and salinity. Here, we propose a method to invert sound speed profiles (SSPs) from multibeam echosounder (MBES) measurements, providing a SSP for every ping. Using erroneous SSPs results in a mismatch in the estimated bathymetry between overlapping swaths. The SSP is estimated by minimizing this mismatch using Differential Evolution. In this work, SSPs are described using empirical orthogonal functions (EOFs), which are obtained from historical SSPs. As a proof-of-concept, we apply the inversion on a simulated MBES survey, where the synthetically generated SSPs are fully described by 3 EOFs. The inverted SSPs deviate 1 m/s from the correct profiles. In the case of actual SSPs, more EOFs are possibly required. The number of required EOFs to get an accurate estimate of the SSP is assessed by using SSPs acquired in the North Sea. Results show that including only 2 EOFs is sufficient to accurately estimate the SSP, although larger deviations up to 3 m/s were found. In this paper, we demonstrated the potential of the proposed method to invert SSPs from MBES measurements, which can provide information about the vertical structure of the water column.

5.1 Introduction

Estuaries and river plumes are highly dynamic areas. Due to the input of fresh river water, strong salinity and/or temperature gradients arise both vertically and horizontally. The resulting density differences induce complex currents, which affect, among others, salt intrusion and sediment transport (de Nijs et al., 2011).

Measuring these phenomena is a challenge. To capture the strong variability in both time and space, very extensive measurement campaigns are required. The deployment of moorings would cover the temporal variability at fixed locations, but not capture the spatial variability. In contrast, vessels are able to cover a larger spatial domain, but many surveys would be required to increase the temporal coverage.

To ensure nautical safety, bathymetric surveys are conducted regularly. This is often done using multibeam echosounders (MBES). A ping is transmitted in a wide swath perpendicular to the sailing direction. Beamforming at reception allows to estimate depths from the two-way travel time and beam angle, in combination with a sound speed profile (SSP). This SSP is measured independently by lowering a sound velocity profiler or a Conductivity-Temperature-Depth (CTD) sensor. Since these measurements are time-consuming, typically only a few are taken per survey.

In case an erroneous SSP is used, the bathymetry estimated from the two-way travel times will be deformed. These deformations are typically known as a smileys or frownies because of the convex shape of the estimated bathymetry along a swath. The deviation is largest for the outer beams. To minimize this error in the estimated bathymetry and to meet the IHO standards for hydrographic operations, it is common practice that the swaths overlap by sailing adjacent tracks sufficiently close to each other. Since the time between measuring two overlapping swaths is generally much smaller than the typical timescale of bed level changes, the bottom can be assumed stable. In case a mismatch is observed between the water depth estimates of the overlapping swaths, it can thus be associated to the use of erroneous SSPs. Mohammadloo et al. (2019) utilized this redundancy to correct the bathymetric measurements by minimizing the mismatch in water depth estimates between overlapping swaths. They parametrized the SSP using a mean sound speed and a constant gradient.

In this study, we propose a method to invert the SSP from MBES measurements, following a similar approach as Mohammadloo et al. (2019) used to estimate the bathymetry. In contrast, we parametrize the SSP using a series of basis functions, i.e. empirical orthogonal functions (EOFs), such that it can be described by a limited number of variables. The EOFs can be derived for specific areas if a sufficient number of historically collected SSPs is available. Typically, only a few EOFs are needed to accurately describe the profiles for that specific area and season, assuming that the historical data are still appropriate. Our method allows to estimate the SSP for each ping, providing large sets of SSPs. This gives insight in the temporal and spatial variability of the sound speed in the area of interest. Since the sound speed is governed by depth, temperature and salinity, changes in the sound speed reflect variations in the salinity and/or temperature. Exploiting MBES measurements by inverting the SSP can thus provide additional oceanographic data.

In Section 5.2 we give a detailed explanation of the proposed method. Subsequently, we invert the SSPs from a simulated MBES survey, where synthetic SSPs are used that are fully described by 3 EOFs. This proof-of-concept is presented in Section

5.3. In Section 5.4, we investigate the required number of EOFs to get an accurate estimate of the SSP. To this end, the synthetic SSPs in the simulated MBES survey are replaced by historically measured SSPs. The conclusions are presented in Section 5.5.

5.2 Method

In this section, we elaborate on the proposed method to invert SSPs from MBES measurements in more detail. The inversion is based on the fact that using an erroneous SSP results in a convex-shaped estimate of the bathymetry when processing MBES measurements. In Figure 5.1, we illustrate how this results in a mismatch in the estimated bathymetry between two overlapping swaths by adopting erroneous SSPs and subsequently determining the bathymetry using a ray tracing algorithm. The bottom is assumed to be stable. We quantify this mismatch using a so-called energy function (Section 5.2.1). The SSPs are estimated by minimizing this energy function using Differential Evolution (DE) (Section 5.2.2). To limit the number of unknowns, the SSPs are described using EOFs (Section 5.2.3). The inversion gives an SSP for each ping along each track, providing large datasets.

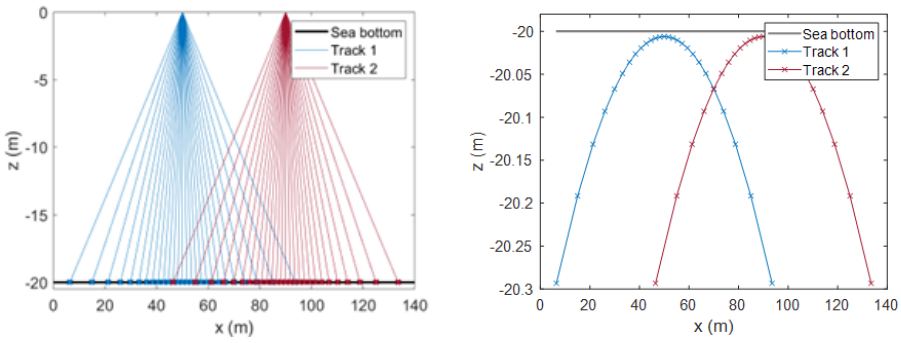

Figure 5.1: a) Two overlapping MBES swaths. b) The deformation of the estimated bathymetry for the two swaths due to the use of erroneous SSPs, resulting in a mismatch in the estimated bathymetry between the overlapping swaths (between $x = 45$ m and $x = 95$ m).

5.2.1 Energy function

The fitness of a SSP is evaluated using the energy function, which quantifies the mismatch in estimated bathymetry between overlapping swaths. The energy function E is defined as

$$E = \sum_j \sqrt{\frac{\sum_k (\hat{z}_{j,k} - z_{j,k})^2}{K}}, \tag{5.1}$$

where $z_{j,k}$ is the real depth, $\hat{z}_{j,k}$ the estimated depth per beam k of track j, and K is the total number of beams. $z_{j,k}$ is obtained using a ray tracing algorithm and depends on the SSP. Of course, the real depth is not known in practice. Therefore, $z_{j,k}$ is obtained

by combining and interpolating the depth estimates of the different swaths. The more accurate the SSPs are, the smaller the mismatch between overlapping swaths will be, and the lower E will be.

This energy function is a modified version of the one used by Mohammadloo et al. (2019). Since the depth estimates are no longer gridded and averaged, it is expected to improve the estimate of the SSP, especially in case of irregular bathymetry. The energy function is computed per segment. A segment consists of one ping per track. It is required that all tracks are parallel and sufficiently close to each other, such that the swaths of the different pings in each segment are aligned and overlap. This definition is, therefore, less versatile applicable than the one that is used by Mohammadloo et al. (2019), since vessels are subject to pitch and yaw.

5.2.2 Differential Evolution

The search for the best SSP is an optimization problem; the energy function is minimized. Here, we use the global optimization method Differential Evolution (DE) developed by Storn and Price (1997), and has been applied successfully to other inversion problems before (Mohammadloo et al., 2019; Snellen and Simons, 2008). DE is a subset of the well-known genetic algorithms. It searches for the global optimum, i.e. the SSP for which the energy function is minimal, by improving the solution iteratively based on an evolutionary process. The first generation is defined randomly, respecting the search bounds for the unknown parameters. A generation, i.e. an iteration, consists of a number of candidate solutions, depending on the population size. A candidate solution consists of a SSP per track. For every candidate solution, the bathymetry is determined using a ray tracing algorithm and next the energy function is evaluated. Subsequent generations are defined based on a process of mutation, crossover, and selection. Different variants of DE exists, which apply different mutation schemes (Das and Suganthan, 2011).

Here, we use the classical *DE/rand/1/bin* scheme (Storn and Price, 1997). In this scheme, each population member is evolved by generating a new candidate through mutation and crossover. Specifically, *rand* indicates that the base population member is randomly selected from the current population. *1* indicates that the population member is mutated by adding the weighted difference between two randomly chosen members. The process of crossover determines which mutations are passed down to the next generation. *bin* indicates that the crossover probability is binomially distributed. An candidate enters the next generation if it outperforms its predecessor. The algorithm is terminated when a preset maximum number of generations is exceeded. For further details on the application of the DE algorithm on inversion problems, we refer to the work of Snellen and Simons (2008).

The performance of DE, i.e. the probability to locate the global optimum, is highly determined by the so-called setting parameters:

- Mutation scheme
- Multiplication factor
- Crossover rate
- Population size
- Maximum number of generations

The DE setting parameters as used in this study can be found in Table 5.1. The values for the multiplication factor and crossover probability were set as used by Mohammadloo et al. (2019) and Snellen and Simons (2008). The population size and maximum number of generations were set to 32 and 300 respectively, to avoid preliminary termination of the optimization.

Table 5.1: DE settings

Mutation scheme	DE/rand/1/bin
Multiplication factor	0.6
Crossover probability	0.55
Population size	32
Max. number of generations	300

5.2.3 EOF analysis

The unknowns we need to find using DE are the SSPs for the different tracks. An SSP is, however, a continuous profile over depth, which implies that the number of unknowns is infinite. To limit the number of unknowns, we make use of EOFs, which are determined from measured SSPs. They constitute a set of orthogonal basis functions from which the measured SSPs can be reconstructed.

Each measured SSP (c_n) can be described by

$$c_n = \bar{c} + \sum_m p_{m,n} v_m \,, \tag{5.2}$$

where $\bar{c}$ is the mean SSP of the dataset, $p_{m,n}$ the m^{th} EOF coefficient of the n^{th} SSP and v_m the m^{th} EOF. The EOFs are the eigenvectors of the covariance matrix R, which is defined as

$$R = \frac{1}{N} \sum_{n=1}^{N} [c_n - \bar{c}][c_n - \bar{c}]^T \,, \tag{5.3}$$

where N is the total number of SSPs. Subsequently, the EOF coefficients p follow from

$$p_{m,n} = V^{-1}[c_n - \bar{c}] \,, \tag{5.4}$$

where V is the matrix containing the eigenvectors of the covariance matrix.

We can approximate an SSP using the G largest eigenvalues by

$$\bar{c_n} = \bar{c} + \sum_{m=1}^{G} p_{m,n} v_m \,. \tag{5.5}$$

In this way, SSPs can be constructed using a limited number of variables, instead of needing to define the sound speed at every point in depth. This simplifies the candidate solutions in DE to a vector with EOF coefficients, which length depends on the number of EOFs and the number of tracks.

5.3 Proof-of-concept

As a proof-of-concept, we start with the inversion of a set of synthetically generated SSPs from a simulated MBES survey. We consider a rectangular domain with a constant depth of 20 m including white noise with an amplitude of 2.2 cm (Figure 5.2a). The MBES survey is simulated by sailing three parallel tracks through the domain in north-south direction (dashed black lines). Along each track, a ping is emitted every 5 m and the swaths overlap for 70%. In order to calculate the travel times, a SSP is required. For this simulation, synthetic SSPs are generated using 3 EOFs, which are obtained after performing an EOF analysis on an existing dataset of 288 measured SSPs. The EOF coefficients are randomly generated within the range of the coefficients of the original SSPs. The resulting synthetic SSPs are shown in Figure 5.2b. The sound speed varies over depth between 1455 ms^{-1} and 1475 ms^{-1}. Subsequently, the travel time per beam for every ping is computed using a ray tracing algorithm. Since this survey consists of 3 tracks and 3 EOF coefficients per SSP are required, 9 unknowns need to be estimated per segment.

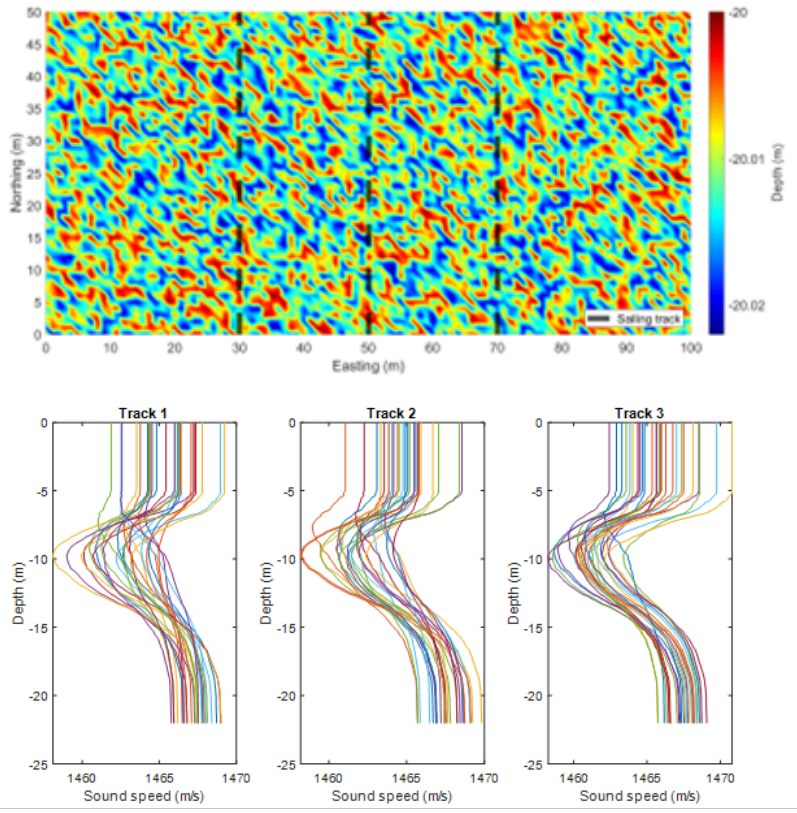

Figure 5.2: a) The domain with a depth of 20 m and the three sailed tracks (black dashed lines). b) The synthetic SSPs per track that are used to calculate the travel times for each ping.

Figure 5.3a shows the inverted SSPs (dashed lines) of the first ping of each track, estimated using the algorithm described in Section 5.2 together with the correct SSPs (solid lines). The maximum deviation is less than 1 ms^{-1}. There is also good agreement between the vertical structure of the estimated SSP and the correct SSP. To inspect the performance of the inversion, we can also check the estimated bathymetry (Figure 5.3b and c). The difference between the bathymetry estimated using the inverted SSPs and the correct bathymetry is in the order of millimetres. This is much smaller than the IHO standards for hydrographic surveys. For NL order A, which is the Dutch national

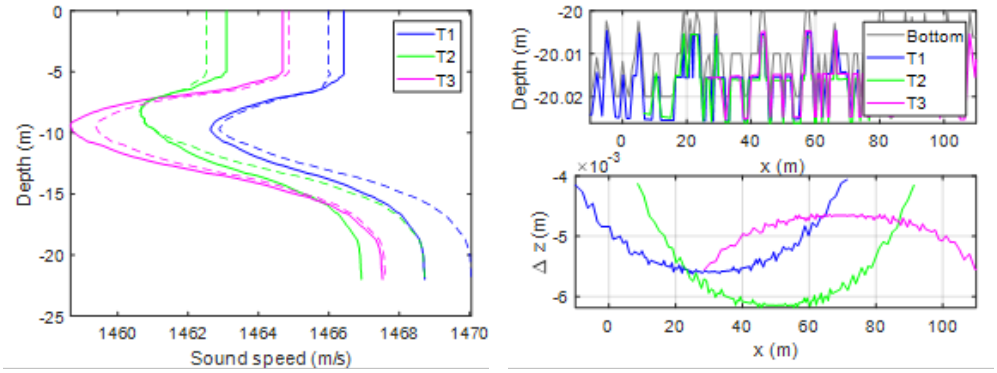

Figure 5.3: The results from the inversion for the first segment. a) The correct SSPs (solid lines) and the inverted SSPs (dashed lines) for the first ping of track 1 (blue), 2 (green), and 3 (magenta) (y = 0 and x = 30, 50 and 70 in Figure 5.2a). b) The estimated bathymetry for each track. The grey line represents the bottom. c) The difference between the bottom and estimated bathymetry per track. Note the convex-shaped deformations as a result of the small deviations in the estimated SSP.

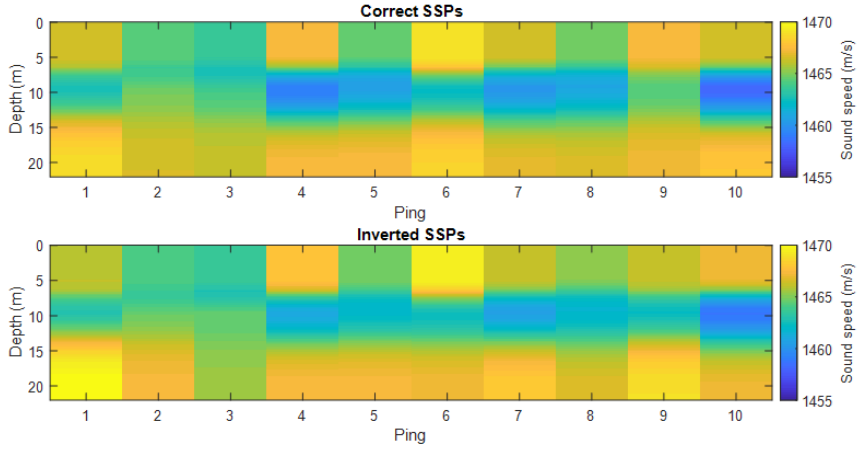

Figure 5.4: The correct SSPs (a) and the inverted SSPs (b) for all pings along track 1 (x = 30 in Figure 5.2a).

standard for hydrographic measurements, the maximum total vertical uncertainty is 0.18 m, assuming a depth of 20 m. Figure 5.4 shows the inverted SSPs for the first 10 pings along the first track. Again, we find a good agreement in the vertical structure of the SSPs and a maximum deviation of 1 ms^{-1}. Similar results are found for track 2 and 3 (not presented here).

So for this idealized case, the results indicate that the proposed method is able to successfully invert the SSPs from MBES measurements. A major simplification, however, is that these synthetic SSPs can be fully described using only three EOFs. In reality, more EOFs might be required to accurately describe the SSPs. The more EOFs are needed, the more unknowns need to be found, which will complicate the inversion. An important question is, therefore, whether an accurate estimate of measured SSPs can be obtained if only a limited number of EOFs is included.

5.4 Number of required EOFs

In this section, we assess the number of required EOFs to get an accurate estimate of the SSP in case actual measured SSPs are used. To this end, we use the same MBES survey as in the previous section. However, we replace the synthetic SSPs by a dataset consisting of 65 measured SSPs, which is collected in the North Sea along the Dutch coast. For each ping, we randomly select a SSP from the dataset and recalculate the travel time. First, we explore the variability in the measured SSPs that is described by each EOF. Subsequently, we run the inversion including a varying number of EOFs.

The dataset of 65 historically collected SSPs is shown in Figure 5.5a. First, we perform an EOF analysis on this dataset. Figure 5.5b indicates the cumulative sum of eigenvalues, indicating what percentage of variation in the SSPs is accounted for by taking into account an increasing number of EOFs. In contrast to the synthetic SSPs, the first 3 EOFs explain now 96.3% of the variability in the measured SSPs. However, the fact that most of the variability is already described by the first few EOFs suggests that including only a limited number of EOFs could result in an accurate estimate of the SSP. This would simplify the inversion.

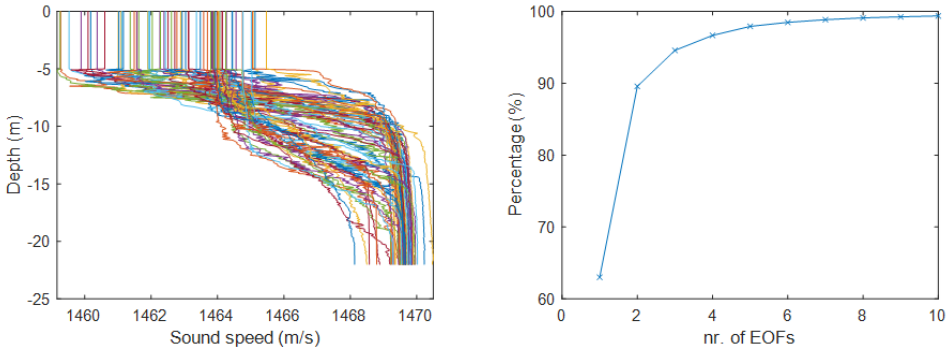

Figure 5.5: a) Dataset of historically collected SSPs along Dutch coast. b) Cumulative percentage of the variability in sound speed explained by the number of included EOFs for this dataset.

Next, we reconstruct the SSPs of the first ping of each track using an increasing number of EOFs. Subsequently, the bathymetry is determined and the energy function evaluated as a function of the number of EOFs (Figure 5.6a – blue line). As expected, the energy reduces if more EOFs are included. However, it is found that more than 50 EOFs are required to approach the global minimum, i.e. the value of the energy function obtained using the measured SSPs (Figure 5.6a – blue versus dashed black line). This is an unexpected result, however, as almost all of the variability was already described by the first 10 EOFs (Figure 5.5b). If we take a closer look at the higher order EOFs, for example v_{20} (Figure 5.6b), we find that these EOFs can be characterized as a noisy signal. These wiggles cannot be related to variations in temperature or salinity in the water column, while it can cause significant deformation of the estimated bathymetry. Therefore, we applied a 1-m moving average to remove the noise from the profiles. After computing the energy function again using the smoothed SSPs, it turns out that now only 12 EOFs are needed to approach the global minimum (Figure 5.6a – orange versus dashed black line). Moreover, including only 2 EOFs results in a close approximation of the optimum already. This suggests again that only a limited number of coefficients needs to be found to obtain an accurate estimate of the SSPs.

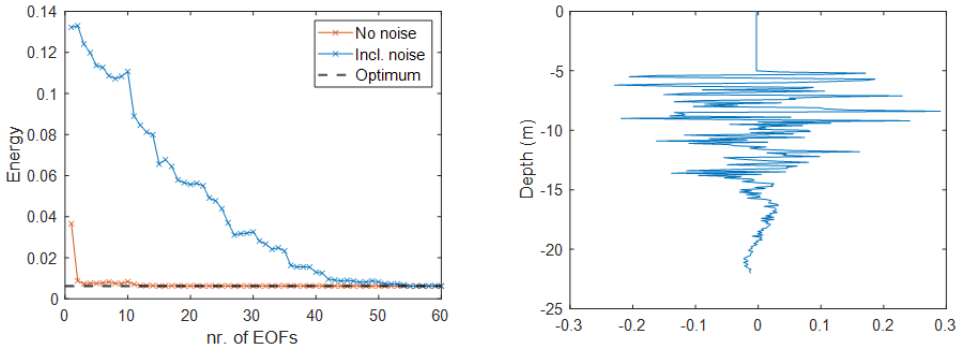

Figure 5.6: a) The energy as a function of the number of included EOFs for two different cases: the measured SSPs including noise (blue line) and the smoothed SSPs (orange line). The SSPs are constructed using the correct EOF coefficients. The dashed line depicts the optimum, computed using the correct SSP. b) Example of a higher order EOF dominated by a noisy signal: v_{20}.

To verify these findings, we carried out the actual inversion for the first segment several times, while including a varying number of EOFs. The same settings as in the previous simulation are used for DE (Table 5.1). The results are presented in Figure 5.7. Including more than 2 EOFs does not significantly improve the estimate of the SSP. The maximum deviation of 2 ms^{-1} is the same for 2, 3 and 4 EOFs and no significant improvement in the representation of the vertical structure is found. Also the value for the energy function does not decrease further. This shows that including only 2 EOFs in the inversion results in an accurate estimate of the SSP, confirming what was found in Figure 5.6a.

To check the performance in more detail, the inversion including 2 EOFs is carried out for all pings. In Figure 5.9, the results are shown for the first ping of all tracks.

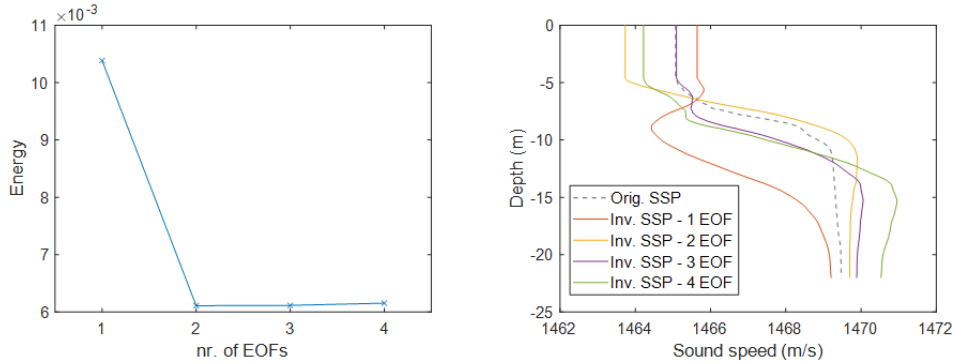

Figure 5.7: Results from the inversion while including a varying number of EOFs, showing a) the energy and b) the inverted SSP for the first ping of the first track. The dashed line in (b) shows the correct SSP.

5

As a reference, we also plotted the SSPs approximated using Equation 5.5 including 2 EOFs and the correct coefficients. The difference between these approximated profiles (solid lines) and the correct SSPs (grey dashed lines) is less than 0.4 ms^{-1}, confirming again that the profiles can be closely approximated by only 2 EOFs. Also the inverted SSPs (colored dashed lines) show strong agreement with the correct SSPs. Figure 5.9 shows the estimated SSPs for the first 10 pings along the first track. The deviation from the correct sound speed near the bed is less than 0.5 ms^{-1}, while the surface sound speed deviates up to 3 ms^{-1}. In practice, however, the sound speed near the transducer at the surface is measured constantly which could be used to correct the

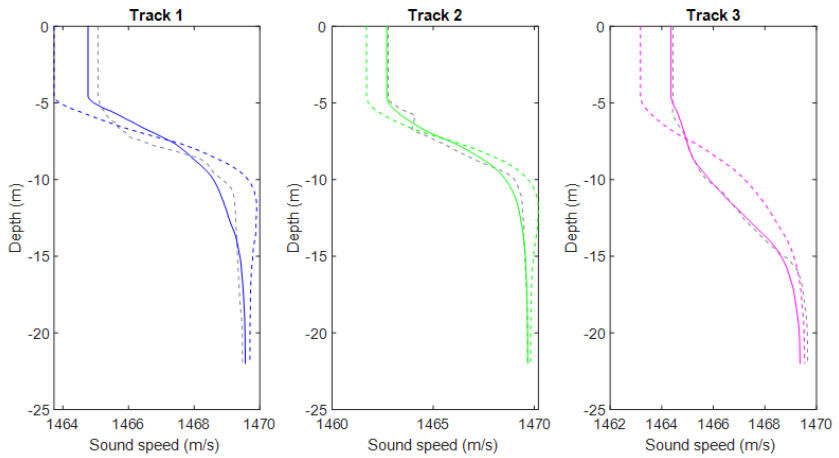

Figure 5.8: The inverted SSPs (dashed colored lines) for the first ping of track 1 (blue), 2 (green), and 3 (magenta) (y = 0 and x = 30, 50 and 70 in Figure 5.2a). The solid colored lines depict the approximated SSP by Equation 5.5 using 2 EOFs and the correct coefficients. The dashed grey lines are the correct SSPs.

inversion. In terms of ocean properties, this deviation of 3 ms^{-1} corresponds to a difference in salinity of about 2.5 PSU or in temperature of about 0.8 ° C, based on Medwin's empirical relation for the sound speed in water (Medwin, 1975). Looking at the vertical structure, all SSPs show a strong vertical gradient between 5 m and 12 m. Although this gradient is reproduced in all estimated profiles, the depth at which this gradient is found differs up to 5 m. What causes this deviation requires further investigation, particularly since this depth will likely coincide with the pycnocline, which is an important ocean property. The bathymetry estimated using the inverted SSPs differs less than 5 cm from the correct bathymetry (not shown here), which is again far below the IHO requirements for vertical depth uncertainty of 18 cm. This indicates that the energy function is correctly minimized.

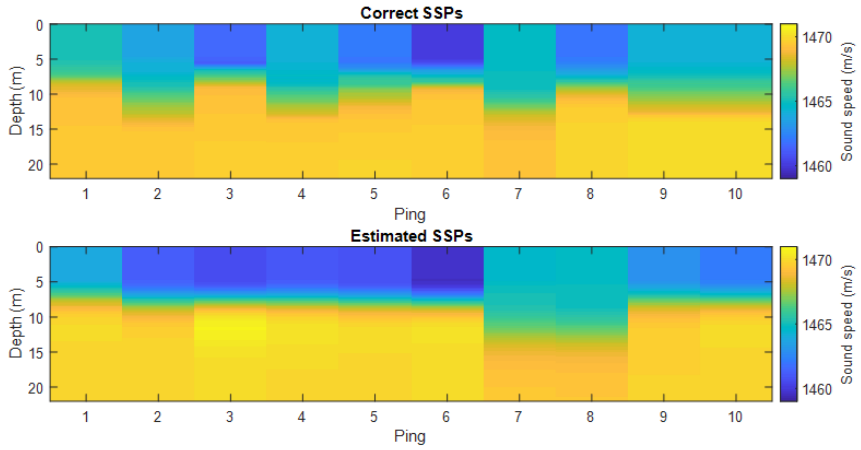

Figure 5.9: The correct SSPs (a) and the inverted SSPs (b) for all pings along the first track (x = 30 in Figure 5.2a).

5.5 Conclusions

Sound speed profiles provide valuable information on the vertical structure of the water column. Therefore, we propose a method to invert the sound speed profiles from MBES measurements. Using an energy function, we quantify the mismatch between overlapping swaths caused by the use of erroneous SSPs. The SSP is estimated by minimizing this energy function using Differential Evolution, a global optimization method. The use of empirical orthogonal functions allows us to describe the SSPs in an efficient way, as we can limit the number of unknowns that needs to be found during the inversion. This method provides a SSP for each ping of every track, resulting in datasets with high resolution in time and space.

In this study, we applied the inversion on two simulations of an MBES survey: one using synthetic SSPs that are fully described by 3 EOFs and one using historically collected SSPs near the Rhine-Meuse Delta. Both simulations showed promising results. The maximum deviation of the estimated SSPs was in the order of 1–3 ms^{-1}. In gen-

eral, also good agreement in vertical structure was found, although the depth of the pycnocline, which corresponds to a strong gradient in sound speed, was not always accurately reproduced for the second simulation. This requires further investigation. Furthermore, it was found that only 2 EOFs were required to get an accurate estimate of the SSP. The number of unknowns can thus be successful limited by parameterizing the SSP using EOFs.

Chapter 6

Discussion

In this chapter, a synoptic picture of the Rhine River plume is provided by integrating the insights of this thesis with previous studies. The aim is to understand the difference between a ROFI and river plume. Next, the contribution of the Rhine River plume to sea-level variability is highlighted and the implications for future studies are discussed. Furthermore, the opportunities regarding the inversion of sound speed profiles and possible next steps to fully exploit the potential of using multibeam echosounder measurements in oceanography are explored. This chapter, and thereby this thesis, ends with a future outlook including recommendations for further research and the concluding remarks.

6.1 Synthesis of the Rhine River plume

Many observational studies reported the effect of tides and winds on the stratification in the Rhine River plume (Simpson and Souza, 1995; Souza and Simpson, 1996; de Ruijter et al., 1997; Rijnsburger et al., 2018), providing insight in the dominant physical mechanisms that control the dispersion of freshwater. Using idealized modelling, de Boer et al. (2006) showed how the interaction between tides and stratification controls the structure of the far-field plume. Recently, Rijnsburger et al. (2021a) were the first to apply a realistic model to the near- to mid-field region of the Rhine River plume. They showed that a multiple front system is formed due to the trapping of tidal plume fronts by ambient tidal currents. Chapter 2 built upon their work by investigating the interaction between the plume, tides and winds and the connection between the different plume regions. Here, the various studies are reconciled, creating a synoptic picture of the Rhine River plume.

The simulations of a spring-neap cycle with idealized wind forcing show that the plume structure depends on the phasing of tides and winds. The tidally-pulsed river outflow results in the formation of tidal plume fronts, as described by Hessner et al. (2001). These fronts are initially arrested by the southward directed ebb currents. When these tidal currents turn, the fronts start propagating northwards. On spring tide, the fronts are strongly advected by tidal currents and propagate alongshore as separate pulses of freshwater, similar to the observations by de Ruijter et al. (1997). In contrast, a multiple front system is found on neap tide, which is similar to the findings of Rijnsburger et al. (2021a), with fronts recirculating in the mid-field plume for multiple tidal cycles.

This recirculation in the mid-field plume has recently been observed using HF radar measurements (Jakšić, 2021) and found in different model simulations (this thesis, but also by Jakšić (2021); Rijnsburger et al. (2021a)). It has strong similarities to a bulge circulation. However, the contrast between slack water after HW and LW (see Jakšić, 2021) shows that the recirculation is more complex than a classical bulge (as described by Nof and Pichevin, 2001) being suppressed by ambient currents (Fong and Geyer, 2002; Horner-Devine, 2009). The onset mechanism of the recirculation is unclear. Furthermore, it remains to be elucidated what the role of the tidal dynamics is, which modify the river outflow and are influenced by the interaction with bottom friction and the headland.

In the far-field plume, a fortnightly and semidiurnal cycle in stratification is found. Similar to the observations of Simpson and Souza (1995), the plume is stratified on neap tide and mainly well-mixed on spring tide (Figure 6.1a,c), except for the (remnants of the) tidal plume fronts. During strong winds, wind mixing dominates, breaking down the stratification (Souza and Simpson, 1996). The semidiurnal cycle in stratification is caused by cross-shore tidal straining (Simpson and Souza, 1995; de Boer et al., 2008). The resulting asymmetry in tidal mixing enhances the landward transport of freshwater, moving the plume onshore (Pietrzak et al., in prep.).

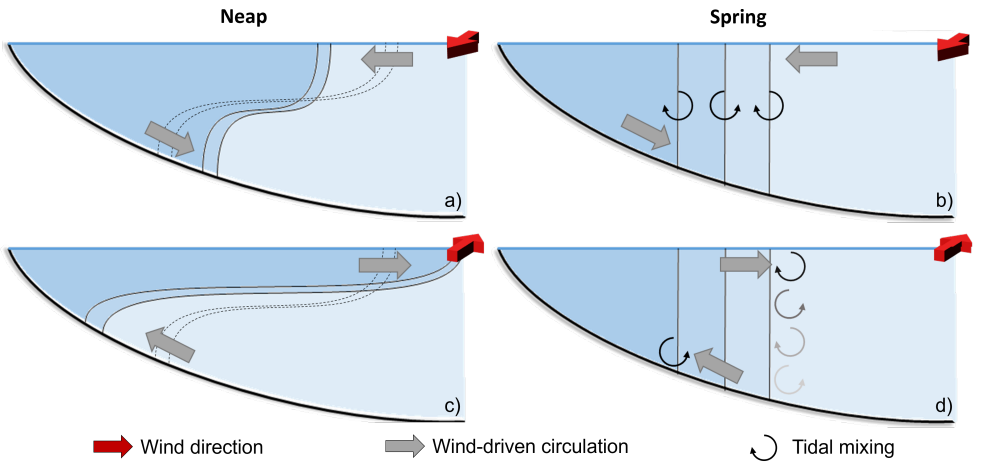

Figure 6.1: Schematic representation of the sping-neap variability in the plume's response to alongshore winds on neap (a,c) and spring tide (b,d): a) the plume is stratified and narrows under downwelling winds; b) the plume is well-mixed, downwelling winds induce more vertical mixing but cause little change in plume width; c) the plume is stratified and widens under upwelling winds; d) the plume is well-mixed, tidal mixing hinders the offshore displacement of the plume under the influence of upwelling winds.

Altogether, the structure of the far-field plume depends on the phasing of tides and winds (Pietrzak et al., in prep., Chapter 2). They showed that the timing of the winds relative to the phase of the tidal cycle is crucial to the plume's wind-driven response, as the plume is more susceptible to wind-driven displacement during the ebb phase of the tidal cycle. In addition, Chapter 2 showed that the response of

the far-field plume to relatively calm winds differs between spring and neap tide, as schematized in Figure 6.1. On neap tide, when the plume is generally stratified, the wind-driven response is in accordance with Ekman dynamics, as described by Fong and Geyer (2001); Whitney and Garvine (2005). On subtidal timescales, the plume moves offshore and thins under upwelling winds (Figure 6.1b), while it is confined against the coast and thickens under downwelling winds (Figure 6.1a). However, on spring tide, tidal mixing is enhanced and the far-field plume is well-mixed. As a consequence, a different wind-driven response of the plume is found. Under upwelling winds, limited offshore displacement is observed due to shorter mixing timescales (Figure 6.1d). Under downwelling winds, no change in plume width is found (Figure 6.1c). The isopycnals are already vertical; further tilting of the isopycnals would result in unstable stratification. The different wind-driven response between spring and neap tide highlights how the competition between straining and mixing determines the structure of the Rhine River plume.

6.2 ROFI OR RIVER PLUME? — That's the question

In literature, the Rhine River plume is often referred to as the Rhine ROFI (Region Of Freshwater Influence). However, when synthesizing the findings of this thesis, strong similarities with other river plumes are found, such as the Merrimack River and Columbia River plumes. This raises the question of what the differences are between a ROFI and a river plume. A general, consistent classification of river plumes enables comparing and contrasting different systems.

Simpson (1997) defined a ROFI as "the region between the shelf sea regime and the estuary where the local input of freshwater buoyancy from the coastal source is comparable with, or exceeds, the seasonal input of buoyancy as heat which occurs all over the shelf". The term ROFI is first found in the literature about the Rhine ROFI and Liverpool Bay around the early 1990's. Horner-Devine et al. (2015) defined a river plume as "a distinct region where water properties are significantly influenced by the riverine freshwater". The use of the term river plume goes back to the early 1960's in research related to the Columbia River plume. These definitions seem very similar. Here, the differences are pursued to be understood.

Horner-Devine et al. (2015) referred to ROFIs as "systems with multiple freshwater sources or shallow frictional shelves", being a subcategory of the prototypical river plume. According to this classification, ROFIs are characterized by the strong influence of bottom friction, being widespread in Europe. European systems such as Liverpool Bay and Rhine ROFI are the classical examples. However, the scaling of Flores et al. (2020, their Eq. 12 and Figure 13) shows that tidal straining could occur globally at higher latitudes (> 30 °), given that the depth is limited. Moreover, recent research, including this thesis, has shown that the Rhine River plume exhibits more of the characteristics of a prototypical plume than of the schematized ROFI (Figure 6.2). On top of that, a strong resemblance with plumes that are classified as prototypical is found, such as the Merrimack River and Columbia River plumes. Similar to these plumes, the outflow of the Rhine River is tidally pulsed. In the near-field region of the Rhine River plume, tidal plume fronts are formed. A recirculation that resembles a bulge is observed in the mid-field region. In the far-field plume, an alongshore current is

found, which is sensitive to Ekman dynamics.

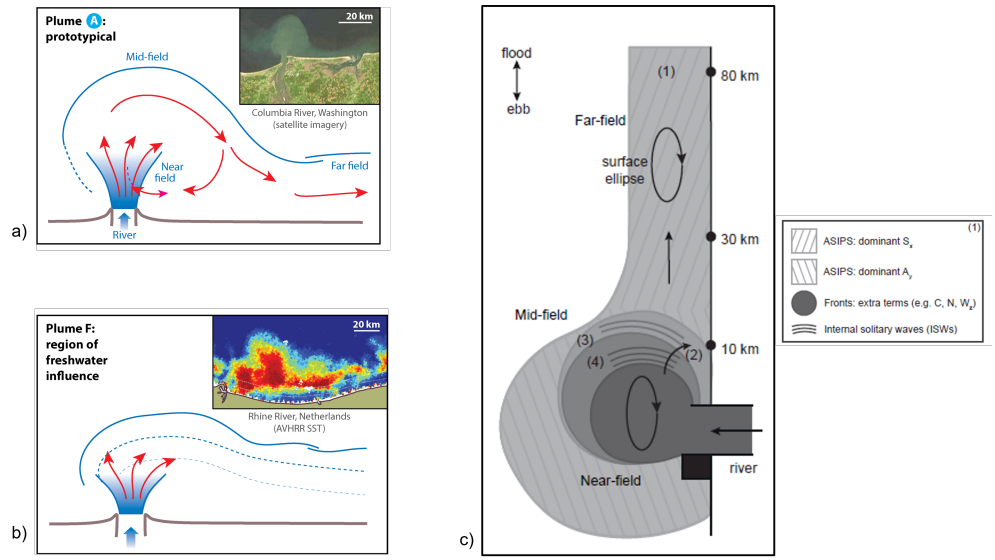

Figure 6.2: a) Morphology of a prototypical river plume, as defined by Horner-Devine et al. (2015), including an example of the Columbia River plume. b) Morphology of a ROFI, as defined by Horner-Devine et al. (2015), including an example of the Rhine ROFI. c) Synoptic picture of the Rhine River plume, as presented by Rijnsburger (2021), highlighting the role of ASIPS (1), onshore propagating tidal plume fronts (2), trapping of fronts in the recirculation (3) and internal waves accompanying the fronts (4).

Overall, more similarities than differences are found between the Rhine ROFI and other river plumes that are qualified as prototypical. Therefore, it is argued that the Rhine ROFI can definitely be seen as a worthy river plume. The terms river plume and ROFI seem to be very similar, having originated from different continents at different times. One could argue that the influence of bottom friction results in plumes with unique dynamics, which need a distinct classification. In this case, the use of frictional river plume is suggested. The term ROFI is suggested to be used in order to describe coastal systems influenced by multiple freshwater sources.

6.3 Baroclinic sea-level contribution

While river plumes are extensively studied (for example Horner-Devine et al., 2015, and references therein), their impact on sea level has received relatively little attention. Especially in shallow, shelf seas, such as the Southern North Sea, steric changes are often considered to be negligble. Chapter 3 shows that even the plume of a moderate river like the Rhine River plume can significantly affect sea-level variability.

The Rhine River plume induces a positive anomaly in steric height, elevating the annual mean sea level along the Dutch coast. Near the river mouth, the steric height

exhibits strong tidal variability driven by the tidally-pulsed outflow, while slower fluctuations correlate with variations in river discharge. These steric changes modulate the tidal signal, since they are coherent. Due to the phasing of the outflow, the steric height is maximum at LW, when the outflow is maximum. Consequently, the observed LW levels are higher than they would be for a barotropic tidal signal (Figure 6.3), resulting in a local decrease of the M2 amplitude. This leads to a decrease in tidal amplitude and a reduction of sea-level variance.

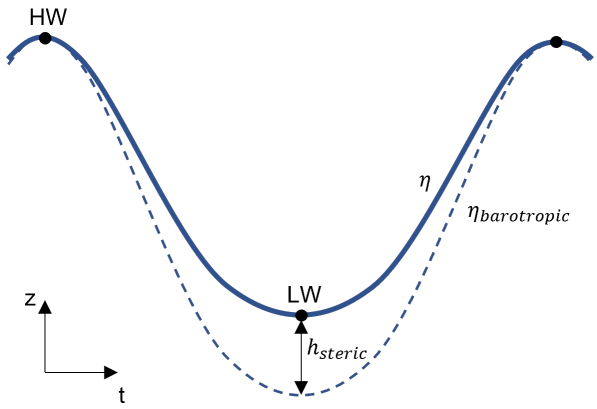

Figure 6.3: Schematic representation of the sea surface elevation η during a tidal cycle. $\eta_{\text{barotropic}}$ represents the tidal signal without accounting for density effects. The difference between the two signals is the steric height.

This raises the question how tide gauge data from stations near the river mouth should be interpreted. For example, when tide gauge data without steric correction is used to calibrate a barotropic tidal model, the tidal amplitude would be underestimated. Although the relative importance and the phasing of the steric changes depends on the system's characteristics, these implications likely hold for many tidally-pulsed river plumes and estuaries around the world (e.g., Columbia River (Horner-Devine et al., 2009; Spicer et al., 2021) and Merrimack River (Spicer et al., 2021)).

Farther downstream in the Rhine River plume, the steric variability diminishes due to mixing, and no significant effect on tidal sea-level variability is observed. Nevertheless, comparison with satellite altimetry reveals improved agreement when the river plume is included, indicating its influence on sea-level variability and highlighting the necessity to properly resolve river plumes in models. Furthermore, the impact of steric changes on the sea surface elevation can be relevant for those interested in using altimeter-derived coastal water levels to study a particular component of the water level (e.g., tides or surges). It is important to be aware that there is a runoff signal in the water levels that needs to be corrected for as well.

On seasonal timescales, steric changes depend on the wind-driven response of the river plume, rather than on variations in the river discharge. This corresponds with findings of the Amazon River plume (Giffard et al., 2019). When studying wind-driven sea-level variability or filtering out wind-driven effects, one should be aware that the wind-driven signal interacts non-linearly with the river plume (Chapter 2). Further-

more, although no significant changes in tidal propagation due to steric changes were found in this thesis, these changes in sea surface elevation could impact the tides (Haigh et al., 2020), especially in other systems where the steric contribution can be larger.

6.4 Inversion of MBES measurements

Multibeam echosounder (MBES) measurements are potentially a great source of information for oceanographic research, including the research of river plumes. Water column data can already provide 3D images of the water column, revealing its vertical structure and features such as internal waves (Colbo et al., 2014). The biggest limitation, however, is that only qualitative properties of the water column can be derived from the backscatter, rather than for example the exact water temperature or salinity. Consequently, the use of the information is limited. For example, validating and calibrating hydrodynamic models requires values for the temperature and salinity. Chapter 5 presented a proof-of-concept for the inversion of sound speed profiles from MBES measurements. This is a first step towards the inversion of temperature and salinity data. Here, the problems that need to be overcome and the next steps to be taken are discussed.

The energy function in the inversion algorithm could not always distinguish between correct and incorrect sound speed profiles. This could be caused by a so-called equivalent sound speed profile. Since an equivalent sound speed profile results in an accurate estimate of the bathymetry (Geng and Zielinski, 1999), the energy function gives a minimum value, resulting in an inaccurate estimate of the sound speed profile. In practice, the sound speed is continuously measured at reception. By restricting the estimated sound speed profile based on the measured surface sound speed, this problem could probably be avoided. Another, complementary way might be to further constrain the optimization based on the knowledge of the environment, to ensure that the resulting profiles are physically feasible (Gourret et al., 2024).

The first, next step in the development of the inversion method could be to assess the accuracy of the estimated sound speed profiles when measured data are used. Key questions that arise concern the required size of the dataset required to construct the EOFs and the obtained accuracy of the estimated sound speed profiles. The uncertainty in the estimated sound speed profile is an important indicator for the potential accuracy of the inversion of temperature and salinity profiles from MBES measurements, and thereby the feasibility of the method.

Hereafter, the same algorithm can be transformed to be used for the inversion of temperature and salinity data. The EOFs should describe temperature and salinity profiles. Combining the temperature and salinity profiles gives a sound speed profile, for which the energy function can be computed in exactly the same way as it is done in the current proof-of-concept. In this way, the algorithm would optimize for the EOF coefficients describing the temperature and salinity profiles, instead of the sound speed profile. The current proof-of-concept provides therefore a sound basis for the collection of temperature and salinity data using an MBES.

6.5 Future outlook & recommendations

In this fast changing world, realistic hydrodynamic models, including their ability to resolve river plumes, will become more and more important. Global climate change is affecting the Earth's oceans, and thereby the coastal systems and river plumes. Sea-level changes will affect tidal propagation (Haigh et al., 2020), which strongly interacts with river plumes (Spicer et al., 2021; Rijnsburger et al., 2021a; de Boer et al., 2008). River discharges are changing due to the intensification of the hydrological cycle (Rottler et al., 2020; Gloor et al., 2013), which is the source of buoyancy that forms the river plume. Changing near-surface winds, as reported by Deng et al. (2021), will not only affect the ocean circulation (Zhai et al., 2012) and air-sea interactions (Renault et al., 2017), but also the wind-driven response of river plumes in coastal seas. Hydrodynamic models improve the understanding of these systems, which is crucial for adaptation and management of the coastal zone.

Furthermore, the world digitizes rapidly and decision making becomes more and more data-driven. Real-time hydrodynamic simulations could support offshore operations and enhance safe shipping. A potential application is using the temperature and salinity model output to compute a 3D field of the sound speed, which can function as input for multibeam echosounders used during hydrographic surveys (Church, 2020). This requires high-resolution models (including uncertainty estimates) that are able to resolve river plumes.

The formation and propagation of the tidal plume fronts were the largest source of uncertainty in the modelling used in this thesis. From a numerical point of view, improving the ability of hydrostatic models to resolve tidal plume fronts will require improved parametrizations of non-hydrostatic processes, because of the non-hydrostatic nature of tidal plume fronts. Furthermore, increasing computational power will allow for finer grids, on which smaller-scale features such as tidal plume fronts can be better resolved.

From a physical point of view, improving the understanding of the interaction between the estuary and the river plume is crucial, as estuarine processes determine the properties of the outflow (Nash et al., 2009). Around the liftoff point, where the outflow separates from the bed and forms a buoyant layer, strong mixing is expected to occur (Cole et al., 2020). Furthermore, the tidally-pulsed outflow results in the formation of tidal plume fronts (Hessner et al., 2001; Rijnsburger et al., 2021a), which are critical for the downstream evolution of the plume (Chapter 2).

Another key aspect, on which this thesis already touched, will be improving the understanding of the recirculation in the mid-field plume, as it affects the (onshore) propagation of tidal plume fronts. First of all, the onset mechanism of the circulation is unclear. In the case of a classic bulge, anticyclonic vorticity must be generated to establish the recirculation (Nof and Pichevin, 2001). However, the source of the vorticity is unknown, although it is likely generated within the estuary or at the river mouth (Jakšić, 2021).

Furthermore, tides introduce variability in the Rhine River plume on timescales shorter than the timescales associated with the adjustment to steady forcing as used in many studies focusing on bulges (e.g. Nof and Pichevin, 2001; Fong and Geyer, 2001). The inflow Rossby number, which controls the bulge formation and alongshore freshwater transport (Fong and Geyer, 2002), varies strongly during a tidal cycle because of

the tidally-pulsed river outflow. The maximum Rossby number is found at High Water Slack (HWS - slack water after HW), coinciding with the moment the recirculation is observed (Jakšić, 2021). The question for future research is whether these assumptions are justified in the mid-field plume. In particular in tidally-pulsed river plumes such as the Rhine River plume, where the mid-field plume varies strongly during a tidal cycle, the formation timescale of the bulge is unclear.

Lastly, it is important to elucidate the role of friction in the formation of the recirculation. In general, bottom friction generally hinders the formation of a bulge circulation (Huq, 2009). However, in the Rhine River plume, tidal ellipses are formed due to bottom friction (Prandle, 1982), resulting in onshore-directed tidal currents at HWS, exactly when the recirculation is observed. While previous studies, which mainly focused on the far-field plume, assumed that this onshore transport is compensated vertically (Visser et al., 1994; de Boer et al., 2006), Jakšić (2021) found that (part of) the onshore transport is deflected back upstream into the recirculation. This is in line with Whitehead (1985), who showed that the majority of the freshwater will be deflected in the anticyclonic direction by the coastal wall in case of a baroclinic jet with a near-normal incident angle. Therefore, the onshore-directed tidal currents potentially enhance the recirculation around HWS, while the currents suppress the bulge during the remainder of the tidal cycle. Moreover, tidal currents are reduced north of the headland, potentially providing a sheltered region where the recirculation can develop.

6.6 Concluding remarks

The aim of this thesis was to advance the understanding of the Rhine River plume and its contribution to sea-level variability. The interaction between tides and winds, particularly the phasing of these processes, determines the structure and evolution of the Rhine River plume, from the near- to far-field plume. By expressing the potential energy anomaly in terms of salinity coordinates, it was shown how tidal plume fronts transfer freshwater from the near-field to the mid- and far-field plume under the influence of tides and winds. The wind-driven response of the Rhine River plume varies strongly between spring and neap tide. On neap tide, when the plume is stratified, the wind-driven response is in accordance with Ekman dynamics. On spring tide, however, the plume is mainly well-mixed due to increased tidal mixing, and the Ekman-driven response is limited. In turn, the spring-neap variability of the plume is modulated by these wind-driven changes.

Moreover, this study showed that the Rhine River plume contributes to sea-level variability through steric changes — a mechanism often overlooked in sea-level research. These steric changes are driven by the interaction of freshwater, winds and tides and vary on tidal and seasonal timescales.

Furthermore, a proof-of-concept for the inversion of sound speed profiles from multibeam echosounder measurements was provided, which is based on minimizing the mismatch between overlapping swaths caused by the use of erroneous sound speed profiles. It provides high-resolution sound speed data in time and space, which can can offer valuable insights into the vertical structure of the water column. This method has the potential to become a valuable tool for determining temperature and salinity

profiles using MBES data, which is routinely collected but not exploited.

Overall, innovative tools (inversion of sound speed profiles) and analysis techniques (combining the potential energy anomaly with salinity coordinates) are used that supported advancing the understanding of the Rhine River plume and its contribution to sea-level variability. The findings in this thesis are important for, amongst other, ecology and coastal protection.

APPENDIX A

Model validation

Here, we validate the adjusted Dutch Continental Shelf Model (DCSM) for water levels, salinity and velocity in the near-field region of the Rhine River plume. To validate the water levels, long-term water level records from the tidal stations at Hoek van Holland and Scheveningen are used. A good representation of the tide is of critical importance, since tides are known to influence the formation and evolution of the tidal plume fronts in the near-field region (Rijnsburger et al., 2021a) and the stratification in the mid- to far-field region of the ROFI (Simpson et al., 1993; de Boer et al., 2008). Field data collected during the STRAINS campaign in September 2014 (Pietrzak et al., 2018; Rijnsburger et al., 2018; Flores et al., 2018) are used to further validate the model for currents and salinity in the Rhine ROFI. The model reproduces the main features of the Rhine ROFI correctly. Therefore, we find the model useful to explore the plume's response to winds under different tidal conditions.

A.1 Sea surface elevation

In the southern North Sea, tides are characterized as progressive Kelvin waves that propagate in anti-clockwise direction. The main tidal constituents are M2 and S2, which induce a spring-neap cycle. Figure A.1 shows the observed water levels at Hoek van Holland for a complete spring-neap cycle in September 2014. Based on a period of 3 months (1 July 2014 – 1 October 2014), the RMSE is 9.2 cm at Hoek van Holland and 7.3 cm at Scheveningen. For Hoek van Holland, a harmonic analysis of the water level shows that the phase of the tide matches. Only small phase differences are found for M2 and S2. The model slightly underestimates the tidal range, since the model tends to overestimate the water level at LW. The tidal amplitude of M2 and S2 is slightly underpredicted, while the amplitude of the two most important overtides, M4 and MS4, is overpredicted. Overall, we find that the modelled and measured water levels are in good agreement.

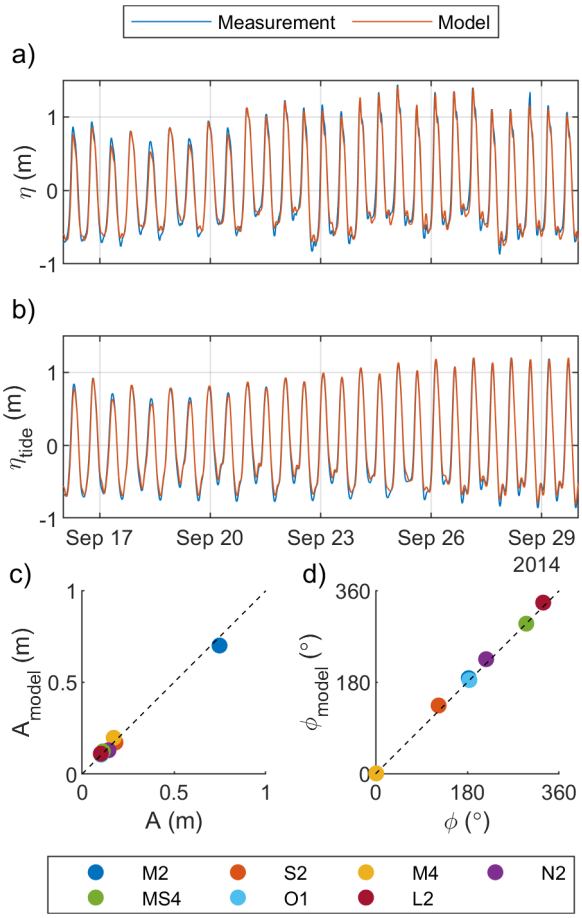

Figure A.1: Comparison between modelled and measured water level at Hoek van Holland. a) Sea surface height (m) and b) tidal elevation (m) for a spring-neap cycle in September 2014. c) Tidal amplitude (m) and d) phase (°) of the 7 largest tidal constituents, for which the amplitude is larger than 10 cm. The reconstructed tidal signal and the tidal constituents are obtained after harmonic analysis using UTide (Codiga, 2011), based on a 3 month period.

A.2 Comparison against field data

In September 2014, the STRAINS field campaign was conducted 10 km north of the river mouth (Pietrzak et al., 2018; Rijnsburger et al., 2018; Flores et al., 2018). We used their field data to validate the model results – in particular, flow velocities and salinity, and their variations over depth. A detailed description of the conditions during the measurement campaign is given by Rijnsburger et al. (2018). Here, we check if the characteristics of the Rhine ROFI are reproduced by the model, focusing on the differences between spring and neap tide.

Figure A.2 shows a comparison between model output and measurements of the cross-shore and alongshore velocities and the salinity during neap and spring tide. Overall, the temporal and vertical structure of the currents are captured well by the model. The magnitude and phase of the modelled alongshore velocity matches with the measurements. The alongshore velocity is in phase with the sea surface elevation, indicating the progressive Kelvin wave, and switches direction twice a day corresponding to the semidiurnal tide. Maximum flood currents (northward) are found around HW and maximum ebb currents (southward) around LW. On spring tide, the alongshore currents are about two times stronger than on neap tide at this location.

We find also good agreement between the modelled and measured cross-shore velocities. In the vertical structure of the cross-shore velocity, we can see the decoupling of the surface and bottom layer with opposite directed currents, as described by de Boer et al. (2006). During ebb (from LW to HW), the surface current is directed onshore, while the current is directed offshore near the bottom. During flood (from HW to LW), the opposite is found with offshore-directed surface currents and onshore-directed bottom currents directed currents are found.

The model is also able to reproduce the salinity reasonably well. A small bias of 0.4 PSU and a RMSE of 0.36 PSU is found in the bottom layer. Because of the configuration of the CTDs on the moorings, we cannot identify the pycnocline from the observed salinity. However, since it is known that this structure is a result of the interaction between tides and stratification (de Boer et al., 2006), the similar vertical structure of the cross-shore velocities indicates that the pycnocline depth is correctly reproduced by the model (Figure A.2e–h).

In Figure A.2j and l, we observe the stratification and the tidal plume fronts. On neap tide, the upper 5 m of the water column is significantly fresher than the deeper waters, indicating the strong stratification. We can also observe the tidal plume fronts passing around 2 hours after HW. On spring tide, they can already be observed within an hour after HW. Moreover, deeper water (between 5 and 10 m) is fresher due to increased tidal mixing, compared to neap tide.

In Figure A.3, the passing of the tidal plume fronts is more clearly visible in the measured data. We find a RMSE of 2.77 PSU here. During neap tide and calm conditions (around September 17–18), good agreement is found between model and measurements. On spring tide (around September 25) or storm conditions (September 20–21), there are some larger discrepancies, especially in the timing of the fronts. We believe this is caused by the combination of small errors, which add up during energetic conditions. First of all, we simulate tidal plume fronts, which are highly non-hydrostatic features, using a hydrostatic model with a relatively coarse grid (with respect to a single front). Although hydrostatic models can be used to get a general

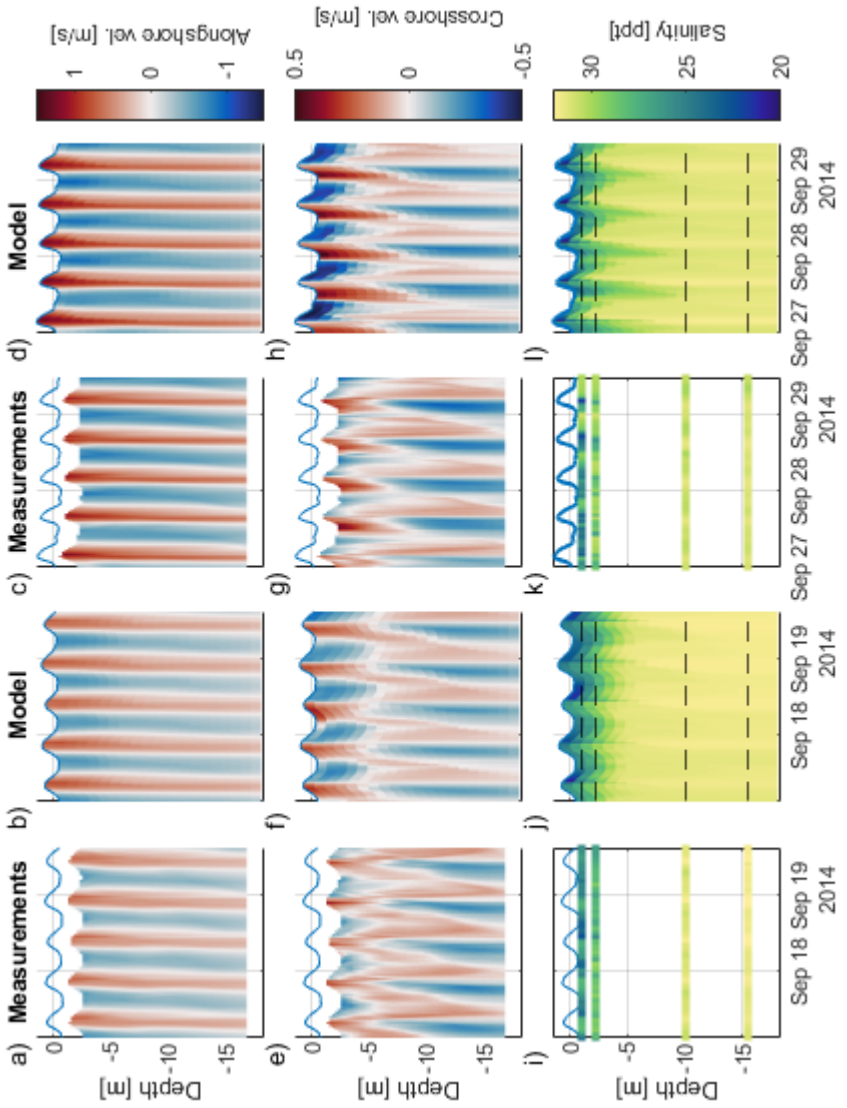

Figure A.2: Comparison between field data and model output on neap (17–19 September) (left two columns) and spring tide (27–29 September) (right two columns). a–d) Alongshore velocity (ms^{-1}). c–h) Cross-shore velocity (ms^{-1}). i–l) Salinity (PSU).

understanding of fronts (Cole et al., 2020), not all the physics are captured. To resolve the details of the fronts and their path more accurately, a non-hydrostatic model is required, which is left for future work. Moreover, the tidal plume front is formed and released at LW. However, at LW we also find the largest deviation in the tidal signal. A small error in this timing will influence the further evolution of the front. Furthermore, wave mixing, which is largest during storms, is not included.

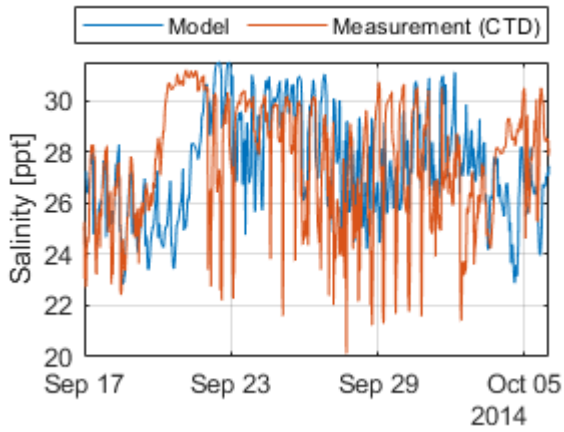

Figure A.3: Comparison between the modelled (blue) and measured (orange) salinity in the surface layer during the spring-neap cycle. The strong salinity jumps indicate the passing of the tidal plume fronts.

Bibliography

Berdeal, I. G., B. M. Hickey, and M. Kawase (2002), Influence of wind stress and ambient flow on a high discharge river plume, *Journal of Geophysical Research: Oceans*, *107*, doi:10.1029/2001JC000932.

Burchard, H., and R. Hofmeister (2008), A dynamic equation for the potential energy anomaly for analysing mixing and stratification in estuaries and coastal seas, *Estuarine, Coastal and Shelf Science*, *77*, 679–687, doi:10.1016/J.ECSS.2007.10.025.

Burchard, H., and H. Rennau (2008), Comparative quantification of physically and numerically induced mixing in ocean models, *Ocean Modelling*, *20*, 293–311, doi:10.1016/J.OCEMOD.2007.10.003.

Carstensen, J., J. H. Andersen, B. G. Gustafsson, and D. J. Conley (2014), Deoxygenation of the Baltic Sea during the last century, *Proceedings of the National Academy of Sciences*, *111*(15), 5628–5633, doi:10.1073/pnas.1323156111.

Chandanpurkar, H. A., T. Lee, X. Wang, H. Zhang, S. Fournier, I. Fenty, I. Fukumori, D. Menemenlis, C. G. Piecuch, J. T. Reager, O. Wang, and J. Worden (2022), Influence of nonseasonal river discharge on sea surface salinity and height, *Journal of Advances in Modeling Earth Systems*, *14*, e2021MS002,715, doi:10.1029/2021MS002715.

Chant, R. J., S. M. Glenn, E. Hunter, J. Kohut, R. F. Chen, R. W. Houghton, J. Bosch, and O. Schofield (2008), Bulge formation of a buoyant river outflow, *Journal of Geophysical Research: Oceans*, *113*, doi:10.1029/2007JC004100.

Choi, B. J., and J. L. Wilkin (2007), The effect of wind on the dispersal of the Hudson River plume, *Journal of Physical Oceanography*, *37*, 1878–1897, doi:10.1175/JPO3081.1.

Church, I. W. (2020), Multibeam sonar ray-tracing uncertainty evaluation from a hydrodynamic model in a highly stratified estuary, *Marine Geodesy*, *43*, 359–375, doi:10.1080/01490419.2020.1717695.

Codiga, D. (2011), Unified tidal analysis and prediction using the UTide Matlab functions, doi:10.13140/RG.2.1.3761.2008.

Colbo, K., T. Ross, C. Brown, and T. Weber (2014), A review of oceanographic applications of water column data from multibeam echosounders, *Estuarine, Coastal and Shelf Science*, *145*, 41–56, doi:10.1016/J.ECSS.2014.04.002.

Cole, K. L., D. G. Macdonald, G. Kakoulaki, and R. D. Hetland (2020), River plume source-front connectivity, *Ocean Modelling*, *150*, 101,571, doi:10.1016/j.ocemod.2020.101571.

Das, S., and P. N. Suganthan (2011), Differential evolution: A survey of the state-of-the-art, *IEEE Transactions on Evolutionary Computation*, *15*, 4–31, doi:10.1109/TEVC.2010.2059031.

de Boer, G. (2009), On the interaction between tides and stratification in the Rhine region of freshwater influence, Ph.D. thesis, Delft University of Technology.

de Boer, G. J., J. D. Pietrzak, and J. C. Winterwerp (2006), On the vertical structure of the Rhine region of freshwater influence, *Ocean Dynamics*, *56*, 198–216, doi:10.1007/s10236-005-0042-1.

de Boer, G. J., J. D. Pietrzak, and J. C. Winterwerp (2008), Using the potential energy anomaly equation to investigate tidal straining and advection of stratification in a region of freshwater influence, *Ocean Modelling*, *22*, 1–11, doi:10.1016/j.ocemod.2007.12.003.

de Boer, G. J., J. D. Pietrzak, and J. C. Winterwerp (2009), SST observations of upwelling induced by tidal straining in the Rhine ROFI, *Continental Shelf Research*, *29*, 263–277, doi:10.1016/j.csr.2007.06.011.

de Nijs, M. A. J., J. D. Pietrzak, and J. C. Winterwerp (2011), Advection of the salt wedge and evolution of the internal flow structure in the Rotterdam Waterway, *Journal of Physical Oceanography*, *41*, 3–27, doi:10.1175/2010JPO4228.1.

de Ruijter, W. P., A. W. Visser, and W. G. Bos (1997), The Rhine outflow: a prototypical pulsed discharge plume in a high energy shallow sea, *Journal of Marine Systems*, *12*, 263–276, doi:10.1016/s0924-7963(96)00102-9.

Deng, K., C. Azorin-Molina, L. Minola, G. Zhang, and D. Chen (2021), Global near-surface wind speed changes over the last decades revealed by reanalyses and cmip6 model simulations, *Journal of Climate*, *34*, 2219–2234, doi:10.1175/JCLI-D-20-0310.1.

Dinardo, S., L. Fenoglio-Marc, C. Buchhaupt, M. Becker, R. Scharroo, M. J. Fernandes, and J. Benveniste (2018), Coastal SAR and PLRM altimetry in German Bight and West Baltic Sea, *Advances in Space Research*, *62*, 1371–1404, doi:10.1016/J.ASR.2017.12.018.

Donlon, C., B. Berruti, A. Buongiorno, M. H. Ferreira, P. Féménias, J. Frerick, P. Goryl, U. Klein, H. Laur, C. Mavrocordatos, J. Nieke, H. Rebhan, B. Seitz, J. Stroede, and R. Sciarra (2012), The global monitoring for environment and security (GMES) Sentinel-3 mission, *Remote Sensing of Environment*, *120*, 37–57, doi:10.1016/J.RSE.2011.07.024.

Donnelly, C., J. C. Andersson, and B. Arheimer (2016), Using flow signatures and catchment similarities to evaluate the E-HYPE multi-basin model across Europe, *Hydrological Sciences Journal*, *61*, 255–273, doi:10.1080/02626667.2015.1027710.

Durand, F., C. G. Piecuch, M. Becker, F. Papa, S. V. Raju, J. U. Khan, and R. M. Ponte (2019), Impact of continental freshwater runoff on coastal sea level, *Surveys in Geophysics*, *40*, 1437–1466, doi:10.1007/S10712-019-09536-W.

Ehlers, F., F. Schlembach, M. Kleinherenbrink, and C. Slobbe (2023), Validity assessment of SAMOSA retracking for fully-focused SAR altimeter waveforms, *Advances in Space Research*, *71*, 1377–1396, doi:10.1016/J.ASR.2022.11.034.

EUMETSAT for Copernicus (2022), SRAL Level 1A Unpacked L0 Complex Echoes (version BC004) - Sentinel-3 - Reprocessed, doi:10.15770/EUM_SEC_CLM_0073.

Fisher, N. R., J. H. Simpson, and M. J. Howarth (2002), Turbulent dissipation in the Rhine ROFI forced by tidal flow and wind stress, *Journal of Sea Research*, *48*, 249–258, doi:10.1016/S1385-1101(02)00194-6.

Flores, R. P., S. Rijnsburger, A. R. Horner-Devine, A. J. Souza, and J. D. Pietrzak (2017), The impact of storms and stratification on sediment transport in the Rhine region of freshwater influence, *Journal of Geophysical Research: Oceans*, *122*, 4456–4477, doi:10.1002/2016JC012362.

Flores, R. P., S. Rijnsburger, S. Meirelles, A. R. Horner-Devine, A. J. Souza, J. D. Pietrzak, M. Henriquez, and A. Reniers (2018), Wave generation of gravity-driven sediment flows on a predominantly sandy seabed, *Geophysical Research Letters*, *45*, 7634–7645, doi:10.1029/2018GL077936.

Flores, R. P., S. Rijnsburger, A. R. Horner-Devine, N. Kumar, A. J. Souza, and J. D. Pietrzak (2020), The formation of turbidity maximum zones by minor axis tidal straining in regions of freshwater influence, *Journal of Physical Oceanography*, *50*, 1265–1287, doi:10.1175/JPO-D-18-0264.1.

Fong, D. A., and W. R. Geyer (2001), Response of a river plume during an upwelling favorable wind event, *Journal of Geophysical Research: Oceans*, *106*, 1067–1084, doi:10.1029/2000JC900134.

Fong, D. A., and W. R. Geyer (2002), The alongshore transport of freshwater in a surface-trapped river plume, *Journal of Physical Oceanography*, *32*, 957–972, doi:https://doi.org/10.1175/1520-0485(2002)032<0957:TATOFI>2.0.CO;2.

Frey, D., and A. Osadchiev (2021), Large river plumes detection by satellite altimetry: Case study of the Ob-Yenisei plume, *Remote Sensing*, *13*, 5014, doi:10.3390/RS13245014.

Fromant, G., N. L. Dantec, Y. Perrot, F. Floc'h, A. Lebourges-Dhaussy, and C. Delacourt (2021), Suspended sediment concentration field quantified from a calibrated multibeam echosounder, *Applied Acoustics*, *180*, 108,107, doi:10.1016/J.APACOUST.2021.108107.

Gaida, T. C., T. A. T. Ali, M. Snellen, A. Amiri-Simkooei, T. A. G. P. V. Dijk, and D. G. Simons (2018), A multispectral Bayesian classification method for increased acoustic discrimination of seabed sediments using multi-frequency multibeam backscatter data, *Geosciences*, *8*, 455, doi:10.3390/geosciences8120455.

Garvine, R. (2001), The impact of model configuration in studies of buoyant coastal discharge, *Journal of Marine Research*, *59*, 193–225.

Garvine, R. W. (1987), Estuary plumes and fronts in shelf waters: A layer model, *Journal of Physical Oceanography*, *17*, 1877–1896, doi:10.1175/1520-0485(1987)017<1877:EPAFIS>2.0.CO;2.

Geng, X., and A. Zielinski (1999), Precise multibeam acoustic bathymetry, *Marine Geodesy*, *22*, 157–167, doi:10.1080/014904199273434.

Giffard, P., W. Llovel, J. Jouanno, G. Morvan, and B. Decharme (2019), Contribution of the Amazon River discharge to regional sea level in the tropical Atlantic Ocean, *Water 2019, Vol. 11, Page 2348*, *11*, 2348, doi:10.3390/W11112348.

Gloor, M., R. J. Brienen, D. Galbraith, T. R. Feldpausch, J. Schöngart, J. L. Guyot, J. C. Espinoza, J. Lloyd, and O. L. Phillips (2013), Intensification of the Amazon hydrological cycle over the last two decades, *Geophysical Research Letters*, *40*, 1729–1733, doi:10.1002/GRL.50377.

Gourret, Y., T. Brander, and K. Hjelmervik (2024), Inverting the sound speed profile from multi-beam echo sounder data and historical measurements - a simulation study, in *Proceedings of the Institute of Acoustics*, Institute of Acoustics, doi:10.25144/22274.

Gregory, J. M., S. M. Griffies, C. W. Hughes, J. A. Lowe, J. A. Church, I. Fukimori, N. Gomez, R. E. Kopp, F. Landerer, G. L. Cozannet, R. M. Ponte, D. Stammer, M. E. Tamisiea, and R. S. van de Wal (2019), Concepts and terminology for sea level: Mean, variability and change, both local and global, *Surveys in Geophysics*, *40*, 1251–1289, doi:10.1007/S10712-019-09525-Z.

Gudmundsson, L., J. Boulange, H. X. Do, S. N. Gosling, M. G. Grillakis, A. G. Koutroulis, M. Leonard, J. Liu, H. M. Schmied, L. Papadimitriou, Y. Pokhrel, S. I. Seneviratne, Y. Satoh, W. Thiery, S. Westra, X. Zhang, and F. Zhao (2021), Globally observed trends in mean and extreme river flow attributed to climate change, *Science*, *371*, 1159–1162, doi:10.1126/science.aba3996.

Haigh, I. D., M. D. Pickering, J. A. Green, B. K. Arbic, A. Arns, S. Dangendorf, D. F. Hill, K. Horsburgh, T. Howard, D. Idier, D. A. Jay, L. Jänicke, S. B. Lee, M. Müller, M. Schindelegger, S. A. Talke, S. B. Wilmes, and P. L. Woodworth (2020), The tides they are a-changin': A comprehensive review of past and future nonastronomical changes in tides, their driving mechanisms, and future implications, *Reviews of Geophysics*, *58*, e2018RG000,636, doi:10.1029/2018RG000636.

Hermans, T. H., C. A. Katsman, C. M. Camargo, G. G. Garner, R. E. Kopp, and A. B. Slangen (2022), The effect of wind stress on seasonal sea-level change on the Northwestern European shelf, *Journal of Climate*, *35*, 1745–1759, doi:10.1175/JCLI-D-21-0636.1.

Hersbach, H., B. Bell, P. Berrisford, G. Biavati, A. Horányi, J. Muñoz Sabater, J. Nicolas, C. Peubey, R. Radu, I. Rozum, D. Schepers, A. Simmons, C. Soci, D. Dee, and J.-N. Thépaut (2018), ERA5 hourly data on single levels from 1979 to present, doi:10.24381/cds.adbb2d47.

Hessner, K., A. Rubino, P. Brandt, and W. Alpers (2001), The Rhine outflow plume studied by the analysis of synthetic aperture radar data and numerical simulations, *Journal of Physical Oceanography*, *31*, 3030–3044, doi:https://doi.org/10.1175/1520-0485(2001)031<3030:TROPSB>2.0.CO;2.

Hetland, R. D. (2005), Relating river plume structure to vertical mixing, *Journal of Physical Oceanography*, *35*, 1667–1688, doi:10.1175/JPO2774.1.

Hetland, R. D. (2010), The effects of mixing and spreading on density in near-field river plumes, *Dynamics of Atmospheres and Oceans*, *49*, 37–53, doi:10.1016/j.dynatmoce.2008.11.003.

Hetland, R. D., and S. F. DiMarco (2008), How does the character of oxygen demand control the structure of hypoxia on the Texas-Louisiana continental shelf?, *Journal of Marine Systems*, *70*, 49–62, doi:10.1016/J.JMARSYS.2007.03.002.

Hickey, B. M., L. J. Pietrafesa, D. A. Jay, and W. C. Boicourt (1998), The Columbia River plume study: Subtidal variability in the velocity and salinity fields, *Journal of Geophysical Research: Oceans*, *103*, 10,339–10,368, doi:10.1029/97JC03290.

Horner-Devine, A. R. (2009), The bulge circulation in the Columbia River plume, *Continental Shelf Research*, *29*, 234–251, doi:10.1016/J.CSR.2007.12.012.

Horner-Devine, A. R., D. A. Jay, P. M. Orton, and E. Y. Spahn (2009), A conceptual model of the strongly tidal Columbia River plume, *Journal of Marine Systems*, *78*, 460–475, doi:10.1016/J.JMARSYS.2008.11.025.

Horner-Devine, A. R., R. D. Hetland, and D. G. Macdonald (2015), Mixing and transport in coastal river plumes, *Annu. Rev. Fluid Mech*, *47*, 569–594, doi:10.1146/annurev-fluid-010313-141408.

Huq, P. (2009), The role of kelvin number on bulge formation from estuarine buoyant outflows, *Estuaries and Coasts*, *32*, 709–719, doi:10.1007/S12237-009-9162-Z.

Huthnance, J. M. (1991), Physical oceanography of the north sea, *Ocean and Shoreline Management*, *16*, 199–231, doi:10.1016/0951-8312(91)90005-M.

Intergovernmental Panel on Climate Change (2023a), *Climate Change 2021 - The Physical Science Basis*, Cambridge University Press, doi:10.1017/9781009157896.

Intergovernmental Panel on Climate Change (2023b), Technical summary, in *Climate Change 2021 - The Physical Science Basis*, pp. 35–144, Cambridge University Press, doi:10.1017/9781009157896.002.

Isobe, A. (2005), Ballooning of river-plume bulge and its stabilization by tidal currents, *Journal of Physical Oceanography*, *35*, 2337–2351, doi:10.1175/JPO2837.1.

Jakšić, L. (2021), The recirculation near Maasvlakte 2 in the Rhine ROFI: Assessing the influence of a manmade headland and baroclinic processes, Master's thesis, Delft University of Technology.

Jordà, G., and D. Gomis (2013), On the interpretation of the steric and mass components of sea level variability: The case of the Mediterranean basin, *Journal of Geophysical Research: Oceans*, *118*, 953–963, doi:10.1002/JGRC.20060.

Jurisa, J. T., and R. J. Chant (2013), Impact of offshore winds on a buoyant river plume system, *Journal of Physical Oceanography*, *43*, 2571–2587, doi:10.1175/JPO-D-12-0118.1.

Kakoulaki, G., D. Macdonald, and A. R. Horner-Devine (2014), The role of wind in the near field and midfield of a river plume, *Geophysical Research Letters*, *41*, 5132–5138, doi:10.1002/2014GL060606.

Kastner, S. E., A. R. Horner-Devine, and J. Thomson (2018), The influence of wind and waves on spreading and mixing in the fraser river plume, *Journal of Geophysical Research: Oceans*, *123*, 6818–6840, doi:10.1029/2018JC013765.

Kernkamp, H. W., A. van Dam, G. S. Stelling, and E. D. de Goede (2011), Efficient scheme for the shallow water equations on unstructured grids with application to the continental shelf, *Ocean Dynamics*, *61*, 1175–1188, doi:10.1007/S10236-011-0423-6.

Kilcher, L. F., and J. D. Nash (2010), Structure and dynamics of the columbia river tidal plume front, *Journal of Geophysical Research: Oceans*, *115*, doi:10.1029/2009JC006066.

Kourafalou, V. H., and Y. S. Androulidakis (2013), Influence of Mississippi River induced circulation on the Deepwater Horizon oil spill transport, *Journal of Geophysical Research: Oceans*, *118*, 3823–3842, doi:10.1002/JGRC.20272.

Kourafalou, V. H., L. Y. Oey, J. D. Wang, and T. N. Lee (1996), The fate of river discharge on the continental shelf: 1. modeling the river plume and the inner shelf coastal current, *Journal of Geophysical Research: Oceans*, *101*, 3415–3434, doi:10.1029/95JC03024.

Kummu, M., H. D. Moel, G. Salvucci, D. Viviroli, P. J. Ward, and O. Varis (2016), Over the hills and further away from coast: global geospatial patterns of human and environment over the 20th–21st centuries, *Environmental Research Letters*, *11*, 034,010, doi:10.1088/1748-9326/11/3/034010.

Lentz, S. (2004), The response of buoyant coastal plumes to upwelling-favorable winds, *Journal of Physical Oceanography*, *34*, 2458–2469, doi:10.1175/JPO2647.1.

Lentz, S. J., and J. Largier (2006), The influence of wind forcing on the chesapeake bay buoyant coastal current, *Journal of Physical Oceanography*, *36*, 1305–1316, doi:10.1175/JPO2909.1.

Levitus, S., T. P. Boyer, H. E. García, R. A. Locarnini, M. M. Zweng, A. V. Mishonov, J. R. Reagan, J. I. Antonov, O. K. Baranova, M. Biddle, M. Hamilton, D. R. Johnson, C. R. Paver, and D. Seidov (2014), World ocean atlas 2013, doi:10.7289/v5f769gt.

Li, J., Q. Gu, Y. Chen, G. Sun, and H. Huang (2018a), A combined ray tracing method for improving the precision of the USBL positioning system in smart ocean, *Sensors*, *18*, 3586, doi:10.3390/s18103586.

Li, X., W. R. Geyer, J. Zhu, and H. Wu (2018b), The transformation of salinity variance: A new approach to quantifying the influence of straining and mixing on estuarine stratification, *Journal of Physical Oceanography*, *48*, 607–623, doi:10.1175/JPO-D-17-0189.1.

Li, X., M. Lorenz, K. Klingbeil, E. Chrysagi, U. GrÃƒÂ¤we, J. Wu, and H. Burchard (2022), Salinity mixing and diahaline exchange flow in a large multi-outlet estuary with islands, *Journal of Physical Oceanography*, *52*, 2111–2127, doi:10.1175/JPO-D-21-0292.1.

Lurton, X. (2002), *An Introduction to Underwater Acoustics*, Springer-Verlag.

Maas, L. R. M., and J. J. M. van Haren (1987), Observations on the vertical structure of tidal and inertial currents in the central North Sea, *Journal of Marine Research*, *45*.

McGranahan, G., D. Balk, and B. Anderson (2007), The rising tide: assessing the risks of climate change and human settlements in low elevation coastal zones, *Environment and Urbanization*, *19*, 17–37, doi:10.1177/0956247807076960.

Meade, R. H., and K. O. Emery (1971), Sea level as affected by river runoff, eastern united states, *Science*, *173*, 425–428, doi:10.1126/SCIENCE.173.3995.425.

Medwin, H. (1975), Speed of sound in water: A simple equation for realistic parameters, *The Journal of the Acoustical Society of America*, *58*, 1318–1319, doi:10.1121/1.380790.

Moffat, C., and S. Lentz (2012), On the response of a buoyant plume to downwelling-favorable wind stress, *Journal of Physical Oceanography*, *42*, 1083–1098, doi:10.1175/JPO-D-11-015.1.

Mohammadloo, T. H. (2020), Optimizing hydrographic operations for bathymetric measurements using multibeam echosounders, Ph.D. thesis, Delft University of Technology, doi:https://doi.org/10.4233/uuid:a1bb9cd0-6eef-4665-a910-969d55667f35.

Mohammadloo, T. H., M. Snellen, W. Renoud, J. Beaudoin, and D. G. Simons (2019), Correcting multibeam echosounder bathymetric measurements for errors induced by inaccurate water column sound speeds, *IEEE Access*, *7*, 122,052–122,068, doi:10.1109/ACCESS.2019.2936170.

Muis, S., M. Verlaan, H. C. Winsemius, J. C. Aerts, and P. J. Ward (2016), A global reanalysis of storm surges and extreme sea levels, *Nature Communications 2016 7:1*, *7*, 1–12, doi:10.1038/ncomms11969.

Munchow, A., and R. W. Garvine (1993), Buoyancy and wind forcing of a coastal current, *Journal of Marine Research*, *51*, 293–322, doi:10.1357/0022240933223747.

Nash, J. D., L. F. Kilcher, and J. N. Moum (2009), Structure and composition of a strongly stratified, tidally pulsed river plume, *Journal of Geophysical Research: Oceans*, *114*, 0–12, doi:10.1029/2008JC005036.

Nau, A. W., B. Scoulding, R. J. Kloser, Y. Ladroit, and V. Lucieer (2022), Extended detection of shallow water gas seeps from multibeam echosounder water column data, *Frontiers in Remote Sensing*, *3*, doi:10.3389/frsen.2022.839417.

Nicholls, R. J., and A. Cazenave (2010), Sea-level rise and its impact on coastal zones, *Science*, *328*, 1517–1520, doi:10.1126/SCIENCE.1185782.

Nof, D., and T. Pichevin (2001), The ballooning of outflows, *Journal of Physical Oceanography*, *31*, 3045–3058, doi:10.1175/1520-0485(2001)031.

O'Donnell, J., G. O. Marmorino, and C. L. Trump (1998), Convergence and downwelling at a river plume front, *Journal of Physical Ocenography*, *28*, 1481–1495, doi:https://doi.org/10.1175/1520-0485(1998)028<1481:CADAAR>2.0.CO;2.

Oey, L.-Y., and G. L. Mellor (1993), Subtidal variability of estuarine outflow, plume, and coastal current: A model study, *Journal of Physical Oceanography*, *23*, 164–171, doi:10.1175/1520-0485(1993)023<0164:SVOEOP>2.0.CO;2.

Orton, P. M., and D. A. Jay (2005), Observations at the tidal plume front of a high-volume river outflow, *Geophysical Research Letters*, *32*, 1–4, doi:10.1029/2005GL022372.

Osadchiev, A., R. Sedakov, and A. Barymova (2021), Response of a small river plume on wind forcing, *Frontiers in Marine Science*, *8*, doi:10.3389/FMARS.2021.809566.

Oviatt, C. A., K. Huizenga, C. S. Rogers, and W. J. Miller (2019), What nutrient sources support anomalous growth and the recent sargassum mass stranding on Caribbean beaches? a review, *Marine Pollution Bulletin*, *145*, 517–525, doi:10.1016/J.MARPOLBUL.2019.06.049.

Pein, J., A. Valle-Levinson, and E. V. Stanev (2018), Secondary circulation asymmetry in a meandering, partially stratified estuary, *Journal of Geophysical Research: Oceans*, *123*, 1670–1683, doi:10.1002/2016JC012623.

Pfister, L., J. Kwadijk, A. Musy, A. Bronstert, and L. Hoffmann (2004), Climate change, land use change and runoff prediction in the Rhine-Meuse basins, *River Research and Applications*, *20*, 229–241, doi:10.1002/RRA.775.

Pichevin, T., and D. Nof (1997), The momentum imbalance paradox, *Tellus A*, *49*, 298–319, doi:10.1034/J.1600-0870.1997.T01-1-00009.X.

Piecuch, C. G., and R. Wadehra (2020), Dynamic sea level variability due to seasonal river discharge: A preliminary global ocean model study, *Geophysical Research Letters*, *47*, doi:10.1029/2020GL086984.

Piecuch, C. G., K. Bittermann, A. C. Kemp, R. M. Ponte, C. M. Little, S. E. Engelhart, and S. J. Lentz (2018), River-discharge effects on United States Atlantic and Gulf coast sea-level changes, *Proceedings of the National Academy of Sciences*, *115*, 7729–7734, doi:10.1073/PNAS.1805428115.

Pietrzak, J. D., G. J. de Boer, and M. A. Eleveld (2011), Mechanisms controlling the intra-annual mesoscale variability of SST and SPM in the southern North Sea, *Continental Shelf Research*, *31*, 594–610, doi:10.1016/j.csr.2010.12.014.

Pietrzak, J. D., A. J. Souza, and A. R. Horner-Devine (2018), Strains data, doi:10.4121/collection:strains.

Pietrzak, J. D., G. J. de Boer, A. Horner-Devine, A. Souza, S. E. Allen, and L. M. Keyzer (in prep.), Asymmetric mixing due to tidal straining influences wind driven ekman dynamics in a shallow river plume, manuscript in preparation.

Prandle, D. (1982), The vertical structure of tidal currents and other oscillatory flows, *Continental Shelf Research*, *1*, 191–207, doi:10.1016/0278-4343(82)90004-8.

Pritchard, M., and D. A. Huntley (2006), A simplified energy and mixing budget for a small river plume discharge, *Journal of Geophysical Research: Oceans*, *111*, doi:10.1029/2005JC002984.

Proudman, J., and A. T. Doodson (1924), The principal constituent of the tides of the North Sea, *Philosophical Transactions of the Royal Society of London. Series A, Containing Papers of a Mathematical or Physical Character*, *224*, 185–219, doi:10.1098/RSTA.1924.0005.

Renault, L., J. C. McWilliams, and S. Masson (2017), Satellite observations of imprint of oceanic current on wind stress by air-sea coupling, *Scientific Reports*, *7*, 1–7, doi:10.1038/s41598-017-17939-1.

Ricker, M., and E. V. Stanev (2020), Circulation of the European northwest shelf: a Lagrangian perspective, *Ocean Science*, *16*, 637–655, doi:10.5194/os-16-637-2020.

Rijkswaterstaat (2019), Verhaal van de Rijn-Maasmonding, *Tech. rep.*, Rijkswaterstaat, https://iplo.nl/thema/water/waterveiligheid/platform-rivierkennis/verhalenreeks-verhaal-rivier/verhaal-rijn-maasmonding/.

Rijnsburger, S. (2021), On the dynamics of tidal plume fronts in the Rhine region of freshwater influence, Ph.D. thesis, Delft University of Technology, doi:10.4233/uuid:279260a6-b79e-4334-9040-e130e54b9360.

Rijnsburger, S., C. M. van der Hout, O. van Tongeren, G. J. de Boer, B. C. van Prooijen, W. G. Borst, and J. D. Pietrzak (2016), Simultaneous measurements of tidal straining and advection at two parallel transects far downstream in the Rhine ROFI, *Ocean Dynamics*, *66*, 719–736, doi:10.1007/S10236-016-0947-X.

Rijnsburger, S., R. P. Flores, J. D. Pietrzak, A. R. Horner-Devine, and A. J. Souza (2018), The influence of tide and wind on the propagation of fronts in a shallow river plume, *Journal of Geophysical Research: Oceans*, *123*, 5426–5442, doi:10.1029/2017JC013422.

Rijnsburger, S., R. P. Flores, J. D. Pietrzak, A. R. Horner-Devine, A. J. Souza, and F. Zijl (2021a), The evolution of plume fronts in the Rhine region of freshwater influence, *Journal of Geophysical Research: Oceans*, *126*, 1–28, doi:10.1029/2019JC015927.

Rijnsburger, S., R. P. Flores, J. D. Pietrzak, K. G. Lamb, N. L. Jones, A. R. Horner-Devine, and A. J. Souza (2021b), Observations of multiple internal wave packets in a tidal river plume, *Journal of Geophysical Research: Oceans*, *126*, e2020JC016,575, doi:10.1029/2020JC016575.

Rippeth, T. P., N. R. Fisher, and J. H. Simpson (2001), The cycle of turbulent dissipation in the presence of tidal straining, *Journal of Physical Oceanography*, *31*, 2458–2471, doi:10.1175/1520-0485(2001)031<2458:TCOTDI>2.0.CO;2.

Rottler, E., T. Francke, G. BÃ¼rger, and A. Bronstert (2020), Long-term changes in central European river discharge for 1869-2016: Impact of changing snow covers, reservoir constructions and an intensified hydrological cycle, *Hydrology and Earth System Sciences*, *24*, 1721–1740, doi:10.5194/HESS-24-1721-2020.

Schlembach, F., F. Ehlers, M. Kleinherenbrink, M. Passaro, D. Dettmering, F. Seitz, and C. Slobbe (2023), Benefits of fully focused SAR altimetry to coastal wave height estimates: A case study in the North Sea, *Remote Sensing of Environment*, *289*, 113,517, doi:10.1016/J.RSE.2023.113517.

Simons, D. G., and M. Snellen (2009), A bayesian approach to seafloor classification using multi-beam echo-sounder backscatter data, *Applied Acoustics*, *70*, 1258–1268, doi:10.1016/j.apacoust.2008.07.013.

Simpson, J. H. (1981), The shelf-sea fronts: implications of their existence and behaviour, *Philosophical Transactions of the Royal Society of London. Series A, Mathematical and Physical Sciences*, *302*, 531–546, doi:10.1098/RSTA.1981.0181.

Simpson, J. H. (1997), Physical processes in the ROFI regime, *Journal of Marine Systems*, *12*, 3–15, doi:10.1016/s0924-7963(96)00085-1.

Simpson, J. H., and D. Bowers (1981), Models of stratification and frontal movement in shelf seas, *Deep Sea Research Part A, Oceanographic Research Papers*, *28*, 727–738, doi:10.1016/0198-0149(81)90132-1.

Simpson, J. H., and J. R. Hunter (1974), Fronts in the irish sea, *Nature*, *250*, 404–406, doi:10.1038/250404a0.

Simpson, J. H., and A. J. Souza (1995), Semidiurnal switching of stratification in the region of freshwater influence of the Rhine, *Journal of Geophysical Research: Oceans*, *100*, 7037–7044, doi:10.1029/95jc00067.

Simpson, J. H., J. Brown, J. Matthews, and G. Allen (1990), Tidal straining, density currents, and stirring in the control of estuarine stratification, *Estuaries*, *13*, 125–132, doi:10.2307/1351581.

Simpson, J. H., W. G. Bos, F. Schirmer, A. J. Souza, T. P. Rippeth, S. E. Jones, and D. Hydes (1993), Periodic stratification in the Rhine ROFI in the North Sea, *Oceanologica Acta*, *16*, 23–32.

Simpson, J. H., E. Williams, L. H. Brasseur, and J. M. Brubaker (2005), The impact of tidal straining on the cycle of turbulence in a partially stratified estuary, *Continental Shelf Research*, *25*, 51–64, doi:10.1016/J.CSR.2004.08.003.

Snellen, M., and D. G. Simons (2008), An assessment of the performance of global optimization methods for geo-acoustic inversion, *Journal of Computational Acoustics*, *16*, 199–223, doi:10.1142/S0218396X08003579.

Souza, A. J., and I. D. James (1996), A two-dimensional (x-z) model of tidal straining in the Rhine ROFI, *Continental Shelf Research*, *16*, 949–966, doi:10.1016/0278-4343(95)00033-X.

Souza, A. J., and J. H. Simpson (1996), The modification of tidal ellipses by stratification in the Rhine ROFI, *Continental Shelf Research*, *16*, 997–1007, doi:10.1016/0278-4343(95)00042-9.

Spicer, P., K. L. Cole, K. Huguenard, D. G. MacDonald, and M. M. Whitney (2021), The effect of bottom-generated tidal mixing on tidally pulsed river plumes, *Journal of Physical Oceanography*, *51*, 2223–2241, doi:10.1175/JPO-D-20-0228.1.

Spicer, P., K. Huguenard, K. L. Cole, D. G. MacDonald, and M. M. Whitney (2022), Evolving interior mixing regimes in a tidal river plume, *Geophysical Research Letters*, *49*, e2022GL099,633, doi:10.1029/2022GL099633.

Storn, R., and K. Price (1997), Differential evolution – a simple and efficient heuristic for global optimization over continuous spaces, *Journal of Global Optimization*, *11*, 341–359, doi:10.1023/A:1008202821328.

Straneo, F., and C. Cenedese (2015), The dynamics of Greenland's glacial fjords and their role in climate, *Annual Review of Marine Science*, *7*, 89–112, doi:10.1146/ANNUREV-MARINE-010213-135133.

Tebaldi, C., R. Ranasinghe, M. Vousdoukas, D. J. Rasmussen, B. Vega-Westhoff, E. Kirezci, R. E. Kopp, R. Sriver, and L. Mentaschi (2021), Extreme sea levels at different global warming levels, *Nature Climate Change*, *11*, 746–751, doi:10.1038/s41558-021-01127-1.

Thomson, J., A. R. Horner-Devine, S. Zippel, C. Rusch, W. Geyer, J. Thomson, A. R. Horner-Devine, S. Zippel, and C. Rusch (2014), Wave breaking turbulence at the offshore front of the Columbia River plume, *Geophysical Research Letters*, *41*, 8987–8993, doi:10.1002/2014GL062274.

Trenberth, K. E., L. Smith, T. Qian, A. Dai, and J. Fasullo (2007), Estimates of the global water budget and its annual cycle using observational and model data, *Journal of Hydrometeorology*, *8*, 758–769, doi:10.1175/JHM600.1.

van Aken, H. M. (1986), The onset of seasonal stratification in shelf seas due to differential advection in the presence of a salinity gradient, *Continental Shelf Research*, *5*, 475–485, doi:10.1016/0278-4343(86)90071-3.

van der Giessen, A., W. P. D. Ruijter, and J. C. Borst (1990), Three-dimensional current structure in the dutch coastal zone, *Neth J Sea Res*, *25*, 45–55, doi:10.1016/0077-7579(90)90007-4.

Verspecht, F., J. H. Simpson, and T. P. Rippeth (2010), Semi-diurnal tidal ellipse variability in a region of freshwater influence, *Geophysical Research Letters*, *37*, doi:10.1029/2010GL044470.

Vignudelli, S., F. Birol, J. Benveniste, L. L. Fu, N. Picot, M. Raynal, and H. Roinard (2019), Satellite altimetry measurements of sea level in the coastal zone, *Surveys in Geophysics*, *40*, 1319–1349, doi:10.1007/S10712-019-09569-1.

Vinogradov, S. V., and R. M. Ponte (2011), Low-frequency variability in coastal sea level from tide gauges and altimetry, *Journal of Geophysical Research: Oceans*, *116*, doi:10.1029/2011JC007034.

Visser, A. W., A. J. Souza, K. Hessner, J. H. Simpson, and A. W. Visser (1994), The effect of stratification on tidal current profiles in a region of freshwater influence, *Oceanologica Acta*, *17*, 369–381.

Volkov, D. L., W. E. Johns, and T. V. Belonenko (2016), Dynamic response of the Black Sea elevation to intraseasonal fluctuations of the mediterranean sea level, *Geophysical Research Letters*, *43*, 283–290, doi:10.1002/2015GL066876.

Vousdoukas, M. I., L. Mentaschi, E. Voukouvalas, M. Verlaan, S. Jevrejeva, L. P. Jackson, and L. Feyen (2018), Global probabilistic projections of extreme sea levels show intensification of coastal flood hazard, *Nature Communications*, *9*, 1–12, doi:10.1038/s41467-018-04692-w.

Whitehead, J. A. (1985), The deflection of a baroclinic jet by a wall in a rotating fluid, *Journal of Fluid Mechanics*, *157*, 79–93, doi:10.1017/S0022112085002312.

Whitney, M. M., and R. W. Garvine (2005), Wind influence on a coastal buoyant outflow, *Journal of Geophysical Research: Oceans*, *110*, 1–15, doi:10.1029/2003JC002261.

Wiles, P. J., L. A. van Duren, C. HÃƒÂ¤se, J. Larsen, and J. H. Simpson (2006), Stratification and mixing in the Limfjorden in relation to mussel culture, *Journal of Marine Systems*, *60*, 129–143, doi:10.1016/J.JMARSYS.2005.09.009.

Wiseman, W. J., N. N. Rabalais, R. E. Turner, S. P. Dinnel, and A. Macnaughton (1997), Seasonal and interannual variability within the Louisiana coastal current: Stratification and hypoxia, *Journal of Marine Systems*, *12*, 237–248, doi:10.1016/S0924-7963(96)00100-5.

Woodworth, P. L., M. MenÃƒÂ©ndez, and W. R. Gehrels (2011), Evidence for century-timescale acceleration in mean sea levels and for recent changes in extreme sea levels, *Surveys in Geophysics*, *32*, 603–618, doi:10.1007/S10712-011-9112-8/FIGURES/5.

Woodworth, P. L., A. Melet, M. Marcos, R. D. Ray, G. Wöppelmann, Y. N. Sasaki, M. Cirano, A. Hibbert, J. M. Huthnance, S. Monserrat, and M. A. Merrifield (2019), Forcing factors affecting sea level changes at the coast, *Surveys in Geophysics*, *40*, 1351–1397, doi:10.1007/S10712-019-09531-1.

Yankovsky, A. E., and D. C. Chapman (1997), A simple theory for the fate of buoyant coastal discharges, *Journal of Physical Oceanography*, *27*, 1386–1401, doi:10.1175/1520-0485(1997)027<1386:ASTFTF>2.0.CO;2.

Zhai, X., H. L. Johnson, D. P. Marshall, and C. Wunsch (2012), On the wind power input to the ocean general circulation, *Journal of Physical Oceanography*, *42*, 1357–1365, doi:10.1175/JPO-D-12-09.1.

Zhang, J., L. Cheng, Y. Wang, and C. Jiang (2023), The impact of tidal straining and advection on the stratification in a partially mixed estuary, *Water 2023*, *15*, 339, doi:10.3390/W15020339.

Zijl, F., J. Veenstra, and J. Groenenboom (2018), The 3D Dutch Continental Shelf Model - Flexible Mesh (3D DCSM-FM): Setup and validation, *Tech. rep.*, Deltares, https://publications.deltares.nl/1220339_000_0042.pdf.

About the author

I was born on 15 November 1993 in Woerden. From 2006 to 2012, I attended Veenlanden College in Mijdrecht for my secondary education. In 2012, I began my studies at Delft University of Technology. After completing a BSc in Civil Engineering in 2015, I continued with an MSc in Hydraulic Engineering. I specialized in Environmental Fluid Mechanics — a field that focuses on the physical processes of flows, waves, and sediment transport, and their integration with numerical modelling and engineering. In 2018, I graduated with my MSc thesis titled ”Predicting the Impact of Sea-Level Rise in Baie Orientale and Baie de L'Embouchure, Saint Martin”. That same year, I began a PhD within the ”Versatile Hydrodynamics” project, deepening my expertise in coastal oceanography and hydrodynamic modelling. In 2022, I started working at the Port of Rotterdam Authority as an advisor, applying the scientific insights gained during my academic career to practical challenges.

List of publications

Journal articles

Keyzer, L.M., Ehlers, F., Pietrzak, J.D., Katsman, C.A., Snellen, M., Verlaan, M., Zijl, F., Afrasteh, Y., Guarneri, H., Klees, R., Slobbe, D.C. (in prep.), The impact of a river plume on sea-level variability in a shallow shelf sea. [*Chapter 3*]

Pietrzak, J.D., de Boer, G.J., **Keyzer, L.M.**, Horner-Devine, A.R., Souza, A.J., Allen, S.E. (in prep.), Asymmetric mixing due to tidal straining influences wind driven Ekman dynamics in a shallow river plume.

Keyzer, L.M., Pietrzak, J.D., Katsman, C.A., Snellen, M., Verlaan, M., Zijl, F., Afrasteh, Y., Guarneri, H., Klees, R., Slobbe, D.C. (in prep.) Spring-neap variability in the wind-driven response of the Rhine River plume. [*Chapter 2*]

Keyzer, L. M., Herman, P. M., Smits, B. P., Pietrzak, J. D., James, R. K., Candy, A. S., Riva, R.E.M., Bouma, T.J., van der Boog, C.G., Katsman, C.A., Slobbe, D.C., Zijlema, M., van Westen, R.M., Dijkstra, H. A. (2020), The potential of coastal ecosystems to mitigate the impact of sea-level rise in shallow tropical bays, *Estuarine, Coastal and Shelf Science*, 246, 107050. https://doi.org/10.1016/j.ecss.2020.107050

Conference proceedings

Keyzer, L.M., Mohammadloo, T.H., Snellen, M., Pietrzak, J.D., Katsman, C.A., Afrasteh, Y., Guarneri, H., Verlaan, M., Klees, R., Slobbe, D.C., (2021). Inversion of sound speed profiles from MBES measurements using Differential Evolution. In *Proceedings of Meetings on Acoustics UACE* (Vol. 44, No. 1, p. 070035). Acoustical Society of America. https://doi.org/10.1121/2.0001508

Conference presentations

Keyzer, L.M., Pietrzak, J.D., Katsman, C.A., Snellen, M., Verlaan, M., Zijl, F., Afrasteh, Y., Guarneri, H., Klees, R., Slobbe, D.C., The impact of river plumes on the sea-level variability [oral presentation], EGU General Assembly 2023, Vienna, Austria, 23—28 Apr 2023, EGU23-11395, https://doi.org/10.5194/egusphere-egu23-11395.

Keyzer, L.M., Pietrzak, J.D., Katsman, C.A., Snellen, M., Verlaan, M., Zijl, F., Afrasteh, Y., Guarneri, H., Klees, R., Slobbe, D.C., Variations in the wind-driven response of the Rhine ROFI during a spring-neap cycle [oral presentation], EGU General Assembly 2022, Vienna, Austria, 23–-27 May 2022, EGU22-5768, https://doi.org/10.5194/egusphere-egu22-5768.

Keyzer, L.M., Pietrzak, J.D., Katsman, C.A., Snellen, M., Verlaan, M., Zijl, F., Afrasteh, Y., Guarneri, H., Klees, R., Slobbe, D.C., Spring-neap variability in the wind-driven response of the Rhine ROFI [online presentation], Ocean Sciences Meeting 2022, Online, 24 February – 4 March 2022.

Keyzer, L.M., Mohammadloo, T.H., Snellen, M., Pietrzak, J.D., Katsman, C.A., Afrasteh, Y., Guarneri, H., Verlaan, M., Klees, R., Slobbe, D.C., Inverting sound speed profiles from MBES measurements using Differential Evolution [online presentation], 6th Underwater Acoustics Conference and Exhibition, Online, 20—25 June 2021

Keyzer, L.M., Rijnsburger, S., Zijl, F., Verlaan, M., Snellen, M.., Slobbe, D.C., Flores, R.P., Souza, A.J., Horner-Devina, A.R., Pietrzak, J.D., The influence of wind on the evolution of freshwater fronts in the Rhine ROFI [online presentation], EGU General Assembly 2020, Online, 4—8 May 2020, EGU2020-14614, https://doi.org/10.5194/egusphere-egu2020-14614.

Keyzer, L.M., Rijnsburger, S., Zijl, F., Verlaan, M., Snellen, M.., Slobbe, D.C., Flores, R.P., Souza, A.J., Horner-Devina, A.R., Pietrzak, J.D., Dynamics in the near-field region of the Rhine ROFI: a multiple front system [oral presentation], Ocean Sciences Meeting 2020, San Diego, United States of America, 16—21 February 2020

Keyzer, L.M., Pietrzak, J.D., Herman, P.M.J., Smits, B.P., James, R.K., Candy, A.S., Riva, R.E.M., Predicting the impact of sea-level rise in Baie Orientale and Baie de L'Embouchure , Saint Martin [oral presentation], NCK days 2019, Enkhuizen, The Netherlands, 21–22 March 2019